Metamaterials, Surface Waves, and Their Applications

Author: Wenchen Chen

Boston College

The Graduate School of Arts and Sciences

Department of Physics

Metamaterials, Surface Waves, and Their Applications

a dissertation

by

Wen-Chen Chen

submitted in partial fulfillment of the requirements

for the degree of

Doctor of Philosophy

May and 2014

Abstract

Metamaterials, Surface Waves, and Their Applications

Author: Wen-Chen Chen

Adviser: Willie J. Padilla, Professor of Physics

The field of metamaterials (MMs) has garnered a great deal of attention ever since the experimental demonstration of negative refractive indexes. Such an exotic response stemmed from the engineering capability of MMs, as they can obtain almost any optical responses at any given frequency by carefully structuring the geometries. There are countless examples where MMs have posed promising results in tailoring free space radiation. However, their usage beyond this common platform is far less explored. For examples, surface electromagnetic waves, which offer great potentials for future device applications, could be an intriguing place for the further development of metamateirals.

In this dissertation, we study various MM configurations where the interplay between surface waves and metamaterials has a significant impact on the device performance. Firstly, Chapter 1 introduces some fundamental concepts of metamaterials and surface electromagnetic waves, and outline the fabrication, experiments, and characterization details. In Chapter 2, we investigate whether the effective optical parameters of MMs have the exact physical meaning as those of natural substances. Two types of MM resonators are studied, and we found the thickness of the host matrix plays a crucial role in such a homogenization process. Next, we present a

computational and experimental study of MMs in conjunction with a novel gigahertz/terahertz transmission line, in Chapter 3. By optimizing the coupling between the MMs and the signal, information can be encoded. Chapter 4 presents a study of designing an extremely subwavelength magnetic MM. By maximizing the effective inductance and capacitance of the structure, the final geometry obtains a strong magnetic resonance with the size of merely $\lambda_0/2000$, where λ_0 is the resonant wavelength. A novel time-domain spectroscopic method is also proposed to determine the frequency-dependent permeability of the samples. In Chapter 5, we characterize two hidden channels of MM perfect absorbers : scattering and generation of surface electromagnetic waves. In particular, we unveil lossy surface waves are generated during the process resulting in an enhancement of angular absorbance. The study provides a new insight to the working principle of MMAs. In Chapter 6, we investigate complementary MM structures that exhibit strong extraordinary optical transmission with higher transmission efficiency. We discover the origin of the fundamental mode is irrelevant to the Bloch modes. Lastly, we summarize all achievements and give an outlook in Chapter 7.

Contents

Acknowledgements

Foremost, I would like to express my deepest appreciation to my advisor Professor Willie J. Padilla for his guidance, for his support, for his patience, and for his thoughtfulness through my entire Ph. D. career. In addition to immense knowledge to which he has passed on me, more importantly he helped me develop a judgemental mind when doing research. All of these value lessons make me more appreciate and enjoy beauty of science.

I also would like to thank the rest of my thesis committees: Professor Krzysztof Kempa and Professor Michael J. Naughton for their value feedbacks to the work. Special thanks to Professor Krzystof Kempa for the theoretical assistance on several collaborated projects, from which I learned the field of plasmonics from a different viewpoint.

My sincere thanks also goes to my colleagues, Dr. David Shrekenhammer, Dr. Xianliang Liu, Christopher Bingham, Dr. Kebin Fan, Dr. Weitao Dai, Dr. Salvatore Sato, Dr. Nathan Landy, Claire Watts, Xinyu Liu, Xuyan Wu, and other members in Padilla's Lab. Thanks them for bearing my temper and cheering me up when I was under pressure. I am sure our friendship will last forever, and I am going to miss our time at Boston College.

In addition, it is fortunate and grateful that I had so many opportunities to work with talents around the world and learn from the greatest. Thanks to Professor David R. Smith, Professor Tahsin Akalin, Professor Yaroslav Urzhumov, Dr. Pramod K. Singh, and Jack J. Mock for sharing their time and expertise with me.

Last but not the least, I would like to thank all of my family, especially for my lovely wife, Hsin-I Lu. Pursuing a Ph.D. outside of our home country was never being easy, and we are lucky that we both went through and accomplished the task with many great memories. Graduation is just a beginning of our new adventure, and we will always stay strong no matter how many challenges are in the front. Cheers.

List of Tables

List of Figures

Chapter 1

Introduction

Surface electromagnetic waves (SEWs) are a special class of electromagnetic waves, where the energy is confined and travels in the metal/dielectric interface without radiation[1, 2]. They are commonly known as surface plasmon polaritons (SPPs) occurring at the plasma frequency of metals, ω_p. SPPs have many distinct advantages, i.e. guiding and confining electromagnetic energy beyond the diffraction limit, and are ideal for device applications. However, the benefits always come with a tradeoff as the energy dissipates strongly inside the metal preventing the wave from propagating for a long distance. In search of viable solutions, metamateirals (MMs) could be an ideal alternative as their optical properties can be engineered in a control manner. For examples, MMs obtain negative permeability in the optical regime to perform so-called hyper/super-lensing[3, 4, 5], and access the full optical parameter space to achieve more exotic responses, like cloaking[6, 7] or transformation optics[8, 9]. While MMs continue to show promising results in tailoring freespace light, their uses on either waveguides or surface electromagnetic waves, on the other hand, are far less explored. Moreover, surface waves could play a crucial role on affecting MM's responses even when designing free-space components. In nature, generating SPPs are

restricted since the host media need to satisfy some particular conditions - materials in the interface need to have opposite signs of permittivity and sufficiently high loss. These restrictions forbid the occurrence of SPPs at low frequencies - below than the plasma frequency of metals or semiconductors. As a result, their contribution outside of the optical regime is typically ignored. The conventional SPP treatments to the low frequency, however, might not be suitable for the artificial materials. This is because most of MMs are resonant and their effective optical constants could vary from a positive to a negative value by the operation frequency. A cause to the surrounding optical environment satisfying the SPP requirements could happen, even at a 'low' frequency. Thus, one shall not overlook the impact of surface waves especially on metamateiral systems.

In this dissertation, we provide several examples where the interplay between surface waves and metamaterials could significantly affect the overall spectral responses. Furthermore, we utilize metamaterial resonators to effective control surface electromagnetic waves.

1.1 Metamaterials

Metamaterials are periodic structured patterns and composed of conductive metals and a dielectric substrate. All dimensions of a unit cell are smaller than the operation wavelength of λ_0 ($\sim \lambda_0/10$), so they can be operated in the quasi-static limit[10, 11]. In this fashion, incoming radiation cannot distinguish each individual component and thus 'see' an effective response from these composites. Figure 1.1 illustrates incoming electric field interacts with a one-dimensional metamaterial array. As can be seen, the local E field distribution over a single cell (a) varies slowly so the excitation can

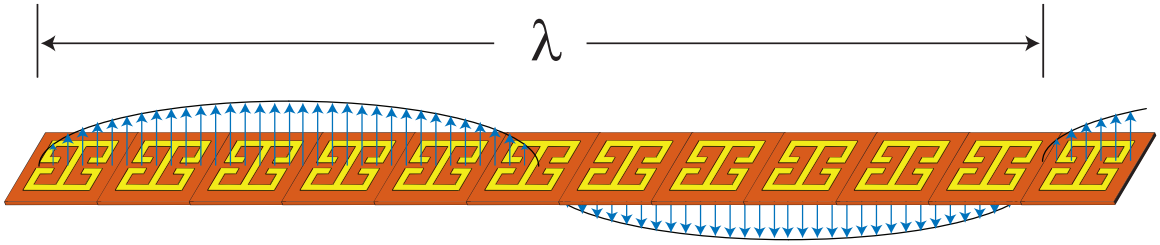

Figure 1.1: A chain of metamaterial array work in the long wavelength limit l ≫ a, light is not sensitive to the microscopic detail, but to the overall response. MMs can thus be treated as a homogenous medium.

be approximated as an uniform field. Based on the effective medium approach, the total scattering properties can then be described by the macroscopic qualities, such as electrical permittivity (ϵ) and magnetic permeability, both of which are governed by constitutive relations of Maxwell's equations - see Equation 1.1.

$$\begin{aligned} \tilde{D} &= \epsilon \tilde{E} \\ \tilde{H} &= \tfrac{1}{\mu} \tilde{B} \end{aligned} \tag{1.1}$$

where $\tilde{D}$ and $\tilde{E}$ are the electric displacement and electric field, $\tilde{H}$ and $\tilde{B}$ are the auxiliary magnetic and magnetic field, respectively.

Another salient feature of MMs is their properties are mainly controlled by their geometry but less by the intrinsic properties of the materials. As Maxwell's equations are scale invariance, the geometric effect at one frequency can be reproduced to the other by simply scaling their dimensions accordingly. There are a large variety of geometric resonators for various strategic advantages. Take Ω-shape resonators[12] as an example, a coupling between $\tilde{E}$ and $\tilde{H}$ field can be initiated due to lack of four-fold symmetry in the structure[13]. In this dissertation, we employ mainly the

structures whose bianisotropic effect, at least to the first order, is small. Two fundamental building blocks, magnetic and electric split-ring metamaterial resonators, will be introduced since they are more relevant with the rest of the topics.

1.1.1 Magnetic metamaterials

Diamagnetic responses of naturally occurring materials are almost negligible at high frequencies due to their inherently small magnetic dipole moments[10, 14]. To create strong diamagnetism John Pendry proposed using an array of artificial materials, known as split ring resonators (SRRs), and theoretically modeled their responses based on an effective medium approach[10]. The frequency-dependent permeability of SRRs can be expressed in a form of Lorentzian resonators.

$$\tilde{\mu}_r(\omega) = 1 + \frac{F\omega^2}{\omega_0^2 - \omega^2 - i\gamma\omega} \tag{1.2}$$

where F is the filling fraction, ω_0 is the resonance frequency, γ is the loss in the resonating SRR.

Figure 1.2 shows a type of split ring resonators (SRRs), where magnetic field of the incoming radiation needs to polarize along the y axis to excite the magnetic mode. We choose THz SRR with a lattice constant (a) of 50 μm for illustration. The simulated reflection (S_{11}) and transmission (S_{21}) can be seen in Fig. 1.2 (d). There is a transmission dip at 0.83THz in S_{21}, otherwise the spectrum is featureless. The current, electric, and magnetic field distributions of the resonant SRRs are shown in Fig. 1.2 (b) and the left and right panels of (c), respectively. In Fig. 1.2 (b) the oscillating currents for the inner and outer loops are both circulating counterclockwise resulting in a net magnet dipole moment pointing along the y axis, as evident is the

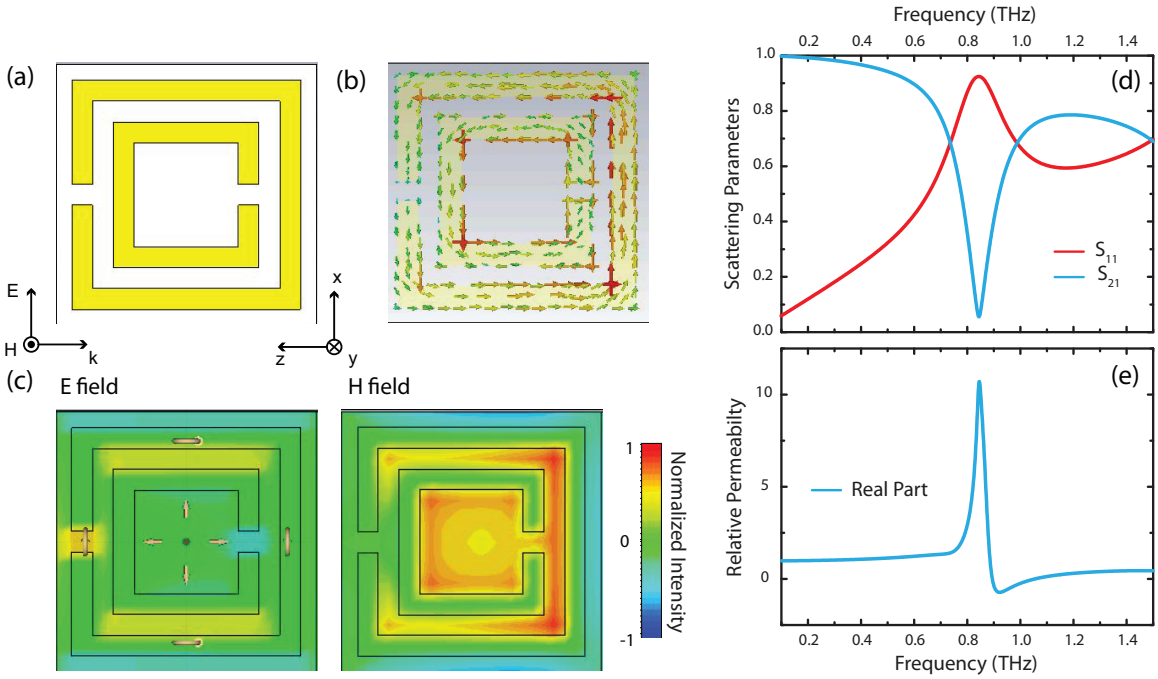

Figure 1.2: (a) A double split ring resonator (DSRR). (b) Current , (c) E (left) and H field (right) distribution of the DSRR at the resonance. (d) The simulated reflection and transmission for the DSRR with a = 50 μm. (c) The effective magnetic permeability of the DSRR.

$\tilde{H}$ field for both loops are in phase. In contrast, electric field along x axis in two capacitive gaps are out-of-phase indicating that there is zero electric dipole moment inside the unit cell (for the first order approximation). Optical constant retrieval procedure is then performed using Eq. 1.3 (We detail the formalism in Chapter 1.3.2). The extracted permeability shows a strong resonance at around 0.8THz occurring with the field analysis, see Fig. 1.2 (e).

To understand the resonant behaviors of the metamateirals[15], one can also employ the transmission line approach. For examples, SRRs can be described conceptually as an LC circuit[16], where L is the inductance associating with the length of the metallic loops and enclosed area by the ring, and C is the capacitance dictating how

strong the capacitive coupling between these splitting gaps. The resonant frequency can be described as $\omega_0 = \frac{1}{LC}$, and we later use this concept to construct a record-breaking subwavelength magnetic particles by maximizing L and C simultaneously, see Chapter 3 for the details.

1.1.2 Electric metamaterials

The properties of electric split ring resonators (ERRs) are in full analogy to those of SRRs except they are designated to be electrical[17, 18]. As a point of illustration, we choose a ERR which has two capacitive gaps laid in an opposite direction, see Fig. 1.3 (a). The fundamental resonance can be excited when incoming radiation has electric field polarized along x axis. The transmission (blue curves) and reflection spectra (red curves) can be seen in Fig. 1.3 (d). Similar to the spectrum of the SRRs, there is a prominent transmission dip happening in 1.1 THz, although the bandwidth is wider. Figure 1.3 (b) shows that the current of each loop flows in an opposite direction leading to a cancelation of total magnetic excitation - this phenomenon can also be observed from the magnetic field plot in the right panel of Fig. 1.3 (c). Electric field between two capacitive gaps, on the other hand, are in phase so that the electric dipole moment is non-zero. This concurs with the extracted relative electric permittivity in see Fig. 1.3 (e) evidencing that a strong Lorentzian-like electric resonance occurs at 1.1 THz.

1.2 Surface Electromagnetic Waves

As mentioned earlier, surface waves can travel along the interface between two different media without radiation[1, 2]. This implies that the field strength decays

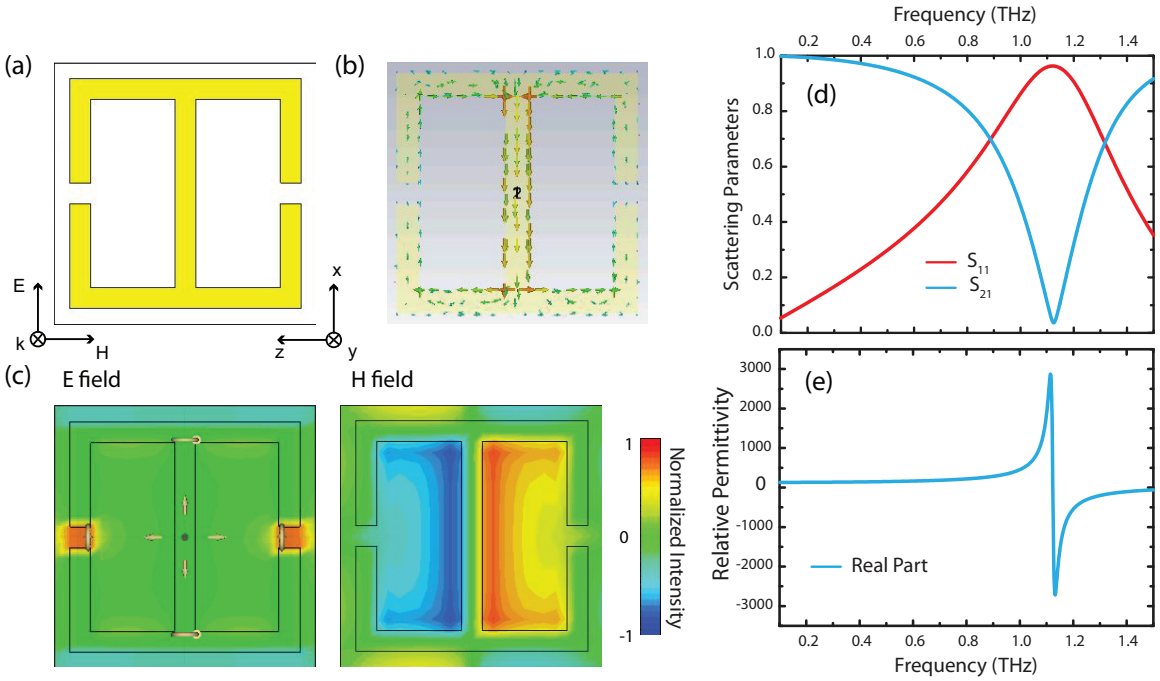

Figure 1.3: (a) A schematic drawing of a electric split ring resonator (ERR). (b) Current , (c) E (left) and H field (right) distribution of the ERR at the resonance. (d) The simulated reflection and transmission for the ERR with a = 50 μm. (c) The effective electric permittivity of the ERR.

exponentially on either side of the surface as the distance increases. This particular phenomenon can only occur when the optical constants of the host media, either ϵ or μ, possess an opposite sign with each other. Because of lack of diamagnetic materials in nature, there is no known magnetic plasmon until the birth of metamaterials. Another constraint for generating SEWs is the loss inside the metal needs to be sufficiently large. For the cases where the conductivity of the metal is high, electromagnetic waves cannot penetrate inside resulting in a weak coupling between SEWs and the metal. Electromagnetic energy stays unbounded in the interface and soon begins to leak. These leave the natural SPP waves to occur only at around ω_p, and makes their superior properties not available to other frequency ranges. As the

field of plasmonics poses more and more advantages, it is very desirable to extent this effect to other ranges. In 2004, John Pendry et al. theoretically proposed that by structuring periodic hole arrays electrons can spoof the plasmon behaviors and couple with light even when the metal is perfectly conducting - known as spoof or designer surface plasmons. A year later, Alastair P. Hibbins et al. [19] followed the concept and were successfully verified the existence of spoof SPPs in experiments. The breakthrough opens vast opportunities for both metamaterials and plasmonics. In Chapter 5, we show that these spoof plasmons can be tuned not only by the periodicity but also by the geometry.

1.3 Design and Fabrication

1.3.1 Computational Study

3D full wave electromagnetic simulators are performed before fabrication and characterization of the samples. The numerical methods are in essence solving Maxwell's equations for a specified optical environment. The space in the simulators is first divided into small grids and the solution at each point is calculated based on the given boundary conditions. For the regions where materials are present, light-material interaction can be modeled providing their frequency-dependent optical parameters such as conductivity, electrical permittivity, and magnetic permeability. There are different mathematical approaches, such as finite difference, finite elements methods, combination of both, and so on, each of which offers their own strategic advantages over different problems[20, 21]. In addition, these solvers can handle with Maxwell's equations in either the time or the frequency domain. The time domain method allows

the simulators to numerically calculate the scattering parameters over a large bandwidth in a computationally efficient manner. As for the frequency-domain method, it improves accuracy relatively to the time-domain solver by generating a more complex meshing.

1.3.2 Extraction of Effective Optical Parameters

However, numerical approaching is not always time-efficient when the structures are complicated, not to mention one needs to further optimize the responses of those. It is desired to gain deeper physical insights when tackling such problems. Thanks to the electrical small size of MMs, their optical properties can be described by a set of effective parameters, μ and ϵ, without examining all microscopic details. The optical constant retrieval process is based on the transfer-matrix formalism, where the complex reflection (r) and transmission coefficients (t) are related to ϵ and μ when MMs have a well-defined thickness of (d)[22, 23]:

$$\begin{aligned} t &= \frac{1}{\cos(nkd) - \frac{i}{2}(Z_r + Z_r^{-1})\sin(nkd)} \\ r &= -\frac{\frac{i}{2}(Z_r - Z_r^{-1})\sin(nkd)}{\cos(nkd) - \frac{i}{2}(Z_r + Z_r^{-1})\sin(nkd)} \end{aligned}$$

where k is the wavenumber of the incident wave and n is the effective refractive index of MMs, Z_r is relative wave impedance. n and Z_r can be used to obtain both ϵ and μ, see details in Chapter 2.

1.3.3 Fabrication

As for sample preparation, two dimensional lithographic techniques, such as photo-, ebeam- as well as printed-circuit-broad (PCB) lithography, are chosen depending on cost efficiency and fabrication tolerance. Since the working principle behind these methods is the same, we hence only illustrate the commonly used one among the three, the ultra-violent (UV) photolithography. To begin with, a thin layer of UV-sensitive photoresist ($\sim 1.2\mu$m) is spin coated on top of the sample wafer. In the next step, the wafer is illuminated with high power UV light through the quartz/Cr photomask. For the regions under illumination, the photo-resist undergoes chemical reaction and can then be removed by the developer. Metal deposition is proceeded on the photoresist mask on the host substrate. Copper/Au are among popular choices of microwave and terahertz applications since they both provide good conductivity. Following the lift-off procedure, sample fabrication is done.

1.4 Characterization

Spectroscopic measurements are performed in order to determine optical properties of the samples. We outline two of main experimental techniques for the sample characterization in the following sections: terahertz time-domain spectroscopy (THz-TDS) and Fourier transform infrared spectroscopy (FTIR).

1.4.1 Terahertz Time-domain Spectroscopy

Terahertz time-domain spectroscopy (THz-TDS) measures both real and imaginary portions of optical responses so that the dynamics within ultrafast materials can be resolved [24, 25]. A typical system covers a range from 0.1 to 1 THz with up to 1

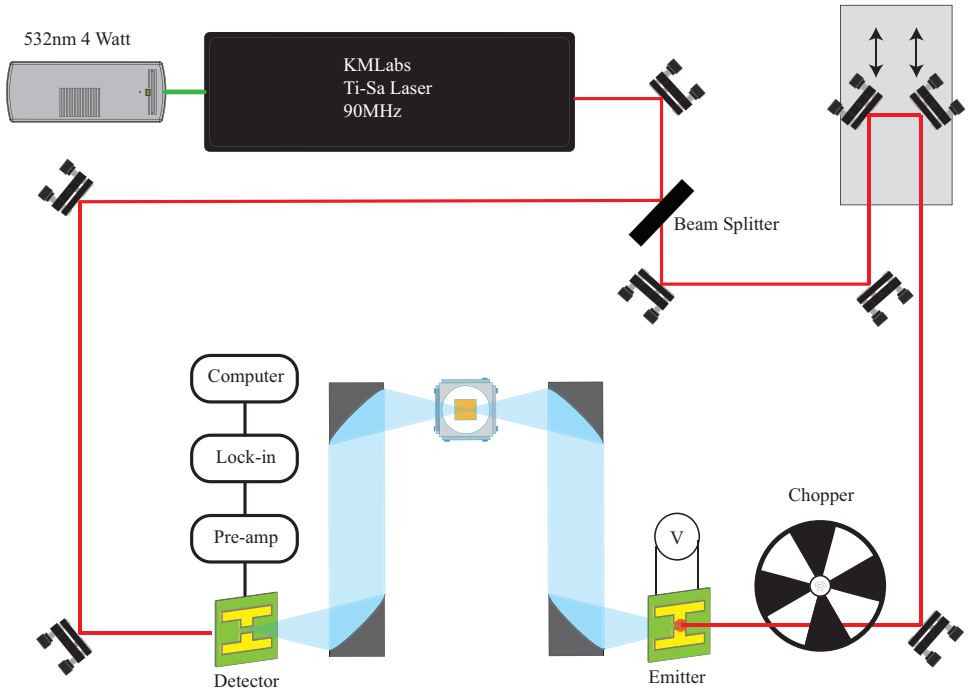

Figure 1.4: A schematic of the THz time domain system that was setup for the study of the single layer THz metamaterial discussed in Ch. 2 where we studied under what condition these artifical composites can have bulk-like optical parameters at the operation frequency.

GHz resolution and the bandwidth can further increase when the water is removed from the environment. The schematic drawing of a standard THz-TDS system based on photoconductive antennas (PCAs) is shown in Fig. 1.4. A 532 nm wavelength 4.5 W neodymium-doped yttrium aluminum garnet (YAG) laser beam is used to pump the titanium sapphire (Ti-sapphire) laser that generates an ultra-short pulse with the bandwidth of 100 nm and the center of spectrum at around 800 nm wavelength (100 fs in duration), at a repetition rate of 85 MHz. The broadband radiation is then split into two separate beam paths; one excites photo-induced charge carriers in an emitter and another in a detector. As shown in the Fig. 1.4, the beam at the detector

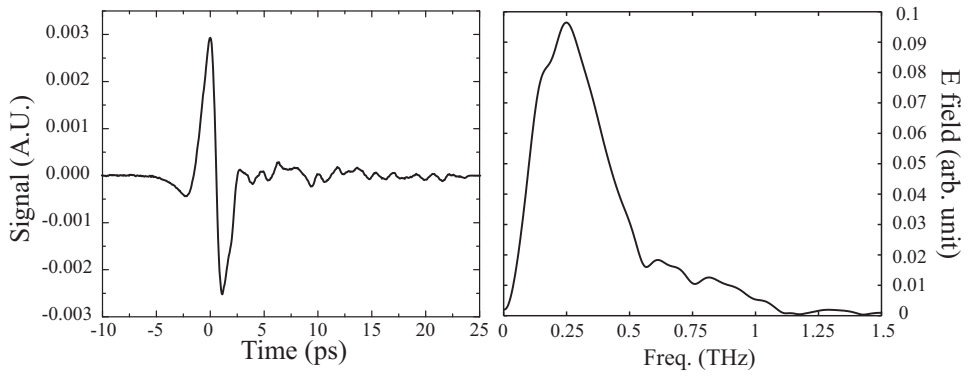

Figure 1.5: THz data collected by THz-TDS system with an open aperture reference. (a) The time domain waveform (b) The resulting spectrum calculated by taking the Fourier transform of the data shown in (a).

side goes through a controllable translation stage, where sub-picosecond time delay between these two routes can be introduced. Emission of terahertz radiation can be achieved by biasing photo-induced charge carriers in PCAs. As for the detection, the working principle is the same as the emission but in a reverse process. By scanning through the delay line a measure of the electric field as a function of time can be accomplished. Figure 1.5 shows a THz transient wave form collected by our THz-TDS system in the air. (a) The resulting spectrum calculated by taking the Fourier transform of the data shown in (a) after zero padding.

The detecting and emitting PCAs are dipole antennas with a gap of 10 μm on low-temperate grown (LT) GaAs substrates (Band gap of 1.42 eV = 874 nm), optical induced carriers of which have extremely short carrier lifetime. Other semiconductors, such as Er:GaAs nanoislands, or ion-implanted silicon-on-sapphire (SOS)[26], are also among the popular choices of PCA materials because of their superior electrical properties. Detecting currents in PCAs can be described as

$$I(t) \sim \int_{-\infty}^{t} \sigma(t)E(t-\tau)d\tau \tag{1.3}$$

where $\sigma(t)$ is the time dependent conductivity relating the free carriers optically excited in the substrate. The final signal is converted via a combination of a current-to-voltage preamplifier (with a gain of 10^9 (V/A)) and a lock-in amplifier. An example of the measured time waveform is shown in Fig. 1.5 (a). Figure 1.5 (b) demonstrates the Fourier transform of the time signal in (a) to obtain the frequency dependent complex electric field spectrum, and the spectral resolution is inversely proportional to the length of the temporal data.

1.4.2 Fourier Transform Infrared Spectroscopy

An alternative method to characterize spectral transmittance/reflectance of materials is using a commercial Fourier transform infrared spectroscopy (FTIR): Bruker Vertex 80 V, see Fig. 1.6. The spectrometry is based on concept of Michelson interferometer, where the inteferogram is obtained by modulating the difference between two beam paths[27, 28]. This instrument allows spectral measurements from 5 cm^{-1} to 50,000 cm^{-1} (free space wavelength of $\sim$ 2 mm to 200 nm), with a spectral resolution of 0.2 cm^{-1}(6 GHz) or better. This extremely large working range is accomplished by combining several sub detection bands. Each sub detection band is established when combining the source, the filter, and the detector. Take THz experiments as an example, the spectrum cover up to almost 3.5 THz when a mercury (Hg) arc lamp, thin mylar beamsplitters (6μm to 125μm), and the liquid helium cooled Si bolometer made by Infrared Laboratories are used. Figure 1.7 represents a measured interferogram of an open aperture collected by the FTIR with the configuration described

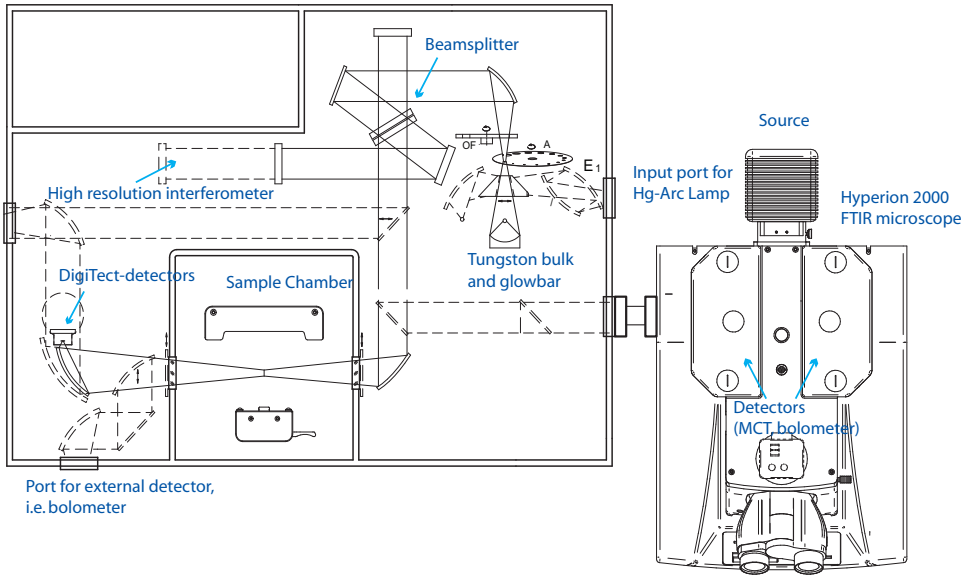

Figure 1.6: A schematic of the commercially available Fourier transform infrared spectrometer (FTIR). On the righthand side, a Hyperion 2000 FTIR microscopy is integrated into the main system providing a small beam spot size of 50 $\times$ 50 μm^2 for characterizing nano-fabricated samples.

above. Similar to TDS system, Fourier transform of the interferogram for either the sample or reference to extract the wavelength dependent intensity spectrum shown in Fig. 1.7 (b). By dividing the sample measurement with the reference, the transmittance/reflectance can be obtained. In addition, our system are also integrated with a beam condenser : Hyperion microscope which allows precise measurement of the sample area down to the sizes of 100 μm^2.

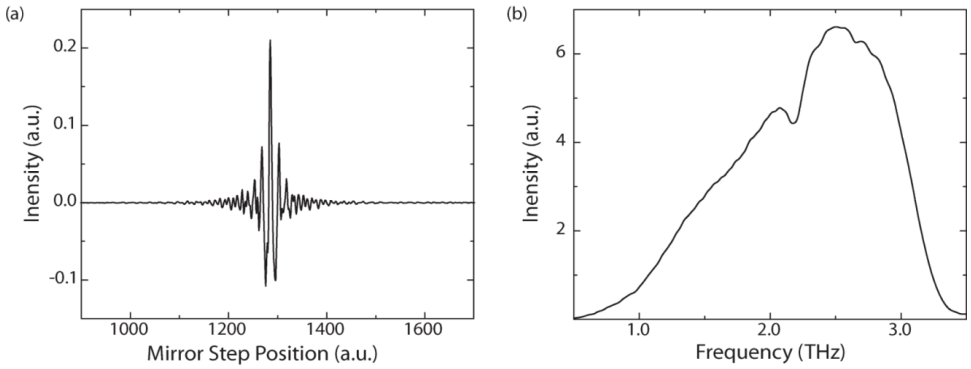

Figure 1.7: THz data referenced to an open channel collected by FTIR. (a) The interferogram plots the measured intensity as a function of mirror step position. (b) The frequency-dependent energy spectrum by Fourier transforming the interferogram shown in (a).

Chapter 2

Single Layer Terahertz Metamaterials with Bulk Optical Constants

2.1 Introduction

Since the theoretical prediction [29] and experimental verification of [30, 31, 32] a negative refractive index, the field of electromagnetic metamaterials has experienced enormous growth. The unique properties of metamaterials create possibilities for novel applications difficult to achieve with naturally occurring materials - cloaking [17, 8, 9] and superlensing [3, 5, 33] being two prime examples. Although the aforementioned cases largely motivate metamaterials research, arguably the real power of metamaterials stems from their ability to construct materials with a specific electric and magnetic response. In practice this is achieved *via* two different metamaterial unit cells able to independently control the two parameters which govern light-matter interactions in Maxwell's equations - the electric permittivity (ϵ), and the magnetic permeability (μ).

The ability to assign optical constants (ϵ, μ) to materials greatly facilitates the description of the interaction of electromagnetic waves and matter. However this

description is only possible when the wavelength (λ) is much greater than the element size (w), and distances between them (a), i.e. $\lambda \gg a > w$ [34]. Compliance with these 'sub-wavelength' requirements ensures that electric and magnetic fields vary slowly over the individual elements and therefore experiences an averaged response. The particular microscopic details may thus be ignored and the electromagnetic response may be described as that being due to the optical constants of a homogeneous material in the so called "effective medium regime" [35].

However the optical constants are intimately connected to the density of electric and magnetic dipoles within a material. For example the definition of the electrical permittivity is $\epsilon = \epsilon_0(1 + \chi_e) = \epsilon_0\epsilon_r$, where ϵ_r is relative permittivity and the electric susceptibility χ_e describes the relation between the electric field (E) and the polarization (P), which is equal to the number of electric dipoles per unit volume, i.e. $P = p/V = \epsilon_0\chi_e E$, where p is the number of electric dipoles, V is the volume, and E is the electric field. A similar definition exists between the magnetic permeability $\mu = \mu_0(1+\chi_m) = \mu_0\mu_r$ and the magnetization (M), that is $M = m/V = \chi_m H$, where μ_r is relative permeability, m is the number of magnetic dipoles, χ_m is magnetic susceptibility, and H is the magnetic field. Metamaterials, on the other hand, obtain their electromagnetic response from a combination of their geometry and p and m. That is, metamaterial unit cells are well described as effective electric or magnetic dipoles and the true number of dipoles due to the constituent materials is, to first order, not relevant, so long as metamaterials are fashioned from highly conductive structures, and operated below the plasma frequency of the metal. Since it is the metamaterial unit cell that is the effective fundamental dipole one may, by extension, assume that metamaterials should be volumetric in order to appropriately describe

their electromagnetic response by effective optical constants.

Metamaterials which extend significantly in three spatial directions are easily fabricated for operation at relatively low RF and microwave frequencies. These may be constructed using printed circuit board techniques thus permitting the assembly of bulk metamaterials. However at terahertz and higher frequencies it is typical to construct metamaterials consisting of a single layer on top of a substrate, owing to the relatively more complicated fabrication processes required - photo, electron beam, and/or focused ion beam lithography. Thus caution must be used when describing the optical constants of metamaterials at THz and higher frequencies as these structures do not significantly extend in a third dimension. As such, one must question the assignment of optical constants to all metamaterials which consist of a single or even of several layers.

There have been several works exploring the optical constants of single layer metamaterials [36, 37, 38, 39, 40], some of which term these structures "metasurfaces" [41, 42, 43]. Most works focus on obtaining ϵ and μ analytically and/or numerically, usually by direct inversion of the transfer matrix equations. Regardless of whether a metamaterial consists of a single or multiple layers, the transfer matrix method permits electromagnetic scattering of a medium of thickness d to be described as [44, 23],

$$t = \frac{1}{\cos(nkd) - \frac{i}{2}(Z_r + Z_r^{-1})\sin(nkd)} \tag{2.1}$$

$$r = -\frac{\frac{i}{2}(Z_r - Z_r^{-1})\sin(nkd)}{\cos(nkd) - \frac{i}{2}(Z_r + Z_r^{-1})\sin(nkd)} \tag{2.2}$$

where t is the transmission coefficient, r is the reflection coefficient, n is the index of

refraction, Z_r is the relative impedance, and k is the wavevector. The refractive index is defined as $n = c/v$ and the impedance as $Z = Z_r Z_0 = E/H$, where c is the speed of light in vacuo, v is the velocity of light within the medium, Z is the impedance, Z_0 is the wave impedance of free space, E is the electric field, and H is the magnetic field. However in effective medium theory a connection may be made between the optical constants and the index of refraction and relative impedance, i.e. $n = \sqrt{\epsilon_r \mu_r}$ and $Z_r = \sqrt{\mu_r/\epsilon_r}$. Equations (4.1) may be inverted to yield explicit equations for the index of refraction and the impedance. We may then also connect these directly to the optical constants, i.e.

$$n = \frac{1}{kd}\arccos[\frac{1}{2t}(1-(r^2-t^2))] = \sqrt{\epsilon_r \mu_r} \tag{2.3}$$

$$Z_r = \sqrt{\frac{(1+r)^2 - t^2}{(1-r)^2 - t^2}} = \sqrt{\frac{\mu_r}{\epsilon_r}} \tag{2.4}$$

An outstanding question in metamaterials research is under what conditions the right side of Eqs. 4.3 and 4.4 are valid [45]. In this paper we investigate the cases under which single layer metamaterials may be described by the optical constants, thus satisfying Eqs. 4.3 and 4.4. Two different structures are studied, each with two different layer thicknesses, in order to demonstrate various prototypical results. A series of simulations and experiments are performed in order to clarify the dependence of the optical constants on metamaterial layer thickness.

2.2 Design and Fabrication

We present two electric split ring resonator structures [46, 47, 48, 49] in single and multilayer configurations, which we term ERR1 and ERR2, see Fig. 2.1. For both

structures, the in-plane size of the unit cell is 50μm$\times 50\mu$m, and both the width and height of the metamaterial is 36μm, with a line width of 4μm. The capacitive gaps, found in the middle of the ERR2 structure and on the sides of the ERR1 structure, are 4μm. The metallic metamaterial layer is a 150nm thick layer of gold and is embedded (centered) within the substrate material, polyimide, giving a total unit cell thickness of either 50μm or 15μm , see Fig. 2.1. We term these two configurations as Type 50, and Type 15 based on their unit cell thickness. Each of these individual metamaterial unit cells (ERR1 and ERR2) of both substrate thicknesses (Type 50 and Type 15) are then stacked and we study n=1,2,3, and 4 layers of both structures and both types. Thus a total of sixteen different metamaterial samples are computationally and experimentally investigated.

Samples were fabricated with the dimensions shown in Fig. 2.1 (a) and (b) for ERR1 and ERR2, respectively. The structures were fabricated on layer-by-layer films of polyimide (PI-5878G HD Microsystems TM). Substrate thicknesses between adjacent metallic gold layers are chosen as mentioned above. Here we take the 50μm ERR1 as an example to demonstrate the fabrication process. First a 25μm layer of polyimide was spin coated on a silicon substrate and cured at 275^oC in an N_2 environment for 5 hours. Then the 150nm thick gold metamaterial was fabricated and patterned using optical lithography and lift-off techniques. For better pattern transfer, vacuum contact mode was used during the exposure process.. Substrate thickness is accurate to $\pm 1\mu$m. For samples with more than one layer, a second metamaterial layer was patterned in the same manner as the first. Alignment between the two layers was performed with a mask aligner which has an accuracy of 0.5μm. Additional layers of 50μm polyimide and 150nm gold can be coated and patterned in the

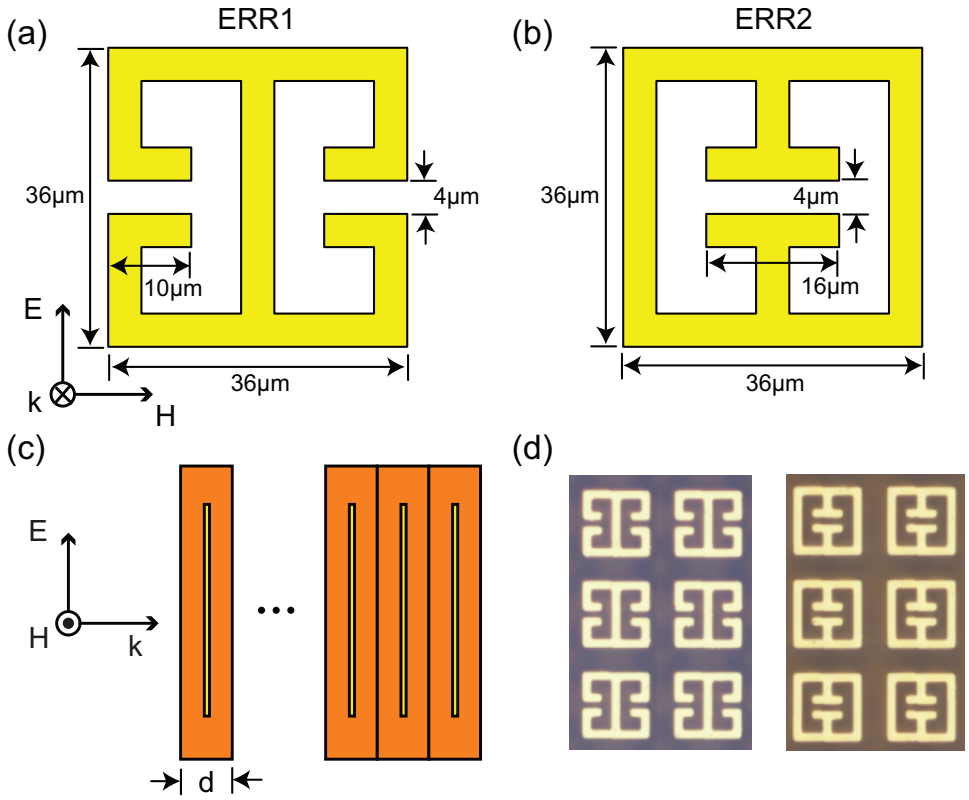

Figure 2.1: Geometry and dimensions of (a) ERR1 and (b) ERR2. Polarization of the incident electromagnetic radiation is shown in (a) for both ERR1 and ERR2. A schematic detailing the stacking of multiple layers is shown in (c), along with the the incident polarization specified. Microscopic photographs of the fabricated samples are shown in (d).

same way. For the last layer, a 25μm thick layer of polyimide was coated on top. In the final step, the entire multilayer sample, encapsulated in polyimide, was peeled off the silicon substrate, thus yielding a free-standing metamaterial multilayer structure embedded within the host dielectric material [50].

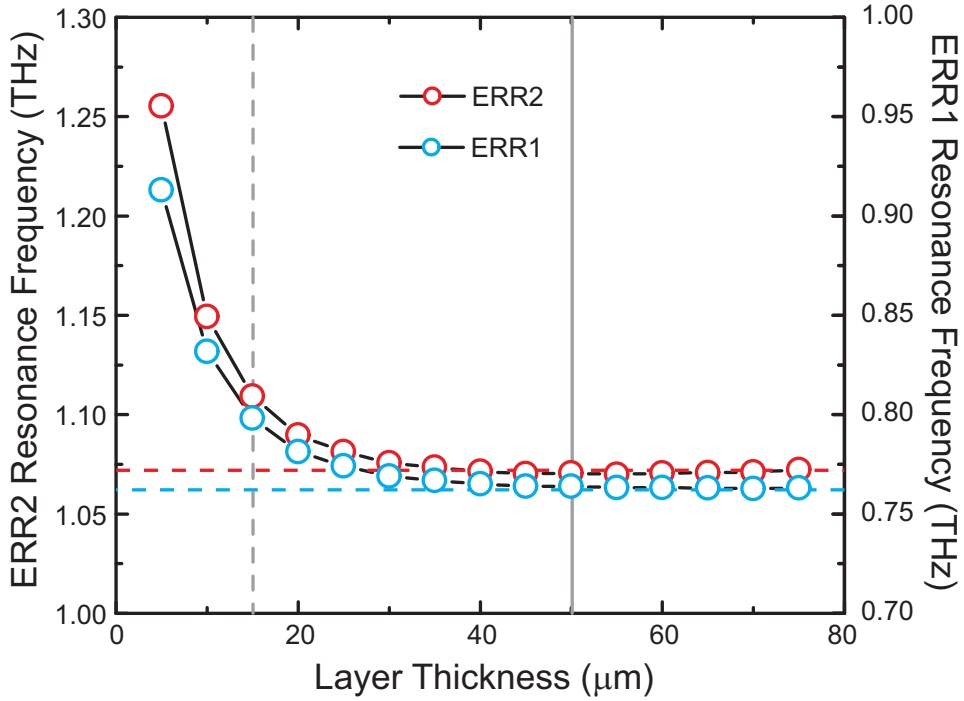

Figure 2.2: Dependence of the resonant frequencies of ERR1 (blue symbols) and ERR2 (red symbols) (single layer structures) on the embedding substrate thickness.

2.3 Simulation and Experiments

The structures were simulated with a commercial finite time domain solver, CST Microwave Studio. The metamaterial itself was modeled as lossy gold with a conductivity of $\sigma_0 = 4.56 \times 10^7$ (S/m). The embedding dielectric had a frequency independent lossy dielectric of $\widetilde{\epsilon} = 2.89 + 0.08i$. ERR1 and ERR2 are designed to have resonances at 0.76 THz and 1.07 THz, respectively. In Fig. 2.2 we show the dependence of the metamaterial resonance frequency, (for a single layer), on layer thickness (d) in the propagation direction, i.e. in the direction of $\mathbf{k}$ (see Fig. 2.1). In all cases, the metamaterial lies in the center of the dielectric layer. Dashed vertical lines at two different

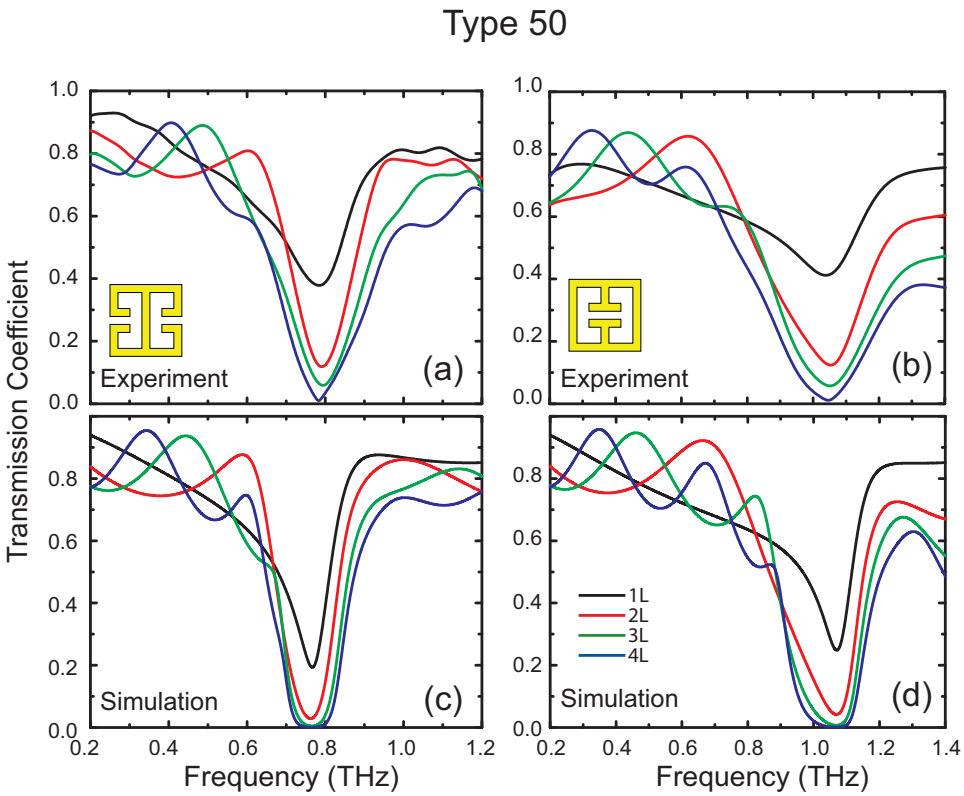

Figure 2.3: Experimental and simulated transmission coefficient for Type 50 metamaterials. ERR1 is shown in (a) and (c) and ERR2 in (b) and (d).

thicknesses show that, for both structures, the resonance frequency is continuing to change as a function of layer thickness for 15μm, but is saturated for 50μm. We simulated all sixteen metamaterial samples and performed extraction of the optical constants for each using Eq. (4.2). For the four layer metamaterial structure, with each layer being 50μm, the total thickness of the film is 200μm. With a resonance frequency for ERR1 (ERR2) of ω_1=0.76THz (ω_2=1.07THz), the corresponding resonant wavelength of λ_1=395 (λ_2=280) μm is comparable to its thickness.

Fabricated samples were experimentally characterized using terahertz time-domain spectroscopy (THz-TDS), which permits amplitude and phase measurements of the

transmitted electric field. A reference measurement was also characterized, (open channel), thus permitting determination of absolute transmission coefficient. Experimental data for all samples and reference measurements was collected over 25ps. The complex transmission coefficient permitted us to calculate the frequency dependent dielectric function through inversion of the Fresnel equations. Etalons resulting from multiple reflections within the metamaterial were incorporated into the extraction algorithm [51, 52].

2.4 Results

The transmitted electric field for each metamaterial ERR1 and ERR2 is shown in Fig. 2.3 (a) and (b) for a polyimide layer thickness of 50μm. We take the single layer ERR1 sample (black curve Fig. 2.3 (a)) as a point of discussion, which yields 90% transmission at 200GHz and at a frequency of 1.2 THz is about 80% transmissive. A minimum of 40% is observed at about 0.75 THz and the curve is otherwise featureless. Transmission for the other Type 50 ERR1 samples also each show minima near 0.75THz with values of 12%, 5%, and 0.1% for n=2,3, and 4 layers, respectively. Notice that, unlike the n=1 thick ERR1 transmission, other samples show oscillatory behavior beyond just the minimum near 0.75THz. For example the n=2 thick ERR1 sample (red curve), shows a local minimum of 72% at 450 GHz and a local maximum of 80% at 675 GHz. This local maximum seems to shift lower for an increase in the number of layers, i.e. 500GHz for n=3 and 425GHz for n=4 layers. This trend is also observed for the ERR2 metamaterial.

ERR1 with a 15μm thick substrate (Type 15), on the other hand, yields a transmission which does not seem to follow the same trend. For example the n=1 layer

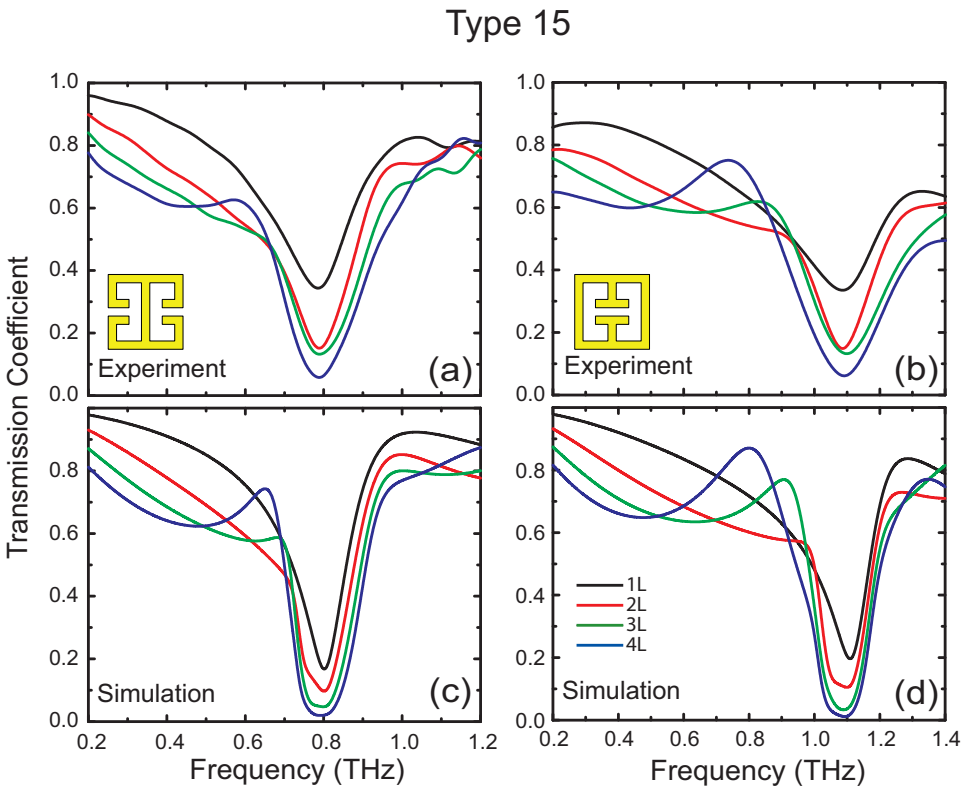

Figure 2.4: Experimental and simulated transmission coefficient for Type 15 metamaterials. ERR1 is shown in (a) and (c) and ERR2 in (b) and (d).

shown in Fig. 2.4 (a) shows a transmission minimum near 0.8 THz followed by maximum of 83% at 1.0 THz. The n=2 and n=3 layers are not so different with the maximum moving non-monotonically to 0.95 and 0.98 THz. In the n=4 sample a local minimum and maximum of 60% and 62% appear at 0.45 and 0.6THz, respectively. The 15μm thick ERR2 sample has roughly the same transmissive behavior.

In Fig. 2.3 (c) and (d) the simulated transmissions are shown for 50μm-thick ERR1 and ERR2, respectively. We achieve good agreement between simulated and experimental transmission, i.e. characteristic frequency dependent features discussed above for the experimental results are all observed in the simulated transmission.

Although the value of transmission maxima in the experimental and computational curves is similar, there is discrepancy in the minima. For example the simulated minimum for n=1 layer thick ERR1 sample (black curve) shown in Fig. 2.3 (c) is 25% compared to a value of 40% for the experimental curve (black curve in Fig. 2.3 (a)). A similar disagreement is found for all transmission data presented in Fig. 2.4.

The refractive index and the impedance of each configuration can be determined from the amplitude and phase of the transmitted electric field, see Eq. 4.1. For the electric metamaterials studied here, the structure is composed of two combined split ring resonators with identical sizes facing either inward or outward within a single unit cell. Magnetic coupling is thus forbidden by symmetry and the electric response dominates [17, 18]. We thus take the relative permeability $\mu_r = 1$ for each configuration such that the dielectric function can be obtained from Eqs. 4.3 and 4.4. Despite the periodic nature of multilayer samples, we take their total thickness to account for the relative difference in phase, (compared to a reference pulse), e.g. the phase change for a n=2 type 50 sample is calculated over 100 μm. The experimentally determined dielectric function for metamaterial samples with 50μm layer thickness are presented in Fig. 2.5 (a) and (b). The permittivity for ERR1 and ERR2 shows Lorentz like oscillators centered at ω_1=0.75 THz and ω_2=1.05 THz, respectively. As can be observed, there is little change in the permittivity for each sample for all layer thicknesses. There is, however, a discrepancy between the n=1 metamaterial and others for both ERR1 and ERR2.

Fig. 2.5 shows the simulated results for ERR1 (c) and ERR2 (d) with a substrate thickness of 50μm. Four different simulations are presented for each metamaterial, where the black, red, green, and blue curves are for n=1,2,3, and 4 layers thick,

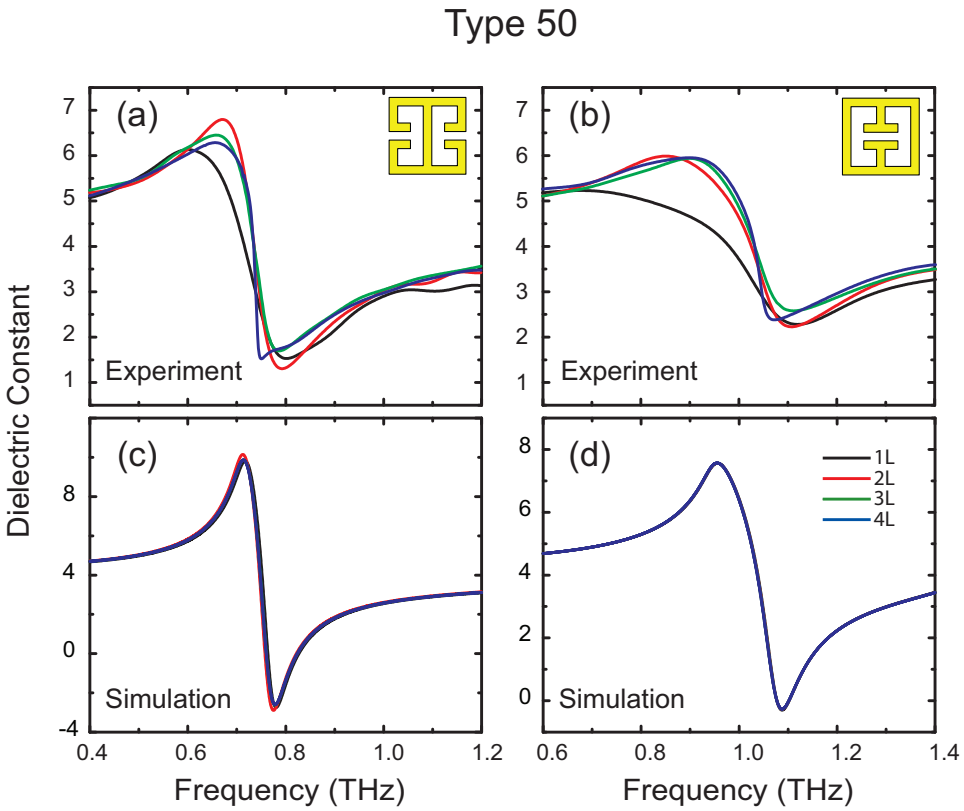

Figure 2.5: Experimentally determined dielectric function for Type 50 metamaterials for ERR1 (a) and ERR2 (b). Simulated dielectric function for Type 50 results for ERR1 are shown in (c) and ERR2 in (d).

respectively, in the propagation direction. As can be observed, the extracted dielectric function for all metamaterial single and multiple layer structures are identical, with no change in oscillator strength or cental frequency location.

In order to elucidate the nature of the above results, we also simulated and characterized the dielectric function for both ERR1 and ERR2 for a different substrate embedding thickness of 15μm (Type 15). Figure 2.6 presents results of this investigation where (a) and (b) shows the frequency dependent permittivity for both metamaterials and (c) and (d) show the corresponding simulations. It can be observed that

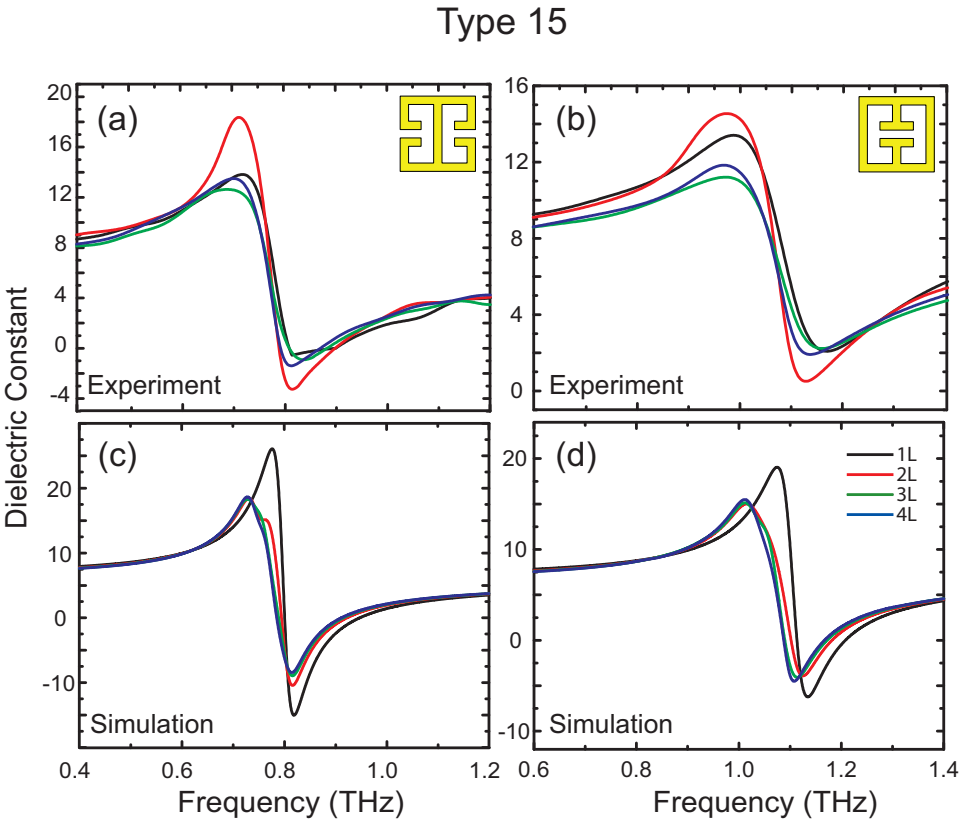

Figure 2.6: Experimentally determined dielectric function for Type 15 metamaterials for ERR1 (a) and ERR2 (b). Simulated dielectric function for Type 15 results for ERR1 are shown in (c) and ERR2 in (d).

the permittivity is seen to change for an increasing number of layers, from one to four (black, red, green, and blue curves). Specifically, for both ERR1 and ERR2, the resonance frequency red-shifts and the maximum peak amplitude decreases for multiple layers. Small variations in peak amplitude and peak position for each configuration are observed.

2.5 Discussion

It is evident that the optical constants, displayed in Figs. 2.5 and 2.6, for Type 50 and Type 15 samples behave differently, although they are comprised of the exact same metamaterial geometry (for both ERR1 and ERR2). As shown in Fig. 2.2, the resonant frequency of these metamaterials continually shifts to lower frequencies as a function of layers thickness, until finally asymptoting around 50μm. For the 50μm-thick samples, the saturated resonance indicates that the substrate is of sufficient thickness and dielectric constant such that there is negligible interaction between adjacent metamaterial layers. This shows that the electromagnetic response within a unit cell can be treated as a homogenous response, i.e. in the effective medium limit, and is independent of the number of layers. Thus in the Type 50 case, we may define a set of optical parameters for the single layer metamaterial which is equivalent to a bulk response.

In contrast the 15μm-thick samples yield significant interaction between adjacent unit cells, owing to the relatively thin substrate and dielectric value. When stacking multiple cells, the range of the layer-to-layer coupling exceeds the unit cell thickness and neighboring unit cells interact. Unlike the previous case, it would not be correct to describe a single layer 15μm thick sample by a set of optical constants, as $\epsilon(\omega)$ depends upon the number of layers. In our studies the response seems to saturate above six layers, (not shown), for the Type 15 metamaterials.

Our computational investigations suggest that metamaterials consisting of only a single layer may or may not be describable by the optical constants ϵ and μ. This depends on some key parameters, namely the embedding dielectric thickness, the complex dielectric constant of the embedding dielectric, the filling fraction, and the

particular type of metamaterial geometry, i.e. the symmetry point group and its relation to incident radiation [53]. A non-changing, layer independent, permittivity in the 50μm thick samples (Type 50) versus a gradually red-shifting permittivity in the 15μm thick samples (Type 15) is observed. Although this is clear in simulation it is apparent that there is some discrepancy for experimental measurements of single layer structures, both for Type 50 and Type 15 metamaterials. All experimental and simulated transmittance data (Fig. 2.3) match well, but the experimentally determined permittivities between the two cases (Type 50 and Type 15) is not as prominent as expected. This discrepancy can be attributed to the relatively weak mechanical strength of polyimide single layer films.

A thin polyimide film, although well characterized by optical constants [50], is highly flexible, mechanically weak and not self supporting. In the single layer case the as measured films surface is slightly modulated resulting in undesirable effects. We find that surface wrinkling leads to a non-uniform lattice parameter which presents itself as inhomogeneous broadening and thus a reduction in oscillator strength, (black curves in Fig. 2.5 (a) and (b)). In transmission this results in a lower absorptive feature and thus higher transmission. For example it can be observed that the disagreement between experimental and simulated transmission $\Delta T = T_{exp} - T_{sim}$ (Fig. 2.3 and 2.4) is worse for single layer metamaterials but gradually improves with more layers. If we take the minimum in transmission as our point of evaluation we find $\Delta T = 18\%$ for single layer Type 50 films. With the addition of more metamaterial layers an increase in mechanical strength is achieved and significantly less surface fluctuations were observed in the measurements of multilayer configurations for both 15μm and 50μm structures. Indeed ΔT diminishes for n=2,3,4 layers and is 10%, 6%

and 1%, respectively.

Simulated results shown for the Type 15 structures indicate that a significant red-shifting of the dielectric function occurs, due to interlayer coupling. As a result the optical constants of the 15μm thick metamaterial samples depend on the number of layers. Type 15 metamaterials achieve a more complicated and undesirable response compared to Type 50 (50μm thick) metamaterials. Although this may often be an unplanned interaction, this effect has been utilized in some cases to achieve unit cells with both electric and magnetic response [46, 54, 55, 56, 57]. Other examples include electromagnetic inducted transparency [58] and energy level hybridization [59, 58, 60]. It should be stressed that in order to define optical constants for a single layer metamaterial, any interactions that may occur due to the addition of other materials in proximity to the surface should be minimized.

As the optical constants of the Type 50 single layer metamaterials explored here are *equivalent to bulk*, we may calculate the number of electric dipoles involved in the electric responses shown here. Lorentz oscillators are fit to the simulated data, shown in Figs. 2.5 and 2.6, and described by,

$$\epsilon_r(\omega) = \epsilon_\infty + \frac{\omega_p^2}{\omega_0^2 + \omega^2 - i\gamma\omega} \tag{2.5}$$

where ω_0 is the center frequency of the oscillator, ϵ_∞ is the dielectric constant at frequencies much greater than ω_0, γ is the damping, and ω_p^2 is the square of the plasma frequency given by,

$$\omega_p^2 = \frac{ne^2}{\epsilon_0 m}. \tag{2.6}$$

where n is the number density (number of charges per unit volume $n = N/V$) involved in the oscillation, e is the charge of an electron, and m is the mass of an electron.

We may also connect the number of charges (N) involved in the metamaterial resonance to the electric dipole p from assuming a form for the electric dipole moment of,

$$\mathbf{p} = -Ne\mathbf{d}. \tag{2.7}$$

where d is the metamaterial gap of 4μm. Table 1 lists the parameters of Lorentzian fits to the dielectric functions of Type 50 ERR1 and ERR2, including the calculated number of charges N determined from Eqs. 2.5 – 2.7 and using a volume of V=L^3 where L=50μm for Type 50 metamaterials.

Type 50	ERR1	ERR2
$\frac{\omega_p}{2\pi}$ (THz)	0.69	0.82
$\frac{\omega_0}{2\pi}$ (THz)	0.75	1.04
$\frac{\gamma}{2\pi}$ (THz)	0.054	0.097
ϵ_∞	3.62	3.86
n (#/m^3)	7.40×10^{8}	1.05×10^{9}
p (C·m)	4.74×10^{-16}	6.69×10^{-16}

Table 2.1: Parameters of Lorentz oscillator fits to simulated Type 50 metamaterials.

As a general prescription for use of the optical constants for single layer metamaterials one may proceed as follows. First systematically explore the scattering parameters, (or effective dielectric properties - e.g. resonance frequency), of single layer metamaterials as a function of embedding dielectric thickness. Once this parameter asymptotes to a steady state solution one can be sure the fields (electric and

magnetic) have diminished to the point that any material placed at the metamaterial boundary will not affect its electromagnetic properties. Thus all the microscopic details of the single layer metamaterial may be ignored and considered to be truly homogenized and well described by the optical constants.

2.6 Conclusion

We have computationally and experimentally explored the conditions under which single layer metamaterials may be described by bulk optical constants. Two types of electric metamaterials were explored, both with two different sizes of embedding dielectric. The Type 50 configuration was a cubic unit cell with a lattice parameter of 50μm, and the Type 15 configuration was a tetragonal unit cell, with dimensions 50 $\times$ 50 $\times$ 15 μm^3. The tetragonal metamaterials were shown to yield layer dependent optical constants, whereas the cubic Type 50 metamaterials yielded layer independent optical constants. A Lorentz oscillator model was fit to Type 50 metamaterials which permitted determination of the total number of charges involved in the primary metamaterial resonance.

Chapter 3

Controlling Gigahertz and Terahertz Surface Electromagnetic Waves with Metamaterial Resonators

3.1 Introduction

Surface electromagnetic waves are propagating solutions to Maxwell's equations in which the electromagnetic energy is bound to an interface between two different media and travels without radiation loss. A common example is that of the Zenneck wave [1, 61], which is a propagating plane wave bound to a flat, conducting surface. Through the use of coordinate transformations, the Zenneck wave can be mapped to an axial cylindrical (Sommerfeld) wave [62, 63, 64, 65], or a radial cylindrical wave, both of which travel along the interface of a conductor - again without radiation. Initially some debated whether SEWs could exist in metals at low frequencies. This controversy arose due to the large conductivity of metals which leads to a weak binding of the wave to the surface. [62]. Although the existence and physical meaning of the Zenneck wave is a topic still debated to this day [66, 67], methods were developed

that enhanced the coupling of waves to planar surfaces, such as the use of dielectric coatings and surface corrugation [1, 68, 69], which can produce strong confinement even when the supporting metal is assumed to have an infinite conductivity.

Guided waves are of vital importance in routing electromagnetic energy from a source to a device or system and eventually to a receiver. Dielectric guides, hollow waveguides, and two-conductor transmission lines (e.g. coaxial) are typical examples and operate with extreme efficiency at very low frequencies (< 1 GHz).[70] Since filtering and other functionality is typically needed in communications applications, lumped components - such as packaged capacitors and inductors - can be implemented easily to form a wide variety of filter networks and other components that can be integrated into the line. However, the availability of packaged circuit components that operate at high frequencies is severely limited and, where they exist, such components tend to be rare and are generally expensive. At higher frequencies, the losses associated with conventional radio frequency (RF) cables and microstrip lines tend to rise, making them less suitable for integrated devices. At these higher frequencies, the properties of SEW devices become more favorable, making them competitive for integrated device applications, especially at terahertz and higher frequencies.

Over the past several years, metamaterial elements have been investigated for use as filters and other components in transmission line structures. Metamaterials (MMs) first garnered attention as structured, periodically positioned, metallic inclusions, able to attain designed electromagnetic response from their geometry. The size of individual MM elements, as well as the spacing between them, is considerably smaller than the free space wavelength at which the elements operate. As such, an electromagnetic wave incident on a collection of metamaterial elements experiences a

homogenized response that can be conveniently described by introducing the electric permittivity (ϵ) and the magnetic permeability (μ). MMs have been used extensively to form effective media, capable of supporting unusual electromagnetic properties such as negative refraction [30, 31]. Different types of MM geometries yield resonant responses to the electric and/or magnetic component of electromagnetic waves. Metamaterials are thus a "bottom-up" [71] approach for the construction of artificial electromagnetic materials and particularly useful in the implementation of graded designs, where the MM geometry changes as a function of position [58]. Such flexibility has been leveraged in the development of transformation optical media designed through use of coordinate transformations. By combining MM elements having distinct properties into a number of different types of sub-lattices [72, 73], even more complex electromagnetic response can be obtained.

In parallel with the development of metamaterials for the control of freely propagating plane waves, metamaterials have also been investigated as elements for the control of transmission line modes. There have been some works utilizing the so-called split ring resonator (SRR) [74], to couple with the magnetic component of light within a waveguide, or the complementary split ring resonator (CSRR) [75, 76, 77, 78, 79], for electric coupling on a coplanar waveguide (CPW) structure. In these systems metamaterials serve as parasitic elements producing stopbands [75, 76] or passbands [74, 79]. Other works have demonstrated MMs capable of more sophisticated responses, such as non-reciprocity [78] and dynamic tunability [80, 81, 82]. All of these works utilize metamaterials to couple to conventional transmission systems in which the electromagnetic energy is effectively confined to a region of space by means of two or more conducting structures; co-axial, co-planar, strip-line, slot-line,

etc. However, under certain conditions, other types of transmission may exist in which the energy is not rigidly confined but rather is bound to a *single* surface or structure and propagates without radiation - the surface electromagnetic wave. Such single conductor guiding structures may support three classes of waves - evanescent fields, radiation fields and guided surface waves; the latter of which can be made to predominate[83].

The ability to tailor SEWs with metamaterials may yield many practical future high frequency devices. However current metamaterial designs, when coupled to waveguides, yield low quality factors [74, 75, 76, 77] and therefore achieve a relatively broad band response, thus limiting the potential for switching or dynamic applications. Previously demonstrated metamaterial elements also significantly modify the impedance of CPWs, resulting in a significant reflection of incident energy. This leads to standing and scattered waves which may overwhelm the signal or reduce signal-to-noise. Both of these effects are due not only to the type of guiding structures utilized, (co-planar waveguides etc), but also due to the metamaterial elements used. Thus conventional 'free-space' metamaterials are undesirable for potential SEW devices and limit their usefulness for control. Although CPWs provide many advantages over other types of transmission lines the use of SEWs - as opposed to confined guided waves - may provide new opportunities for dynamical control using metamaterials. It is clear, however, that new metamaterial structures must be sought which are ideal to interact with the particular modes exhibited by SEWs.

Here we report on computational and experimental investigations of the control of SEWs with novel metamaterial elements. As a demonstration of the flexibility and scalability of the designs we show results over two bands of the electromagnetic

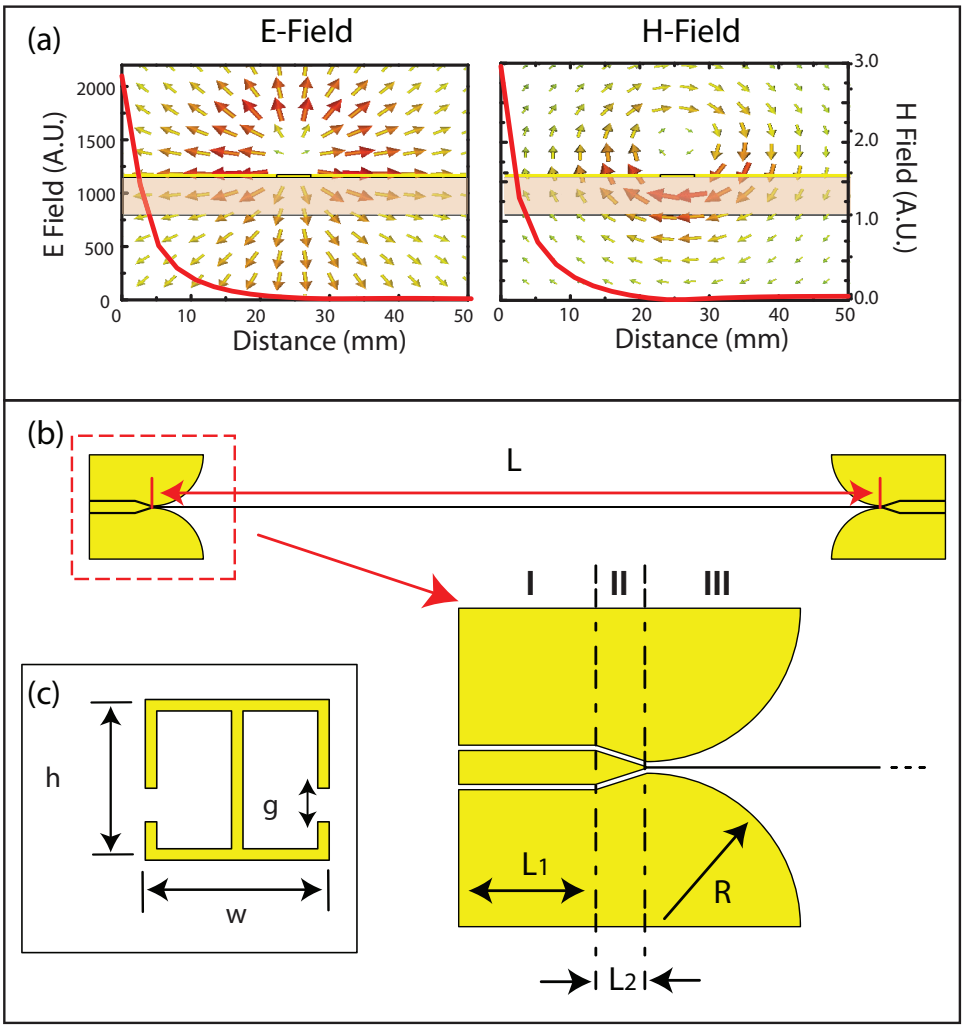

Figure 3.1: Simulated modes and dimensions of the planar Goubau line, and metamaterial schematic. Left panel of (a) plots the norm of the electric field strength as a function of horizontal distance away from the center of the GHz PGL, and right panel of (a) plots the norm of the magnetic field in the same manner. Insets to (a) show vector plots of the electric (left) and magnetic (right) field vectors. Panels (b) and (c) show the dimensions of the PGL, and metamaterial, respectively.

spectrum - gigahertz (GHz) and terahertz (THz) frequencies. For guiding of our electromagnetic wave we make use of a modified Goubau line, termed a 'planar Goubau line' (PGL) [84, 85], which is a single planar wire transmission line that lies on top of a supporting dielectric substrate. The geometry of the PGL is optimized to obtain a broadband spectrum. We further develop new metamaterial elements designed for maximum interaction with SEWs and demonstrate several examples.

3.2 Simulation

The PGL and metamaterial structures are simulated in the time domain with a commercial full wave electromagnetic mode transient solver. For the simulations, we use metallic conductivities with values of $\sigma_0 = 4.7 \times 10^7$ (S/m) and $\sigma_0 = 4.56 \times 10^7$ (S/m) and the underlying substrates are simulated as lossy dielectrics with values of $\widetilde{\epsilon} = 3.75 + 0.025i$ and $\widetilde{\epsilon} = 2.828 + 0.056i$, for the GHz and THz materials respectively. The GHz metallic structures have thicknesses of 17μm and supporting substrates are 200μm thick. In the terahertz regime, all metallic elements are 200 nm thick with a substrate thickness of 350 μm. The cross section (width x height) of the GHz PGL is 150 μm $\times$ 17 μm while the THz PGL is 4 μm $\times$ 0.2 μm. The total lengths are 320 mm and 5000 μm for the GHz and THz PGLs, respectively.

The PGL supports an approximately axial cylindrical SEW. The insets to Fig. 4.1(a) show a PGL in cross section, centered in each plot, with the supporting substrate shown underneath. Plotted in the insets to Fig. 4.1 are the electric (left) and magnetic (right) field vectors. The modes are transverse-electric-magnetic (TEM)-like, with the electric field directed uniformly radially outward and the magnetic field circulating clockwise around the wire. The red curves in Fig. 4.1 show the spatial

dependence of both the electric field strength (left) and magnetic flux density (right) beginning from the center of the wire and moving horizontally outward. Both fields fall off approximately exponentially.

In order to couple electromagnetic energy into and out-of the PGL we utilize a co-planar waveguide (CPW) section (Fig. 4.1 (b) section I), matched to 50Ω. The CPW transitions (see section II of Fig. 4.1 (b)) to a two-dimensional (2D), planar horn antenna (section III of Fig. 4.1 (b)), where the center conductor of the PGL line lies in the middle. The parameters that maximize the transfer of radiation for the GHz PGL, (and the total length of the PGL itself), are (in millimeters): L = 320, L1 = 20, L2= 7.5, and R = 20; and (in microns): L = 5000, L1 = 300, L2 = 300, and R = 800, for the THz PGL. In Fig. 4.2 (a) we show simulated results for each of the PGLs. Both exhibit large transmittance over a a broadband frequency spectrum with a usable range of 47 GHz and 384 GHz for the GHz and THz PGLs, respectively. For both lines, the simulated bandwidth is approximately 200% relative to the center frequency. Figure 4.2 (b) shows an expanded view of the simulated spectra of the GHz (solid blue curves) and THz (solid red curves) PGLs.

We seek to couple to the electric field of the PGL using a metamaterial element (inset to Fig. 4.1 (a)). As a starting point, we begin with the so-called electric ring resonator (ERR) [17, 18] element. The ERR has shown the ability to yield strong interactions with the electric field component of a free space TEM wave with good oscillator strength [18]. We optimize dimensions of the ERRs in order to obtain the highest quality factor (Q), defined as $\omega_0/\triangle\omega$ where ω_0 is the resonant frequency and $\triangle\omega$ is the FWHM of the resonance. The optimized geometry is shown in Fig. 4.1 (c), with the dimensions of g = 0.39, w = 2.4, and h = 2.1 for the GHz MMs and g

= 6, w= 105, and h = 90 for the THz MMs.

3.3 Fabrication and Characterization

Metamaterials and PGLs were fabricated with printed circuit board (PCB) technology (GHz structures) and optical lithography (THz structures), with dimensions identical to those simulated. The PCB is copper clad FR4 and the THz structures are nano-patterned gold deposited on a thin fused silica substrate. Masks were used for fabrication of both structures. Photographs of the fabricated PGLs are shown as the insets to Fig. 4.2 (b), and photos of the THz metamaterial / PGL structures are shown as the insets to Fig. 4.3 (a) and (b). All structures were characterized with Vector Network Analyzers (VNAs) operating separately in the gigahertz band from 8 to 20 GHz and the terahertz band from 0.22 to 0.325 THz. The complex frequency dependent scattering parameters - the transmission coefficient (S_{21}) and the reflection coefficient (S_{11}) - were characterized for the PGLs with and without metamaterials. All spectra were normalized with respect to a PGL with no metamaterial elements.

The experimental spectra of the PGL, shown in Fig. 4.2 (b) as the dashed blue (GHz) and dashed red (THz) lines, are in good agreement with simulated spectra (solid curves). Having characterized the spectra of each PGL, we now turn toward study of the interaction of metamaterial elements with the broad spectrum provided by the PGL *via* the transmissivity ($T(\omega)=|S_{21}|^2$). We calculate $T(\omega)$ by dividing the transmitted spectra of the PGL plus metamaterial by the transmitted spectra of the PGL alone. In the grey curves of Fig. 4.3 (a) and (b) we show the simulated absolute value $T(\omega)$ of metamaterial elements for both the GHz and THz structures, respectively. It is evident that only one prominent minimum is observed on each PGL and

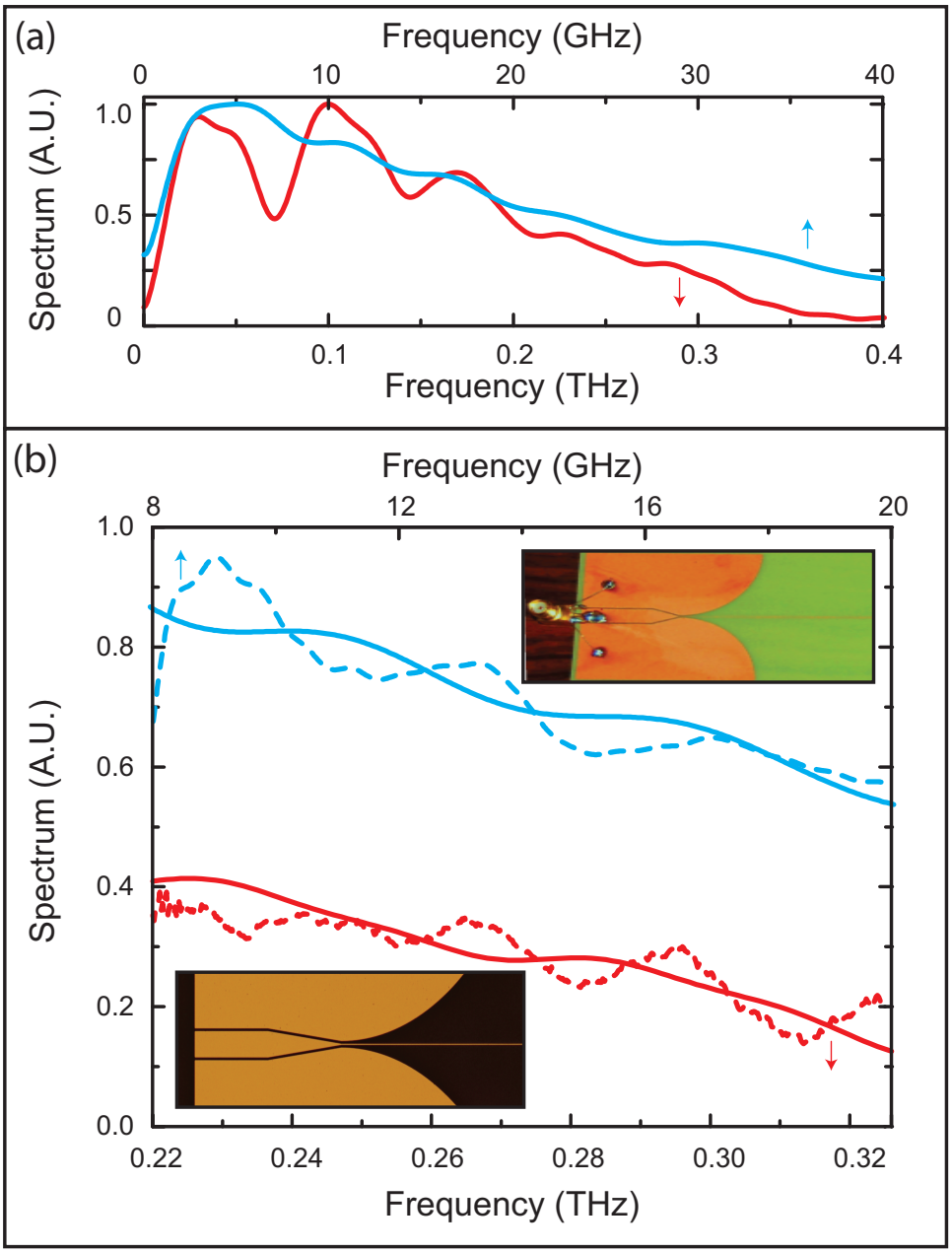

Figure 3.2: (a) Simulated spectra of GHz (blue) and THz (red) PGL waveguides. (b) Experimental (dashed curves) and simulated (solid curves) spectra for both the GHz (blue) and THz (red) PGLs. Insets are optical images of the gigahertz (top right) and terahertz waveguide (bottom left).

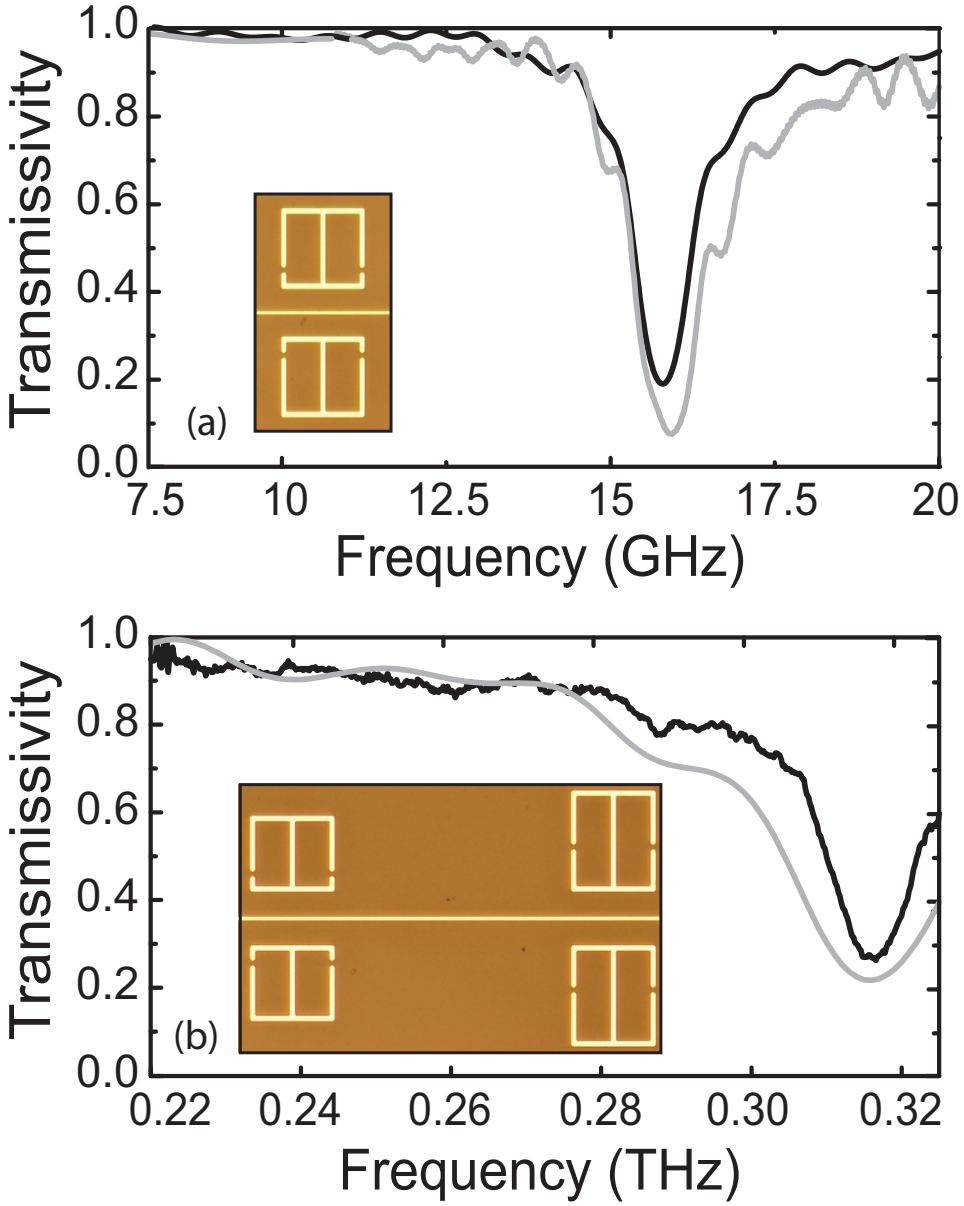

Figure 3.3: Simulated (grey curves) and experimental (black curves) transimissivity of (a) the GHz MMs and (b) THz MMs on PGL, two insets are optical images of single (top) and dual (bottom) THz metamaterial elements adjacent to the PGL.

values of T(ω)=8% at 16 GHz and T(ω)=21% at 0.315 THz are obtained. Simulations indicate Q-values of 10.3 and 10.5 for the GHz and THz metamaterials, respectively. Outside of the resonant region the PGL achieves over 85% transmission indicating that metamaterial elements yield only a narrow-band resonance. The normalized experimental transmissivity (black curves) of the GHz and THz metamaterial elements are plotted in Figs. 4.3 (a) and (b), and we observe good agreement with simulation (grey curves). Consistent with the simulations, we observe resonances around 16 GHz and 0.32 THz (see black curves in Fig. 4.3). A slightly higher transmitted energy and narrower bandwidth is observed, for both configurations, at the resonance frequency, and in each case the measured Q is higher than that predicted by simulation.

In order to verify absorption and coupling of the metamaterial element to the waveguide, we next explore a non-resonant metamaterial configuration and study the transmission dependence. We utilize a geometry similar to that previously published [86] - essentially an ERR in which the gaps are closed. This 'closed-gap' configuration has been shown to be non-resonant, as the capacitive portion of the metamaterial element has been removed. The blue curve of Fig. 4.4 (a) demonstrates that the simulated closed gap metamaterial elements do not couple to the SEW carried by the PGL, at least within the range characterized. Indeed the transmission is observed to be roughly frequency independent with values above 90%. For a direct comparison we re-plot the simulated T(ω) for a resonant (open gap) metamaterial element, and this is shown as the red curve in Fig. 4.4 (a). The experimental results match well with simulations, shown as the blue (closed gaps) and red (open gaps) curves of Fig. 4.4 (b).

Although we are only able to perform experiments over a narrow range of the

large bandwidth carried by the PGL, it should be possible to utilize multi-unit cell designs with which it would be possible to 'encode' more resonances onto the broad spectrum. We fashion a metamaterial which is slightly larger in size than the previously demonstrated element, shown in Fig. 4.3 (b). We simulate two different sized metamaterial elements, (shown as the inset to Fig. 4.3 (b)), which interact with the THz SEW - shown as the red curves of Fig. 4.4 (c). We observe a new resonant absorption in T(ω) at 0.260 THz while simulations indicate little change to the higher energy metamaterial absorption at 0.320 THz. With a view toward future dynamical or switchable SEW metamaterials we may again close the gaps of the metamaterial elements. The simulated results in which both resonators are in the non-resonant configuration are shown as the blue cures of Fig. 4.4 (c). There are no resonant absorption features observable and transmissivity is relatively featureless, with values of roughly T(ω)=0.8. To compare responses between the single and the dual metamaterial elements on the PGL, we re-plot the transmissivity for the single metamaterial with the gaps open, shown as dark grey curves of Fig. 4.4 (c). As can be observed there is little change in the higher lying resonance - it is essentially unaffected. Figure 4.4 (d) shows experimental measurements where both ERR elements are resonant (red curves), both ERRs are short circuited (blue curves), and the case where only a single metamaterial is resonant (grey curve). A comparison of the simulated and experimental curves of Fig. 4.4 shows relatively good agreement in all cases.

3.4 Discussion

We now highlight several salient features of metamaterial designs presented here. A notable difference between free space and surface wave metamaterials is that, for

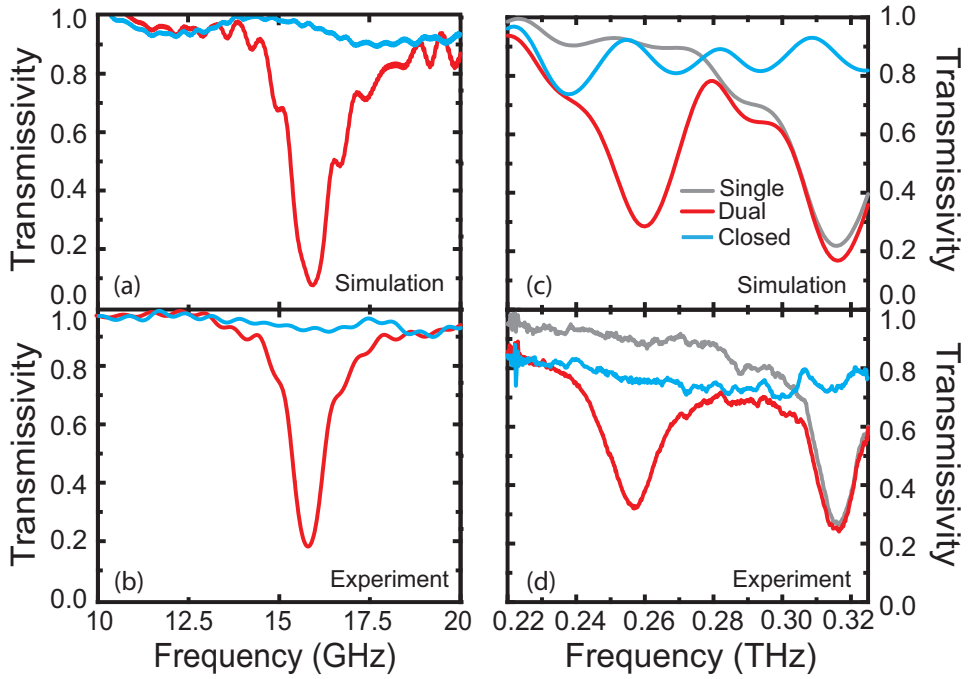

Figure 3.4: Simulated (a),(c) and experimental (b),(d) results of MMs on PGL - (a) and (b) are for the single pair case ; (c) and (d) for the dual pairs.

the latter, we only need two elements in proximity to the PGL. Although this is the case we still realize substantial electromagnetic response signified by large dips in the transmission. This is a bit surprising considering the small cross section the metamaterial elements occupy compared to the extent and homogeneity of the mode - see plot of the electric field in the inset to Fig. 4.1. However we must recall that the electric and magnetic fields fall off exponentially as a function of distance from the center of the line. Thus so long as the elements are spaced relatively close to the PGL the resonant dips yield relatively large Qs with experimental values of Q=14.9 and Q=18.4 at GHz and THz frequencies, respectively. In contrast, the non-resonant metamaterial element configuration attains relatively large frequency independent values for T(ω). Thus the resonant metamaterial elements are responsible for the

lack of transmission at the resonance frequency. Obviously energy in the broad band carried by the PGL which is not transmitted can be reflected, absorbed, or scattered by the metamaterial element. In Fig. 4.5 we present experimental results for GHz structures which reveal that energy is primarily absorbed by the metamaterial. As can be observed the reflection, (blue curve of Fig. 4.5), is essentially zero across the entire band, while the transmission achieves a minimum of approximately 20%. This means the metamaterial elements do not significantly modify the impedance of the PGL. Scattered radiation due to the metamaterial elements has been also studied in simulation, (not shown), and was negligible across the range shown in Fig. 4.5. Thus the energy which is not transmitted is absorbed by the metamaterial elements, as shown by the green curves of Fig. 4.5, with values reaching 80%. As shown in Fig. 4.4 (c) and (d) a second absorptive dip may be encoded onto the broad spectrum of the PGL *via* a different metamaterial element, with similar electromagnetic properties, i.e. strong absorption characteristics, as that of a single metamaterial element.

The strong absorption achieved by the metamaterial elements, in comparison to the high transmission achieved by the non-resonant metamaterial elements, suggests dynamical applications. For example, energy absorbed within the metamaterial elements is focused within the capacitive gaps of the structures. Thus utilization of field effect transistors or semiconductors placed within the gaps of the metamaterials would provide the ability to modulate the amplitude and frequency location of the resonance *via* electronic or optical means. Further, as shown in Fig. 4.4, these metamaterial resonances may be modulated independently. By adding more elements along the length of the PGL it may thus be possible to encode a large amount of information on the broad electromagnetic spectrum, which would enable high bandwidth

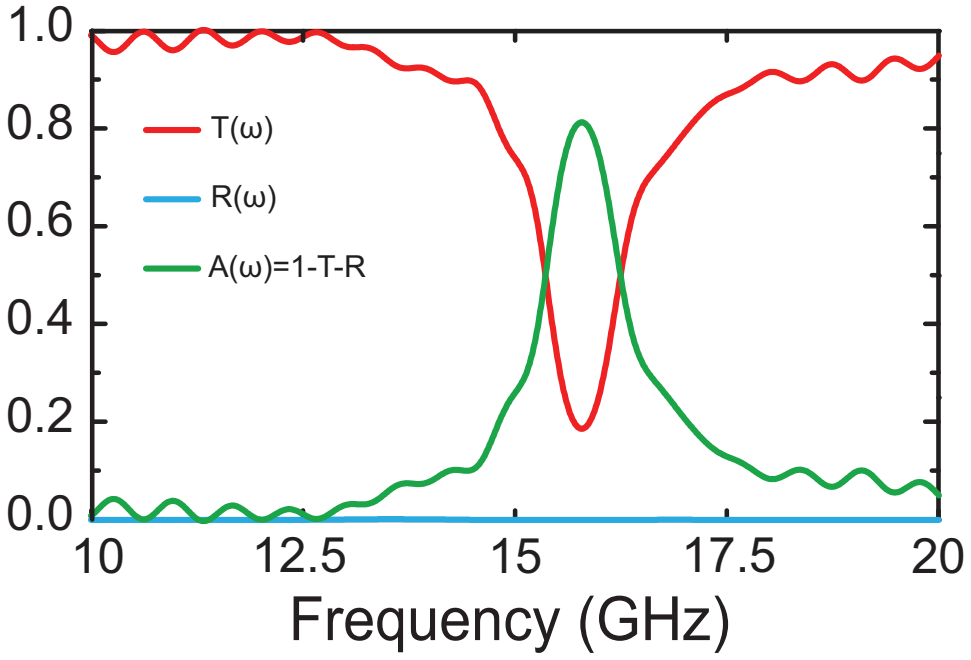

Figure 3.5: Experimental results of the reflection, transmission, and absorption of a GHz metamaterial interacting with the SEW carried by a PGL.

THz communication.

3.5 Conclusion

The planar Goubau lines explored here have been demonstrated to carry a wide band surface electromagnetic wave spectrum. Newly designed metamaterial elements have been shown to strongly interact with the particular mode exhibited by the PGL SEW and yield high Q resonances. Multiple metamaterial element resonances have been coded onto the broad PGL spectrum and independent shunting of each metamaterial resonance has been demonstrated.

Chapter 4

Extremely Sub-wavelength Planar Magnetic Metamaterials

4.1 Introduction

Experimental verification of a negative index of refraction[30, 31] confirmed a four decade old theoretical prediction[29] and initiated a new area of research in artificial electromagnetic (EM) materials[10], known as metamaterials (MMs). In the last decade metamaterials research has yielded many exotic effects including: invisibility cloaking[17], perfect lensing[3, 4], and perfect absorbers[87]. Interest in metamaterials stems from their available use in nearly any band of the electromagnetic spectrum and their ability to achieve almost any desired electromagnetic response[14, 16, 88].

While there are relatively few technical restrictions limiting operational frequencies of metamaterials there are, however, some practical hurdles. To date there has been a noticeable lack of metamaterials demonstrated at low frequencies – on the order of 100 MHz or lower. Traditional RF devices in use today cover a number of disciplines ranging from long range satellite communication, magnetic resonance imaging (MRI), to common everyday devices like radios and televisions. Although

metamaterials may offer advantages to the above mentioned devices, the main drawback is that the dimensions can become impractically large. Wavelengths for these frequencies range from thousands of meters (for 100's kHz) to lengths of meters (100's MHz). Since it is not uncommon for individual metamaterial elements to have sizes on the order of $\sim \lambda_0/10 - \lambda_0/100$, (where λ_0 is free space wavelength at resonance), the side length of a single RF metamaterial element could be expected be around 100 m to 10 cm. In many situations this size may be unacceptable for real-world applications, particularly so for 'portable' devices. The development of a new class of metamaterials with a significant reduction in the ratio of its physical size 'a' to its resonant wavelength λ_0 may create new opportunities for low frequency metamaterial-based applications[89, 90, 91, 92].

Magnetic properties exhibited by natural materials are typically weaker and less common than their electric counterpart. This is due to the fundamental difference in how magnetic and electric responses are generated - the former being produced either from orbital currents or intrinsic unpaired spins. This fundamental lack of diversity in materials hinders full development of electromagnetic devices. Metamaterials with a μ-negative response have been shown to improve the effectiveness of systems that make use of magnetic fields at radio frequencies such as increasing the resolution of an MRI[93, 94] and enhancing wireless power transfer efficiency[95, 96].

Here we propose that dual layer metamaterial spirals may be used in order to achieve extremely sub-wavelength RF magnetic metamaterials. We utilize and detail a time domain method for characterization of the complex magnetic response ($\mu(\omega)$) of the RF metamaterials and support experimental results with simulation.

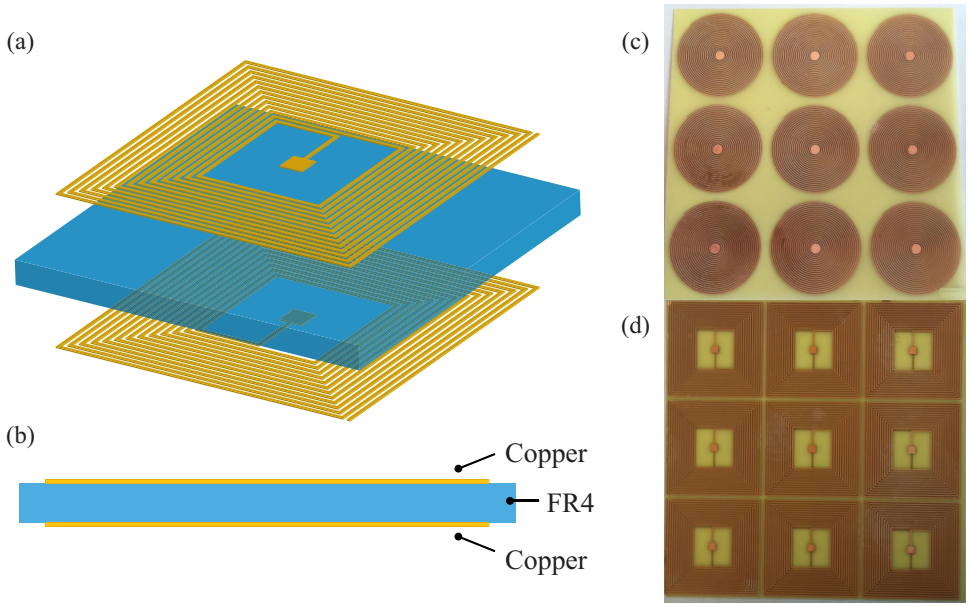

Figure 4.1: (a) Schematic (exploded view) of the dual-layer square spiral metamaterial. (b) Side view showing material layers. Photographs of fabricated metamaterial circular spirals (c) and square spirals (d).

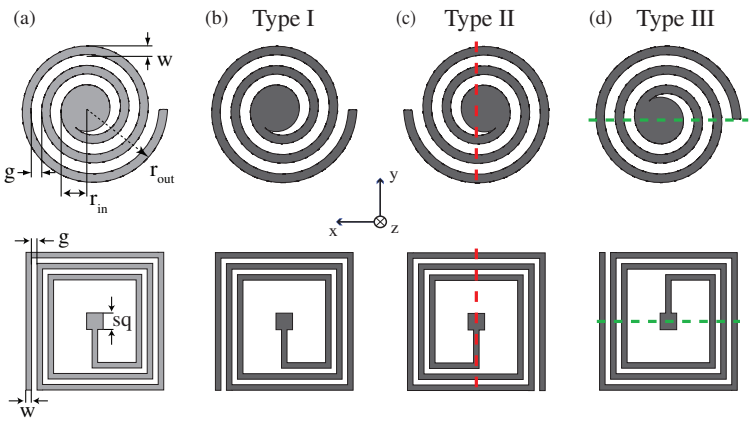

Figure 4.2: Schematic illustrating the geometry of circular (top row) and square (bottom row) spiral metamaterials. In the top of (a) the notation used for description of the geometry in shown. Column (a) shows the single layer structure, and (b), (c) and (d) show the orientation of the second spiral layer in type I, II, and III structures, respectively, as described in the text.

4.2 Spiral Metamaterial Design and Simulation

As a starting point for exploration of RF magnetic metamaterials we begin with a design based on a planar spiral structure capable of achieving large inductances[97, 98, 99] – as it is trivial to wind a significant length of wire into a small area. The spiral response can be approximated based on a simple LC resonator model $\omega_0 = 1/\sqrt{LC}$, where ω_0 is the resonant angular frequency, L is the inductance, and C is the capacitance of the MM. Additional reduction of the unit cell size may thus be achieved by maximizing L and C simultaneously. In single layer planar spirals the capacitance arises solely due to interactions between adjacent metallic windings - the so-called 'edge coupling' capacitance[100]. However, since typical lithographic methods produce extremely thin metallic layers the capacitive values obtained in this manner are small. We may drastically increase the capacitance by adding a second spiral layer, thus creating an interlayer interaction between the two planar structures. In this way both the larger area of the broadside metallic surfaces and a supporting dielectric in-between will provide an increased capacitance. A similar idea had been demonstrated in the microwave range, "the broadside-coupled" SRR was found to have a resonance occurring at much lower frequency than the original single layer design[101, 100]. The addition of the second layer will also provide an enhancement of the metamaterial inductance - so long as the inductances are added in series.

We investigate two different varieties of the planar spiral – circular and square windings. For each we consider three independent dual-layer configurations, termed as types I, II, and III. The paired spirals in each configuration represent different symmetry operations between layers. If we define a coordinate system that is centered in the middle of the two metallizations in the z-direction and centered laterally and

horizontally, then the type I spirals, Fig. 4.2(b), have two identical structured patterns on top and bottom layers, where the top layer is simply translated along the z-axis by some distance d. In Fig. 4.2(c) we show the type II case where the top and bottom layers have 180 degree rotational symmetry about the y-axis. In the type III case the top and bottom layers have 180 degree rotational symmetry about the x-axis. In all cases, metallic layers on each side of the substrate are capacitively coupled through a circular or square pad located in the center of the unit cell.

Simulations were performed with a commercially available 3D full wave finite element frequency domain solver. Excitation from a waveguide port is used where the electric field is along the $\hat{x}$ direction, and the magnetic field is along $\hat{z}$. The simulated circular spiral design has: 21 turns, a linewidth $w = 170$ μm, line spacing $g = 320$ μm, inner radius $r_{in} = 1.2$ mm, outer radius $r_{out} = 11.7$ mm, and unit cell size (a) of 25.4 mm. The square spiral has: 13 turns, a linewidth $w = 210$ μm, line spacing $g = 320$ μm, side length of the central capacitive pad $sq = 1.9$ mm, and the side length of the square coil is 25 mm with a unit cell size (a) of 26 mm. The dielectric slab for both patterns is 203 μm thick and was modeled using a dielectric value of $2.6 + 0.04i$. All metallic components were modeled as copper with a conductivity of $\sigma = 5.8 \times 10^7$ S/m. For all cases, a vacuum box $(a \times a \times 40(mm))$ was used, and the geometry of the spiral, including the size of the centrally located capacitive pad, was modified in order to obtain the greatest oscillator strengths.

Simulations provide the scattering parameters which are related to the transmission t and reflection r. The transfer matrix method then allows one to relate t and r

to a medium of thickness d as[23],

$$t = \frac{1}{\cos(nkd) - \frac{i}{2}(Z_r + Z_r^{-1})\sin(nkd)} \tag{4.1}$$

$$r = -\frac{\frac{i}{2}(Z_r - Z_r^{-1})\sin(nkd)}{\cos(nkd) - \frac{i}{2}(Z_r + Z_r^{-1})\sin(nkd)} \tag{4.2}$$

where n is the index of refraction, Z_r is the relative impedance, and k is the wavevector. The impedance is $Z = Z_r Z_0$, where Z_r is the relative impedance, and Z_0 is the wave impedance of free space. In effective medium theory we can relate the optical constants (ϵ_r and μ_r) to the index of refraction and relative impedance, i.e. $n = \sqrt{\epsilon_r \mu_r}$ and $Z_r = \sqrt{\mu_r/\epsilon_r}$. Equations 4.1 and 4.2 can be rewritten to yield explicit equations for the index of refraction and the impedance. We may then also connect these directly to the optical constants as,

$$n = \frac{1}{kd}\arccos[\frac{1}{2t}(1 - (r^2 - t^2))] = \sqrt{\epsilon_r \mu_r} \tag{4.3}$$

$$Z_r = \sqrt{\frac{(1+r)^2 - t^2}{(1-r)^2 - t^2}} = \sqrt{\frac{\mu_r}{\epsilon_r}} \tag{4.4}$$

Based on Eqs. 4.3 and 4.4, the effective permeability μ_r for each metamaterial design can be obtained from simulations.

The extracted permeability for each magnetic metamaterial is shown in Fig. 4.3(a) for the circular spirals and Fig. 4.3(b) for the square spirals. A single layer spiral design (Fig. 4.3 blue curve) was examined to act as a reference point for the dual layer structures. A prominent magnetic Lorentzian type resonance can be observed for each configuration described by,

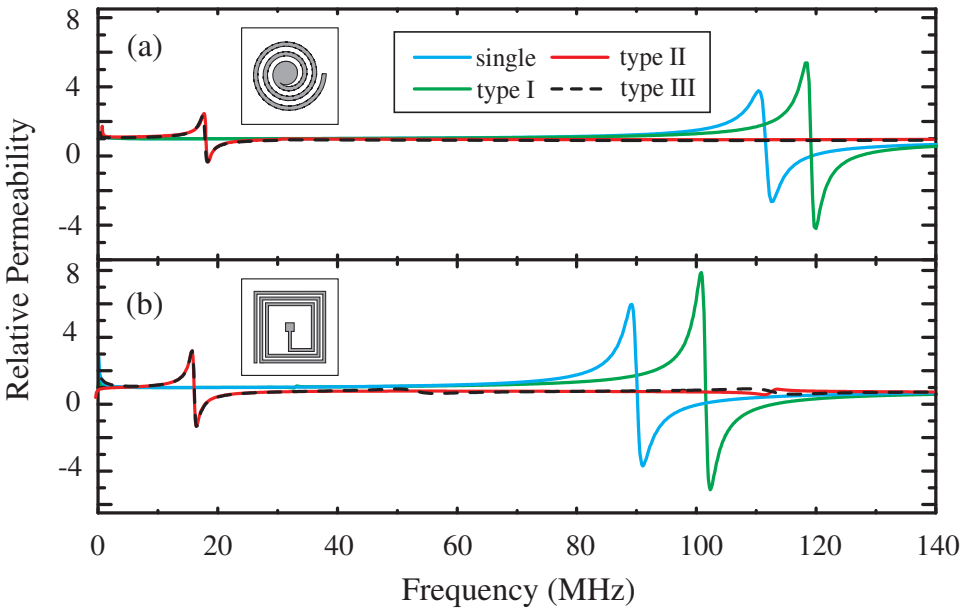

Figure 4.3: Simulated permeability of several different types of spiral metamaterials, the single-layer (blue curves), type I (green curves), type II (red curves), and type III (dash black curves).

$$\tilde{\mu}_r(\omega) = \mu_\infty + \frac{\omega_{mp}^2}{\omega_0^2 - \omega^2 - i\gamma\omega} \tag{4.5}$$

where μ_∞ is the relative permeability at frequencies higher than the resonance, ω_{mp} is the magnetic plasma frequency, ω_0 is the center frequency of the resonance, and γ is the loss. In Table I we list the parameters for a Lorentz oscillator fit to the simulated magnetic response - the resonant frequency (ω_0), minimum μ value, the oscillator strength ($\omega_{mp}/2\pi$), and the resonant wavelength to unit cell size ratio (λ_0/a). In the single layer case the resonance of the circular (c) and the square (s) spirals occur at frequencies of 112 MHz and 90 MHz. They both have good oscillator strength with values of 40 MHz for both. For the type I design (green curves of Fig 4.3), μ-resonances shifted to higher frequencies by approximately 10%, compared to the

single layer spirals, for both circular and square designs. Resonant frequencies for both type II and III configurations lie below 20 MHz and simulated oscillator strengths for these designs are lower than the single layer spiral and type I structures. It is clear, however, that Type III circular and square designs achieve the largest λ_0/a values and thus we have chosen to experimentally investigate these particular structures.

Table 4.1: Parameter values from fits to simulated μ_r for the circular and the square metamaterials shown in Fig. 4.3.

Type	$\omega_0/2\pi$ (MHz)	μ_{min}	$\omega_{mp}/2\pi$ (MHz)	λ_0/a
(C) single	112	-2.64	40	105
(C) type I	119	-4.20	41.7	99.3
(C) type II	17.8	-0.342	5.5	664
(C) type III	17.3	-0.357	5.8	683
(S) single	90.2	-3.97	40.4	131
(S) type I	101	-5.11	46.2	116
(S) type II	16.8	-1.51	6.95	703
(S) type III	16.7	-1.52	6.98	707

4.3 Magnetic Time Domain Spectroscopy

In order to characterize the complex permeability ($\widetilde{\mu}(\omega) = \mu_1 + i\mu_2$) response of our magnetic metamaterials, (μ_1 and μ_2 are the real and imaginary portions of the magnetic response function, respectively), we utilized a time-domain spectroscopic method. A schematic illustrating our experimental apparatus is shown in Fig. 4.4. In our setup a driving coil, (bottom of Fig. 4.4), is driven by a voltage pulse from a function generator creating a transient magnetic field. A second coil (pickup coil) is co-axially aligned with the drive coil, (spaced a distance z away) and measures the induced time dependent electromotive force ($emf(t)$) due to the incident magnetic field created by the drive coil. Based on the Faraday's law of induction, the induced

emf can be described as,

$$emf(t) = -\frac{d\Phi_B}{dt} \tag{4.6}$$

where Φ_B is the magnetic flux defined as,

$$\Phi_B = \int \mathbf{B} \cdot d\mathbf{A} \tag{4.7}$$

For a magnetic field component in the vertical (z-axis) direction at the pickup coil of B_z and an assumed time harmonic dependence ($\mathbf{B} \sim e^{-i\omega t}$), we may thus write the emf as,

$$emf(t) = -A\mu_r\mu_0\frac{dH_z(t)}{dt} \tag{4.8}$$

where A is the area of the pickup coil, and we have used $\mathbf{B} = \mu\mathbf{H} = \mu_r\mu_0\mathbf{H}$. It should be noted that, strictly speaking, we must convolve μ_r with the excitation field in Eq. 4.8. However for all cases studied here the resonant wavelength is at least 100 times larger than the size of metamaterials. Thus we are in the quasi-static limit [3] and neglect the time dependence.

In order to determine the complex permeability of a magnetic material we perform a referenced time domain measurement. This is achieved by first characterizing the response of the apparatus with no materials present, i.e. we measure a reference electromotive force of $emf(t)_r \equiv -A\mu_0 dH_z/dt$, since $\mu_r = 1$ for free space. We then place a planar material which has an area A into the pickup coil and characterize its time dependent electromotive force as $emf(t)_s \equiv -A\mu_r\mu_0 dH_z/dt$. Thus by taking the ratio of the time dependent emf's we are able to characterize the complex frequency

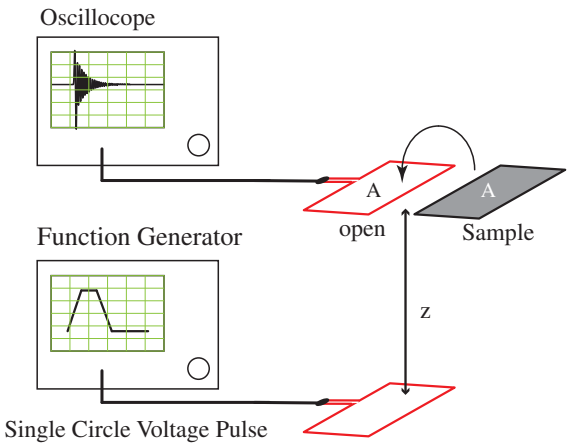

Figure 4.4: Schematic of the experimental apparatus as described in the text.

dependent permeability as,

$$\widetilde{\mu}_r(\omega) = \frac{\hat{F}(emf(t)_s)}{\hat{F}(emf(t)_r)} \tag{4.9}$$

where $\hat{F}$ stands for the complex Fourier transform. It's worth noting that in our experiment, the pickup coil can only measures a difference in electromotive force between the sample and reference. However, Maxwell's equations (specifically Ampere's law) specify that the bound current, which is related to the magnetization via $\bar{\mathbf{J}}_B = \bar{\nabla} \times \bar{\mathbf{M}}$, and thus to the magnetic permeability, is what changes upon placing a magnetic material in the loop of the pickup coil. As $\mathbf{H}$ is only related to the true free current, this remains constant in our measurements and thus cancels out for both the sample and reference measurements. Of course the above assumes that there is no change in the mutual coupling between the drive and pickup coils due to placement of the measured material, which would change the free current. We also note that there are no restrictions on homogeneity of the magnetic field and for the case where $\mathbf{B}$ has

a high spatial dependence the extraction method described in Eq. 4.9 is still valid. We use the time domain method described here to characterize the complex magnetic response of metamaterials. In all cases we have made the areas of the pickup coil and metamaterial samples equal.

4.4 Fabrication and Characterization

Metamaterial samples were fabricated using printed circuit board (PCB) photolithography. We used a dual sided copper clad FR4 board (thickness of 203 μm) where both metallization were 17 μm thick. A photomask for the square spiral geometry was created by printing on a transparency with a standard high resolution laser printer. For the circular spiral geometry a transparency mask was purchased from a commercial vendor. After the board was exposed to UV light through the photomask, a ferric chloride bath was used to etch away the unwanted copper to create patterned spiral metamaterials. The dimensions of both the circular and square geometries are identical to those in the computational models. Optical images of a unit cell of the fabricated samples are shown as insets to Fig. 4.1(c) (circular spiral) and (d) (square spiral).

The time dependent magnetic field used to characterize our metamaterial samples was generated using a coil antenna driven by a transient voltage. The peak to peak voltage (V_{pp}) was set to 10 V at a frequency of 12.5 MHz with a duty cycle of 37.5%. A receiving coil spaced a distance of 8 cm away was connected to a digital sampling oscilloscope which captured the time dependent electromotive force induced by the incident magnetic flux. The shape and dimensions of the receiving coil were chosen such that it matched that of a 3 $\times$ 3 array of our magnetic metamaterials. For each

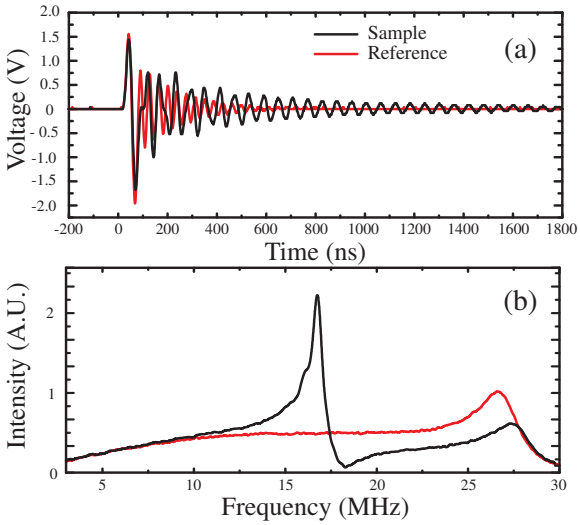

Figure 4.5: (a) Time domain waveform recorded by the pickup coil for the metamaterial (black curve) and a reference signal (red curve). The amplitude spectrum for the metamaterial (black) and reference (red) obtained by a Fourier transformation of (a).

sample we performed two measurements. The first was a reference where nothing was placed inside the receive coil. For sample characterization we placed the metamaterial array into the center of the receiving coil. All measurement were collected with an average of 128 wave forms.

Representative time pulses are shown in Fig. 4.5(a) for both the sample (black curve) and reference measurement (red curve). A noticeable difference can be seen between the two measured time pulses as the reference signal has almost completely died out after 600ns, while the metamaterial signal 'rings' for a much longer time (over 1800ns). A plot of the frequency spectra calculated from the Fourier transform of the time data is shown in Fig. 4.5(b). Applying the extraction method of Eq. 4.9, outlined earlier, one can determine the effective permeability μ_r of the magnetic metamaterials. Due to the dimensions of our antenna coils and the input time signal

characteristics the useable spectral range was 3-30 MHz.

The real and imaginary portions of the measured permeability of the samples are plotted as black curves in Fig. 4.6 for both the circular (top panels) and square type III (bottom panels) samples. As can be observed both spiral metamaterial structures yield magnetic resonances with Lorentz-like lineshapes. The circular spiral has its resonance centered at 17.3 MHz and the square spiral at 16.8 MHz. The real part of the measured relative permeability for both designs reaches a negative value of-0.25 for the circular design and -1.51 for the square design. The full width at half maximum (FWHM) is 0.554 MHz and 0.794 MHz for the circular and square designs, respectively. The calculated Q-factors are 30.3 and 21.8, which shows both designs have the decent oscillator strength at the resonances.

Simulated results of the type III spirals are as displayed as dashed red curves in Fig. 4.6. In comparison to the experimental results (black solid lines), the simulated curves are nearly identical to the measured ones. For example the simulated and experimental peak μ values differ by only 0.2% and 0.1% for the square and circular spirals, respectively. Some discrepancies in the amplitudes and Δf for both designs are observed. Nevertheless, the experiments are in excellent agreement with the simulations. The errors are most likely be attributed to imperfections from the fabrication process.

We compared experimental permeabilities to a frequency-dependent Drude-Lorentz oscillator, as shown in Eq. 4.5. The grey curves of Fig. 4.6 are fits to the experimental data and we find good agreement with parameters of: $\mu_\infty = 0.893$, $\omega_{mp} = 2\pi \times 4.91$ (MHz), $\gamma = 2\pi \times 0.745$ (MHz), and $\omega_0 = 2\pi \times 17.3$ (MHz) for the circular geometry, and $\mu_\infty = 0.87$, $\omega_{mp} = 2\pi \times 6.6$ (MHz), $\gamma = 2\pi \times 0.587$ (MHz), and $\omega_0 = 2\pi \times 16.8$

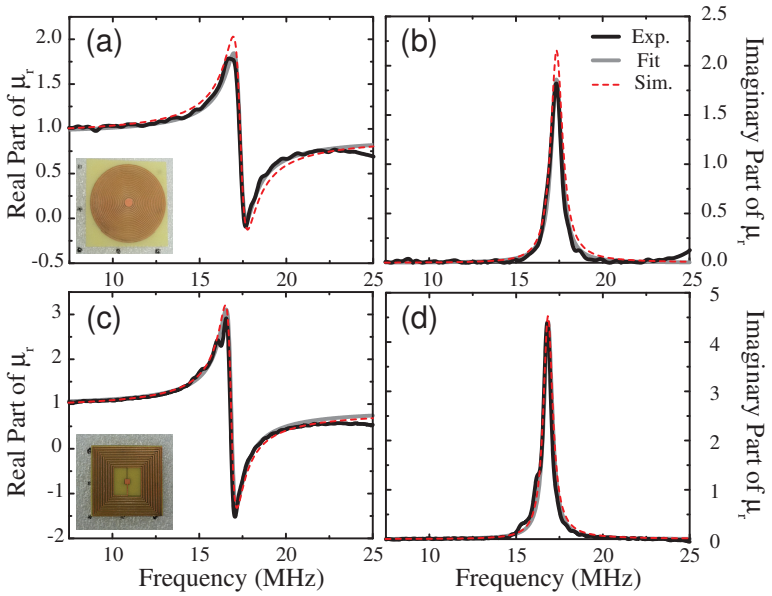

Figure 4.6: Experimental (black curves), simulated (dashed red curves) and fits (gray curves) to the real (a,c) and imaginary (b,d) parts of μ_r. Panels (a) and (b) show the real and imaginary permeability, respectively, for the circular spiral. Panels (c) and (d) show the real and imaginary permeability, respectively, for the square spiral.

(MHz) for the square geometry.

4.5 Discussion

Radio frequency magnetic metamaterials investigated here yield reasonably strong resonances although their physical size (a) is only a small fraction of their resonant wavelength. Circular spiral metamaterials achieved $a = \lambda_0/683$ and square designs $a = \lambda_0/703$. Resonant wavelengths of Type II and III designs are nearly six times smaller than λ_0 obtained from single layer spirals, although all have roughly the same unit cell size. It's worth noting that in-spite of the strong sub-wavelength sizes of

metamaterials presented here, there are simple improvements which will further increase λ_0/a. For example we have chosen to fabricate designs in which the two planar spirals are independent and are only capacitively coupled through the substrate. We chose this geometry simply because these structures are easier to fabricate, however by connecting the two layers with a conductive via one may push sizes of these structures even more sub-wavelength, as the unwound length effectively doubles.

Figure 4.7 presents simulations of a type III square spiral, with a connecting via, and a unit cell size $a = 15.5$ mm, linewidth $w = 100$ μm, line spacing $g = 100$ μm, board thickness of 203 μm, and consisting of 25 windings. Simulations indicate this design should exhibit a strong magnetic resonance at 9.34 MHz and the extracted complex μ is shown in Fig. 4.7(a). For this geometry we find $a = \lambda_0/2072$. Although the design discussed above is well within both laboratory and commercial fabricational capabilities, here we chose to experimentally demonstrate a slightly less subwavelength structure, and simply modify the type III circular spiral shown in Fig. 4.1(a) and (c). Holes were drilled through the center capacitive pad of each unit cell and a wire was soldered on both sides to create the connecting via. We then characterized the sample and extracted the complex permeability as shown in Fig. 4.7(b). We find a resonant frequency of 8.94MHz and thus this modified spiral magnetic metamaterial yields $a = \lambda_0/1321$. It should be noted that the experimental structure presented here was by no means an optimized design, i.e. we did not fine tune capacitive and inductive reactances which could be responsible for the significantly lowered oscillator strength. Additionally a notable Ohmic loss resulted from the manner in which the conductive via was experimentally implemented. The metamaterial geometry was simulated where the via was modeled as a resistive element (R=13Ω) and

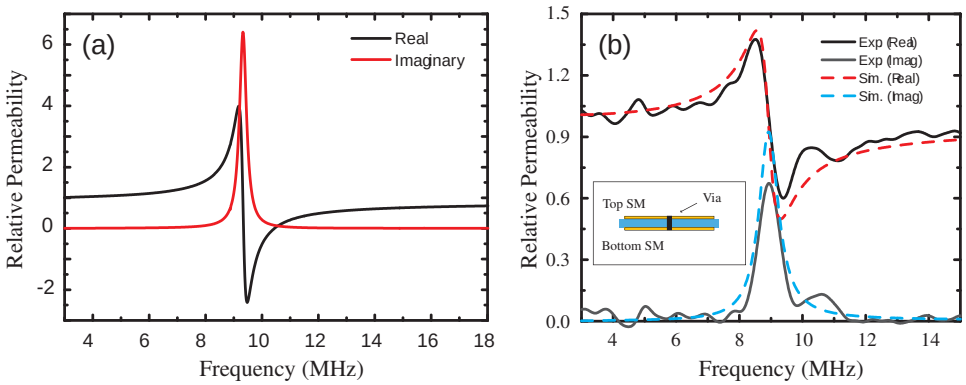

Figure 4.7: (a) Simulated real (black) and imaginary (red) relative permeability for a dual layer circular spiral metamaterial with an interlayer via. (b) Experimental (solid curves) and simulated (dashed curves) relative permeability of a type III circular spiral metamaterial with conductive via - described in the text.

we find excellent agreement with experiment as shown in Fig. 4.7(b).

Although the measured magnetic responses shown in Fig. 4.6 and 4.7 are well described by Lorentz oscillators, careful consideration of the assignment of $\mu_r(\omega)$ to metamaterials studied here should be given. As the permeability is equal to the number of magnetic dipoles per unit volume – and our metamaterials consist of only a single layer – one might by extension assume that metamaterials should consist of multiple layers in order to be appropriately described by effective optical constants. In this case it is clear that any response which results due to incident time varying magnetic fields, must happen within the physical bounds of the metamaterial, which has a volume of 0.237mm×a×a ∼150mm^3. More specifically in the case of the magnetic metamaterials investigated here, this can only be a re-arrangement of electrons within the conductive spiral itself. However it is important to note that the response fields significantly extend beyond the physical thickness and, in the direction normal to the plane, are only negligible at some distance (D) away. Thus any material placed

within D will effect the response of the metamaterial and thus alter μ_r. This is not, however, a barrier to specifying a unique permeability, so long as metamaterials are spaced a distance D apart in the z direction.

We investigate the uniqueness of μ_r both computationally and experimentally as its value should be independent of the apparatus and the particular spacing between the pickup and drive coils used. In simulations we investigated the dependence of the resonant frequency of a spiral metamaterial and dimensions of the bounding box along the direction normal to the metamaterial plane. As a point of demonstration, we show the simulated results for the square spiral case in Fig. 4.8(a). As the size of the bounding box increases, the resonant frequency also increases but eventually asymptotes to some value ω_0 (16.8MHz for the example). Computational investigations indicate that for both square and circular type III geometries the resonant wavelength saturates when the side length of the bounding box is around 40mm. At this layer spacing the fields of the metamaterial are small enough such that anything placed at or beyond this distance will not affect the response. We further verified this effect by simulating multiple metamaterials inside a unit cell and observing their responses. The extracted permeability for three different configurations is shown in Fig. 4.8(b). As we expect, even with the simulated unit cell composed of up to three metamaterial elements (the inset of Fig. 4.8(b)), the extracted permeability is nearly identical. This demonstrates that, in our case, both single and multi-layered metamaterials have exactly same permeability. Thus the simulated metamaterial element possesses 'layer-independent' optic constants and nearest neighbor effects may be ruled out.

As a verification to the validity of the experimental time-domain method presented

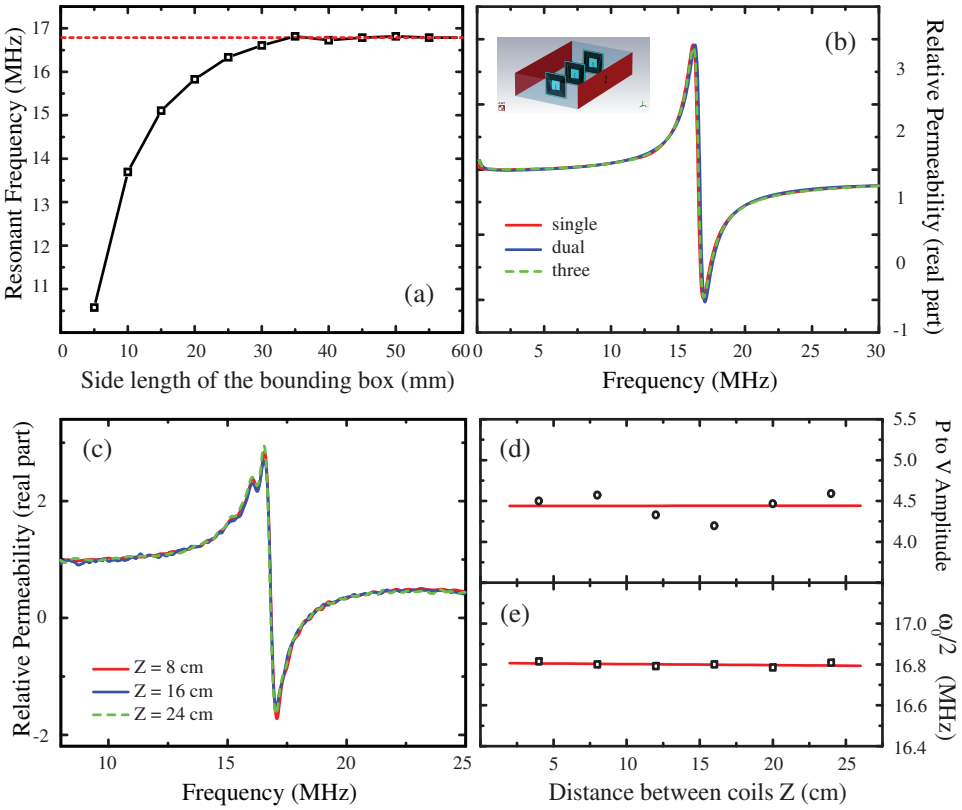

Figure 4.8: Simulated results: (a) Side length of the bounding box (vacuum) versus resonant frequency of square spiral metamaterials. (b) Extracted permeability of unit cell that contains single, dual, and three metamaterial elements. Experimental results: (c) Measured permeability for several values of coil separation z. The peak to valley amplitude of μ_r (d) and the resonant frequency ($\omega_0/2\pi$) (e) versus the coil separation distance (Z). Solids red lines are linear fits to the data.

here, we performed measurements of the response of magnetic metamaterials for several coil separation distances ranging from Z = 4 cm to Z = 24 cm. In all cases the sample under investigation was placed directly in the plane of the pick-up coil. As before all sample measurements were characterized and compared with a reference measurement. The induced maximum peak-to-peak value of the emf for the reference measurements was observed to change from 2V for the closest spacing to 40 mV for

the farthest. Calculated μ_r values are shown for three characteristic separations of Z = 8, 16, and 24 cm in Fig. 4.8(c). In Fig. 4.8(d) and (e) we plot, respectively, the peak-to-valley amplitude of μ_r and the resonance frequency ω_0, both as a function of coil separation. The red horizontal lines of Fig. 4.8(d,e) are fits to the data and have nearly zero slope to within 10^{-4}. The measured center frequencies only deviate by a maximum of 1% of the average value for z distances studied here. Variation, however, in the peak-to-valley μ_r values is as much as 5% though we attribute this discrepancy to noise in the system.

4.6 Conclusion

We computationally and experimentally demonstrated extremely sub-wavelength planar magnetic metamaterials. Experimental resonant wavelength to unit cell size values were shown to be as much as ∼1300, and an ideal simulated design was shown to be $\lambda_0/a \sim 2000$. We find excellent agreement between experimental and simulated magnetic permeabilities, for all structures investigated, and attain reasonable oscillator strengths. A novel characterization method has been presented capable of determining the complex magnetic response of planar materials at RFs. Compact sub-wavelength designs presented here make low-frequency study of metamaterial practical which may lead to RF metamaterial applications.

Chapter 5

Characterization of Surface Electromagnetic Waves and Scattering on Infrared Metamaterial Absorbers

5.1 Introduction

Metamaterial absorbers (MMAs) [102] are a type of engineered material that obtain near-unity absorption of electromagnetic energy at a specified wavelength. The MMA operates by achieving an impedance ($Z(\omega)$) match to free space, while at the same time providing high loss - as determined by the imaginary portion of the index of refraction ($n_2(\omega)$). A unit cell of the MMA often consists of two metallic layers (typically one patterned and one continuous) with an insulating layer lying in-between. The unit cell is subwavelength and periodic in the plane. The patterned metallic layer is an electric ring resonator (ERR) [17, 18] and provides a Lorentz type resonant electric response ($\epsilon(\omega)$). The ERR interacts strongly with the underlying metallic layer and a resonant effective magnetic response ($\mu(\omega)$) can be obtained. The first realization of such a structure was experimentally demonstrated at microwave

frequencies [46] and designs were quickly shown in the THz [50], infrared [103, 60] and optical regimes [104]. The thickness of the MMA is small compared to the free space wavelength of light thus yielding large absorption coefficients. The above mentioned salient features of the MMA suggest they may be used to replace conventional absorbers and to enable novel applications, such as frequency-selective detectors [105], emitters [87] and spatial light modulators [103].

Metamaterial absorbers operating at infrared and optical wavelengths utilize a simpler ERR geometry compared to designs demonstrated at THz and lower frequencies [103, 60, 104]. This permits the MMA to be fabricated more precisely, with less errors, thus producing higher yield and hence greater performance. The consequence, however, is that the unit cell size (a) is not as sub-wavelength as geometries utilized at lower frequencies. Experimental results have shown that the resonant wavelength to unit cell size (λ_0/a) is typically around 3 or 4 at infrared wavelengths. Although IR MMAs are still able to obtain high absorptivity, with values of 98% shown [103], it is unknown when the scattering ($D(\omega)$) becomes non-negligible as the wavelength and unit cell size become close in dimension. Incident energy may further generate surface electromagnetic waves ($S(\omega)$), which may then be dissipated or re-radiated [2, 1, 106, 107]. Thus in a normal specular characterization, both diffuse scattering and excitation of SEWs may appear as absorption. To date no investigation has accounted for all possible light-matter interaction that may occur upon the surface of a MMA. Here we experimentally and computationally investigate the role of $D(\omega)$ and $S(\omega)$ to absorption in infrared MMAs. We demonstrate that scattering is small and not relevant in the absorption process, but that highly lossy surface electromagnetic waves are generated upon the MMA in TM polarization.

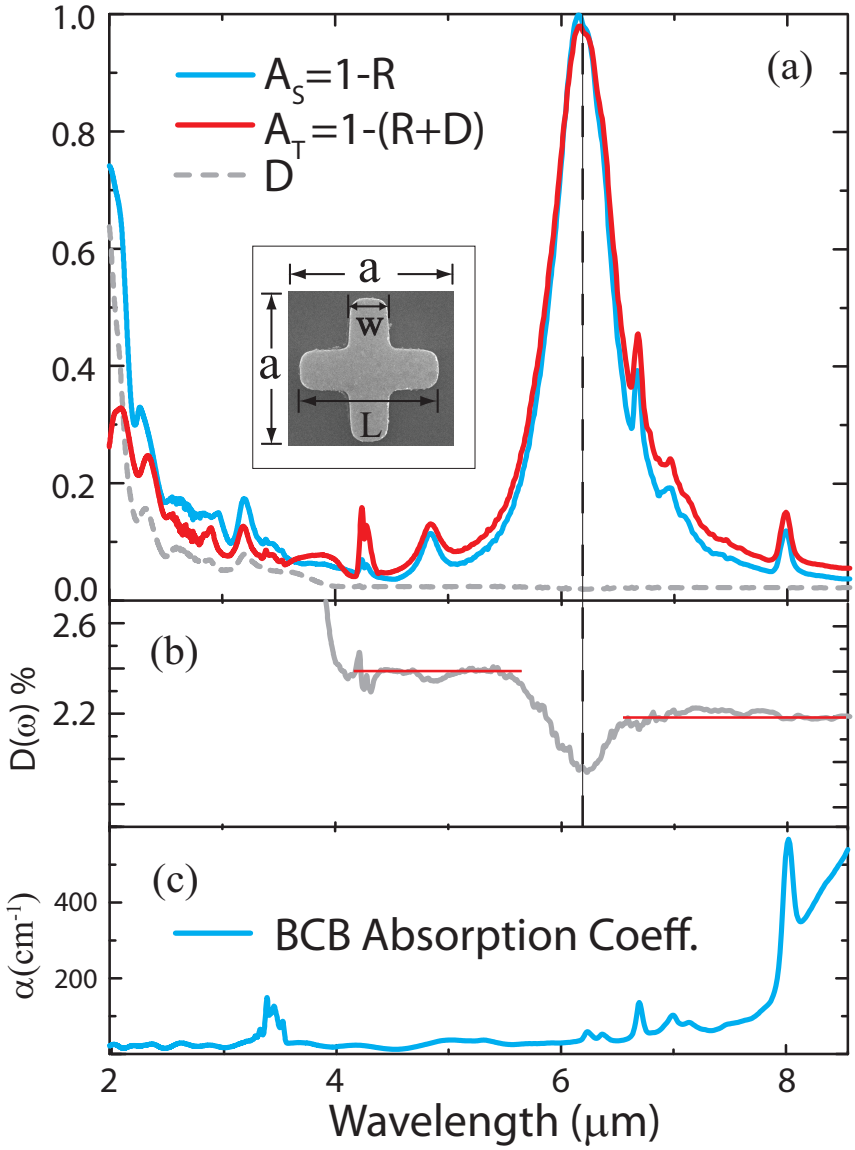

Figure 5.1: (a) Experimental diffuse scattering $D(\omega)$ (dashed curve), the specular absorbance A_S (blue curve), and the total absorbance A_T (red curve) of the IR MMA. The inset shows an SEM image of the fabricated sample with dimensions: $w = 500$nm, $L = 1.95$ μm, and $a = 3.2$ μm. (b) An expanded view of $D(\omega)$ from 2-8.5μm detailing the global minimum at 6.13μm, as denoted by the vertical dashed line. (c) Experimental determined absorption coefficient of BCB.

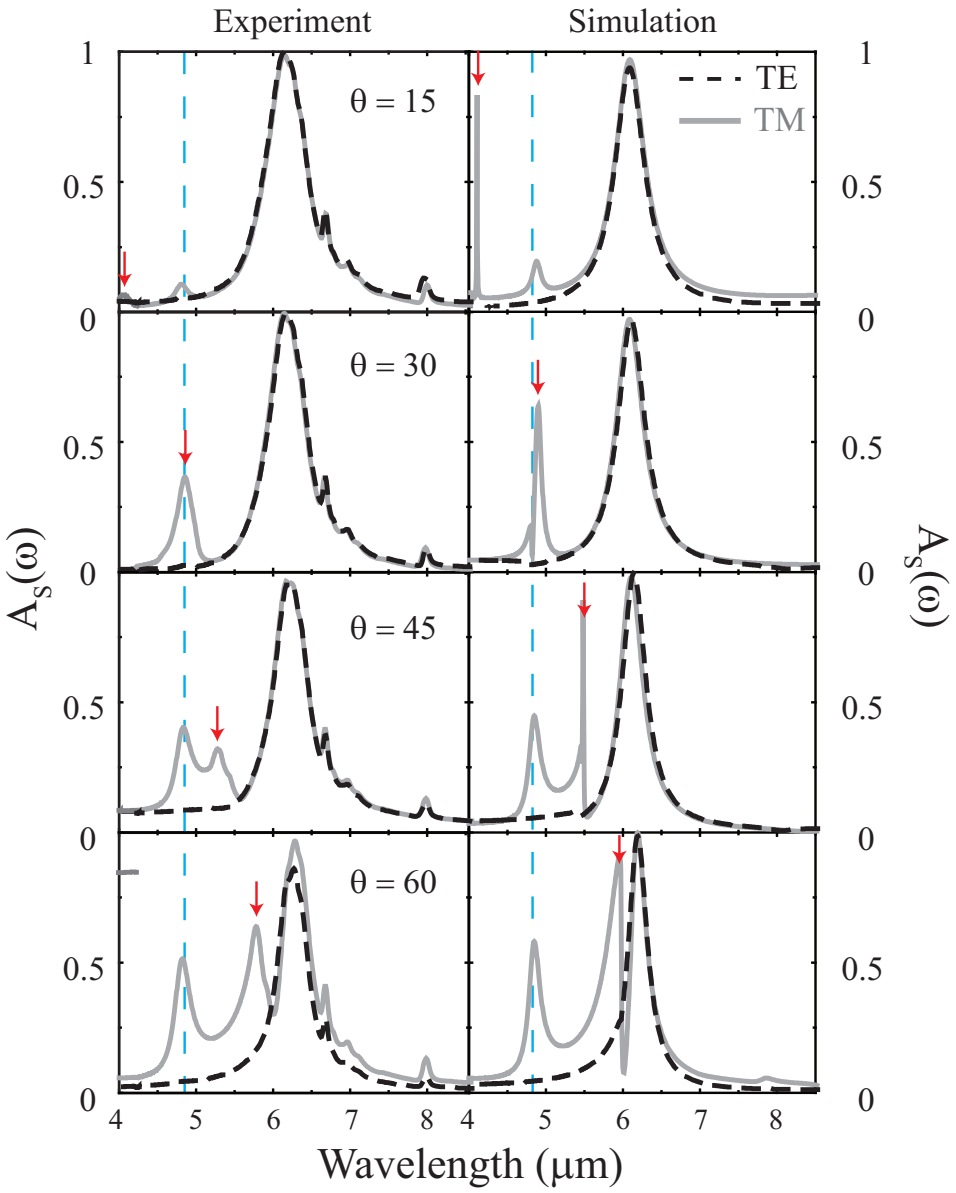

Figure 5.2: Experimental (left panels) and simulated (right panels) frequency dependent specular absorption for various incident angles (θ) in both TM (grey solid curves) and TE (black dash curves) polarizations.

5.2 Fabrication and Characterization

The infrared metamaterial absorber sample was fabricated using thin-film processing combined with photolithographic patterning. The first step was the electron-beam vacuum deposition of a 3 nm Cr adhesion layer followed by a 100 nm thick gold ground plane. The dielectric spacer layer of the MMA is a 195 nm thick film of benzocyclobutene (BCB) which was spin coated onto the ground plane and thermally cured under vacuum. Next, deep UV lithography is used to pattern the metamaterial elements in the UV lithography resist, and a 3 nm Cr adhesion layer followed by 75 nm thick gold layer are then deposited onto the nanopatterned sample. After performing lift-off of the Cr/Au, the remaining Cr/Au forms the MMA elements. A scanning electron microscope (SEM) image of a MMA unit cell is shown as the inset to Fig. 1(a). The patterned MM cross has the following dimensions: linewidth w = 500 nm, and side length L = 1.95 μm, with a unit cell size a = 3.2 μm. The fabricated samples have a relatively large surface area, with a total lateral size of 2.54 $\times$ 2.54 cm^2, in order to enable the accurate characterization of the MMAs at high incident angles.

We characterize the specular absorbance, defined as $A_S(\omega) = 1 - R(\omega)$, where $R(\omega)$ is the reflectance, shown as the blue curve in Fig. 6.1. (The transmittance $T(\omega)$ was zero in all measurements due to the thick continuous gold ground plane.) The reflectance (unpolarized) is collected at near normal incidence (21 degrees) and is normalized by the reflectivity of a gold mirror. We find that the IR MMA obtains a prominent peak with a value of A_S= 99.8% at 6.14 μm. Outside of this main absorptive feature A_S is relatively low and there are small local maxima observed at 6.67, 6.96, 7.10, 7.99, and 9.57 μm due to characteristic absorptions in the dielectric

spacer layer of BCB [108], see Fig. 6.1(c) for detail.

In order to quantify the contribution of diffuse scattering to the specular absorption shown in Fig. 6.1, we characterized the MMA using a sphere integrator [109, 110]. A gold coated Lambertian scatterer is used to obtain the normalized diffuse scattered light (D) and normalized diffuse plus specularly reflected light ($D+R$). Radiation is incident at 13 degrees and measurements are performed at atmospheric conditions. In Fig. 6.1 (b) $D(\omega)$ is plotted as the dashed grey curve and is low and relatively featureless from 4-8.5 μm with values around 2.2-2.3% [111]. As we proceed to wavelengths shorter than 4 μm, D begins to increase and is 64.0% at 2.0μm. Interestingly the increase in D is fairly rapid and continuous for wavelength shorter than 4μm, except for some notable features occurring at 2.32, 2.60, 2.89 and 3.20 μm. Having characterized the diffuse scattering we may plot the total absorbance, (solid red curve of Fig. 6.1(a)), defined as $A_T = 1 - (R(\omega) + D(\omega))$ over the range of 2-8.5 μm. One noticeable feature at 4.24 μm in the total reflectance spectrum is due to the asymmetric stretch mode of CO_2[112]. It should be stressed that the two distinct measurements, A_S and A_T, are in good agreement over the range from 4-8.5 μm, and only largely deviate from each other where the diffuse scattering becomes significant. Figure 6.1(b) shows a detailed view of $D(\omega)$ and it is found that a global minimum ($\sim 1.9\%$) in the diffuse scattering occurs at the exact position of the primary metamaterial absorption, denoted by the dashed vertical line.

Having verified the negligible impact of diffuse scattering on absorption we next investigate the possible existence of surface waves on MMAs and clarify their impact on the electromagnetic properties. We carry out a series of off-normal angle dependent reflectance measurements in both transverse electric (TE) and transverse magnetic

(TM) polarizations. Experimental results for TE (dashed black curves) and TM (solid grey curves) at incident angles of 15, 30, 45, and 60 degrees are plotted as A_S and shown in the left panels of Fig. 6.2. For both polarizations the spectral characteristics of A_S are similar for near normal incidence (15 degrees) – a main absorptive feature due to the MMA is observed near 6μm and other identifiable BCB absorptive signatures are found. Proceeding to larger incident angles we observe that, for the TE polarized case, the amplitude of the main peak drops noticeably from 90% at 15 degrees to 75% at 60 degrees. However, for TM polarization the peak in A_S remains high for all angles investigated, but notably two distinct signatures are revealed for larger incidence angles. One of these absorptive features – which we term here Mode A – is independent of incident angle and occurs at a wavelength of 4.83μm. The other feature – termed Mode B – is observed to shift to longer wavelengths as angle is increased (as noted by the red arrows in Fig. 6.2).

5.3 Simulation

In order to gain insight into the various absorptive features observed in the experimental results presented above, we perform 3D full wave electromagnetic field simulations (CST Microwave Studio 2012). The MMA was simulated with dimensions identical to that of the fabricated sample. We use a Drude model for all metallic components [113], and a frequency independent dielectric constant of $2.06 + i0.12$ for BCB. Unit cell boundary conditions are assigned which enable us to computationally investigate the angular and polarization dependent absorption. Simulations provide the complex scattering parameters and we calculate the specular absorption as $A_S = 1 - R = 1 - |S_{11}|^2$. The right panels of Fig. 6.2 show A_S for various incident

angles and good agreement with experimental results is evident - notably both Modes A and B are also observed.

5.4 Discussion

We next discuss the implications of the experimental and computational results and focus first on Mode B. We note that Mode B only appears in the TM polarization and its peak redshifts as a function of incident angle. It is well-known that periodic structures can support spoof surface-plasmon-polaritons (SPPs) for TM polarization incident waves [69]. Excitation of SPPs requires the momentum of incident light, k_i, to match that of the SPP [1, 19], i.e. $k_{spp} = k_i + k_G$, where k_{spp} and k_G are k-vectors of SPP and the Bloch wave (reciprocal lattice vector), respectively. By re-writing k_i in terms of free space light k_0 as $k_i = k_0 sin\theta$, a strong angular dependence of such SPPs is evident. If Mode B is indeed a SPP, then its peak value should be a function of sin(θ). We perform a linear fit to our experimental data, (not shown) and find that our y-intercept, $k_G = 2\pi/a$, equals a value of 1.71×10^6 (m^{-1}). A linear fit to the curve reveals a value of $a = 3.65$ μm, which agrees qualitatively with the lattice spacing (3.2μm) of the fabricated samples. Thus, we attribute the angular dependent feature, (Mode B), as a Bloch wave or spoof SPP, related to the periodicity of the metamaterial.

The other absorptive feature, (Mode A), however is independent of incident angle, always occurring near 4.83μm. Notably, Mode A seems to increase in strength as a function of increasing incident angle. To note, at 30 degress incidence, both Mode A and Mode B occur at the same wavelenghth, thus increasing the apparent oscillator strength of Mode A. In turn, we computationally investigate its properties with light

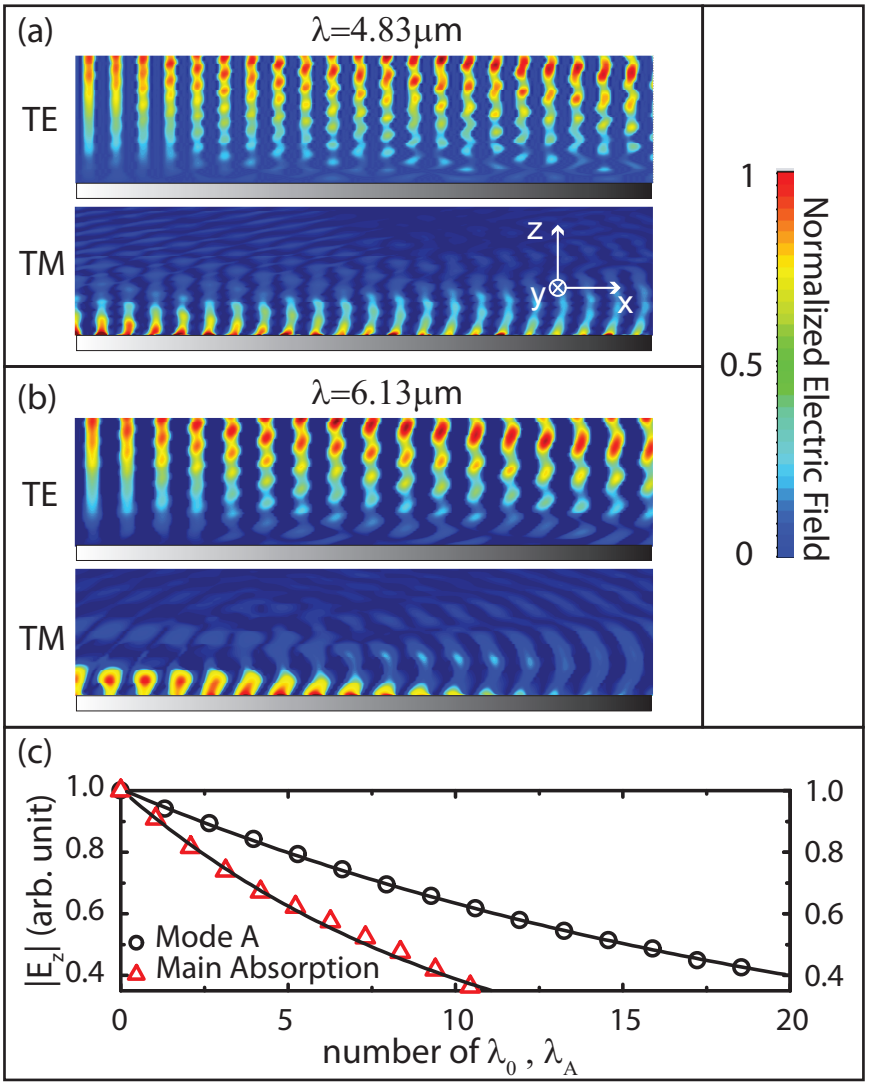

Figure 5.3: Simulated electric field along the surface of the metamaterial absorber at (a) 4.83 μm and (b) 6.14 μm for both TE, and TM polarizations. (c) $|E_z|$ as a function of position in the x-direction at 4.83μm (open triangles) and 6.14 μm (open circles). The horizontal axis is in units of the free space wavelengths of λ_0 and λ_A, where λ_A denotes free space wavelength of Mode A.

coming in at an incident angle of 90 degrees. A computational geometry consisting of 32 MMA unit cells is simulated and has a total length of 102.4μm, (see Fig. 6.3). Along the z direction, an open boundary is assigned to the top of the bounding box while a perfect electric boundary is assigned to the bottom (the metal ground plane). By setting either a perfect electric or perfect magnetic boundary condition in the y direction, incident light along the x direction can be approximated as TE or TM polarization.

The simulated transmission (not shown) shows two noticeable dips in TM polarization but, notably, is featureless for TE polarization, i.e. high transmission over the range investigated. Transverse magnetic polarized transmission minima occur at 6.17μm and 4.80μm, which can be correlated to the primary metamaterial absorption and Mode A in our measurements, respectively. In Fig. 6.3 (a) and (b) we plot the electric field at 6.17μm and 4.80μm for both TM and TE polarizations. We first discuss λ=4.80μm, as plotted in Fig. 6.3(a), which shows a TE polarized wave which does not couple to the surface. However, drastically different behavior is observed for the TM polarized wave. We find that the TM incident wave is coupled to the surface of the metamaterial and both a decaying surface wave and a free space component are observed. The phase advance of the surface wave, compared to that of the free space wave, is different causing interference – a signature of light coupling with surface plasmons. Although quantitatively the TE and TM polarized waves show disparate behavior, our simulations further allow us to extract quantitative information by approximating both the wave number and loss of the SEW. For example, in Fig. 6.3 (a) the wavelength of the TM surface waves λ_A, may be determined by tracing the extrema of the electric field along the air/metamaterial interface. We find that the

SEW yields a wavelength of about 4.72μm while the free space wavelength is 4.83μm. Thus this mode is a type of slow waves with a k-vector 1.02 times larger than that of free space light. In addition, the propagation length (L_{spp}) can be calculated by extracting the z component of the electric field as a function of position (x direction), see open black circles in Fig. 6.3(c). From a decaying exponential fit to the plot we find that L_{spp} is about 102 μm indicating that the SEW travels over an appreciable distance of 25$\times$ its free space wavelength of 4.83μm. Similar behavior is observed for TE and TM polarized waves at $\lambda = 6.13\mu$m, i.e. a SEW in TM polarization. We thus apply the same analysis in order to study the electric field surface profiles, see Fig. 6.3(b). One noticeable difference is the TM polarized SPP at 6.13μm has a propagation length of 64.5 μm, which is only about half of that found for Mode A, shown in Fig. 6.3(c).

We may gain further insight into Modes A and B by performing eigenmode simulations which allow us to calculate the band structure for the k-vector parallel ($k_{\|}$) to the MMA surface – see Fig. 5.4. An acoustic-like branch beginning from zero frequency is found with the slope equal to that of the free space light line. As can be seen, a band gap occurs before which another linearly dispersing mode is observed. In addition, two plasmon-like modes at 6 and 4.7μm can be observed. Although our eigenmode solver ignores losses, it should be stressed that these SPP-like modes occur at frequencies very close to the experimentally determined values of the primary absorption peak and mode A (red and blue dash curves of Fig. 5.4).

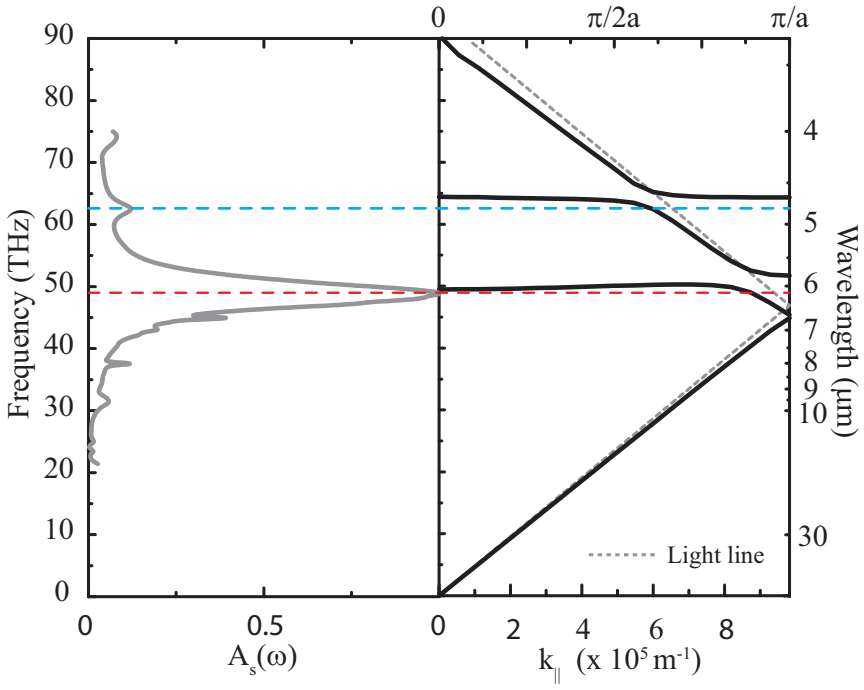

Figure 5.4: Experimental frequency dependent absorption (left panel) and simulated dispersion relation in the $k_{||}$ direction (right panel) for the metamaterial absorber. The two horizontal dash curves indicate the peak positions of mode A (blue) and the primary metamaterial absorptive resonance (red).

5.5 Conclusion

We computationally and experimentally investigated scattering and generation of surface electromagnetic waves on infrared metamaterial absorbers. Scattering was found to be negligible near the primary metamaterial absorption λ_0, and only became appreciable at shorter wavelengths. Two surface modes were found to exist on metamaterial absorbers, when incident light is TM polarized, one due to the periodicity of the unit cell and the other due to the effective optical constants of the MMA. The latter occurs at λ_0, is highly lossy and is responsible for the good angular dependence of absorption in TM polarization.

Chapter 6

A Sub-wavelength Extraordinary-optical-transmission Channel in Babinet Metamaterials

6.1 Introduction

The study of light coupling to small apertures in metallic films has a long and illustrious history. In 1897 Lord Rayleigh treated the problem by using the concept of effective dipoles. Most recently, researchers have made these apertures periodic, where they exhibited so-called extraordinary optical transmission (EOT) - transmission efficiencies far in excess of unity at wavelengths greater than the lattice parameter of the surface. This behavior is not predicted by standard aperture theory as developed by Bethe in 1944, [114] nor was it noticed before fabricational and measurement techniques had advanced to the point that EOT could be observed at optical wavelengths. However, in 1998 Ebbesen *et al.* [115] showed EOT in the near-infrared and posited that this stemmed from plasmon coupling between surfaces. Since then, EOT [115, 116, 117, 118] has been studied with increasing detail in both theoretical

and experimental capacities. This result led to a flurry of intense theoretical and experimental research to probe the nature of this extraordinary optical transmission.

Babinet metamaterials [75, 48, 119] may also be described as periodic apertures in metal films. Metamaterials are structured periodic metallic patterns which enable the construction of materials with specified electromagnetic properties, some of which cannot be obtained *via* naturally occurring materials. [120, 102] Metamaterials exhibit electromagnetic resonances where the resonant wavelength is significantly larger than the physical dimensions of the individual elements. Thus metamaterials are subwavelength media and well described by the optical constants ϵ and μ. [36] In transmission metamaterials (scatterers) yield an absorptive like minimum feature at resonance, but are otherwise highly transmissive outside of this band. In contrast Babinet metamaterials (apertures) - made by taking the "inverse" metamaterial structure - yield opposite behavior and exhibit a transmission maxima near resonance. [121, 122]

Here we describe both Babinet metamaterials and EOT by an effective medium theory with plasmons playing a particularly important role. We further show that by utilizing metamaterial shaped apertures, we can further augment the EOT effect. Specifically, it is demonstrated that Babinet metamaterials exhibit higher transmission efficiencies at lower frequencies than traditional ellipsoidal and quadrilateral hole designs.

6.2 Theoretical Model of Babinet Metamateirals

Light transmission through patterned metallic surfaces display more complicated scattering, (compared to transmission in bulk metals), which is not easily reconciled with

Drude theory. Specifically, drilled holes in metals exhibit transmission maxima far below the plasma frequencies of metals, even considering the finite hole size by accounting for diffraction. Most research has focused on holes of simple geometry to provide analytical models of the plasmon dispersion, and good progress has been made to accurately describe the transmission properties and clarify the contribution from surface modes. [123, 124, 125, 126] Although there has been some experimental investigation of the effects of perturbations to the geometry, no consistent theoretical model predicts the effect of aperture shape on the transmission spectra. Additionally, EOT has been shown to extend to frequencies far lower than the optical where surface structure can mimic a plasmonic response.

The theoretical consensus for enhanced transmission is that it is the result of excited surface plasmon polaritons (SPPs) which couple on either side of the metal. [116] However, the enhanced transmission phenomenon can be scaled to much lower frequencies, at which metals act essentially as perfect electric conductors. Prior experimental works have observed abnormal transmission in conductive periodic apertures, known as frequency-selective surfaces, in the microwave and infrared ranges. [127, 128, 129]However, at the time these studies were not directly linked to EOT since there was no known SPP coupling mechanism. Based on the theoretical framework developed by Pendry [69] and Garcia-Vidal *et al.*, [130], the SPP-like behavior is "spoofed" by the excitation of waveguide modes in the holes, and the plasma frequency is given by the cutoff of the permitted lowest-order waveguide mode. [69] Within the proposed model, we see that there is a method to further modify the dispersion of the surface. A surface perforated by small square holes yields a plasmon-like dispersion curve similar to a Drude metal, but determined by the geometry of the

waveguide. It was shown that propagating modes exist for frequencies such that $\epsilon_h > \frac{\pi^2 c^2}{l^2 \omega^2}$ where ϵ_h is the dielectric constant of materials filling the holes, l is the side length of the hole, and c is the speed of light. By tuning ϵ_h we may thus significantly alter the dispersion of the artificial plasmon.

We demonstrate that the geometry of the hole or aperture can profoundly impact dispersion and we use a class of structures known as complementary metamaterials (CMMs) - also called Babinet metamaterials. Falcone *et al.* [48] demonstrated through Babinet's principle that a complementary split-ring resonator (CSRR) could be considered to have an effective electric response. It was then noted by Liu *et al.* [123] that the CSRR could be treated as an electric metamaterial, in the context of a waveguide, and validated this by retrieval of the optical constants. [22, 23] Other work interpreted complimentary electric ring resonators by an effective permeability response, based on the electromagnetic duality of Maxwell's equations. [131]

6.3 Simulation

In order to elucidate the physics underlying EOT, we perform computer simulations using a commercially available finite difference time domain solver for three different aperture structures. All geometries were substrate-free and the conductive portions were modeled as gold using the Drude model with a complex frequency dependent conductivity, a plasma frequency ω_p=2$\pi\times$2175 THz, and collision frequency ω_{col}=2$\pi\times$6.5 THz. Incident light is polarized along the x axis and the effective permittivity ($\epsilon(\omega) = \epsilon_1(\omega) + i\epsilon_2(\omega)$) is obtained by inversion of the S-parameter data, where we use a thickness of t=200nm (see Supporting Information for simulation details). It should be noted that the effective medium approach applied here can only offer a good

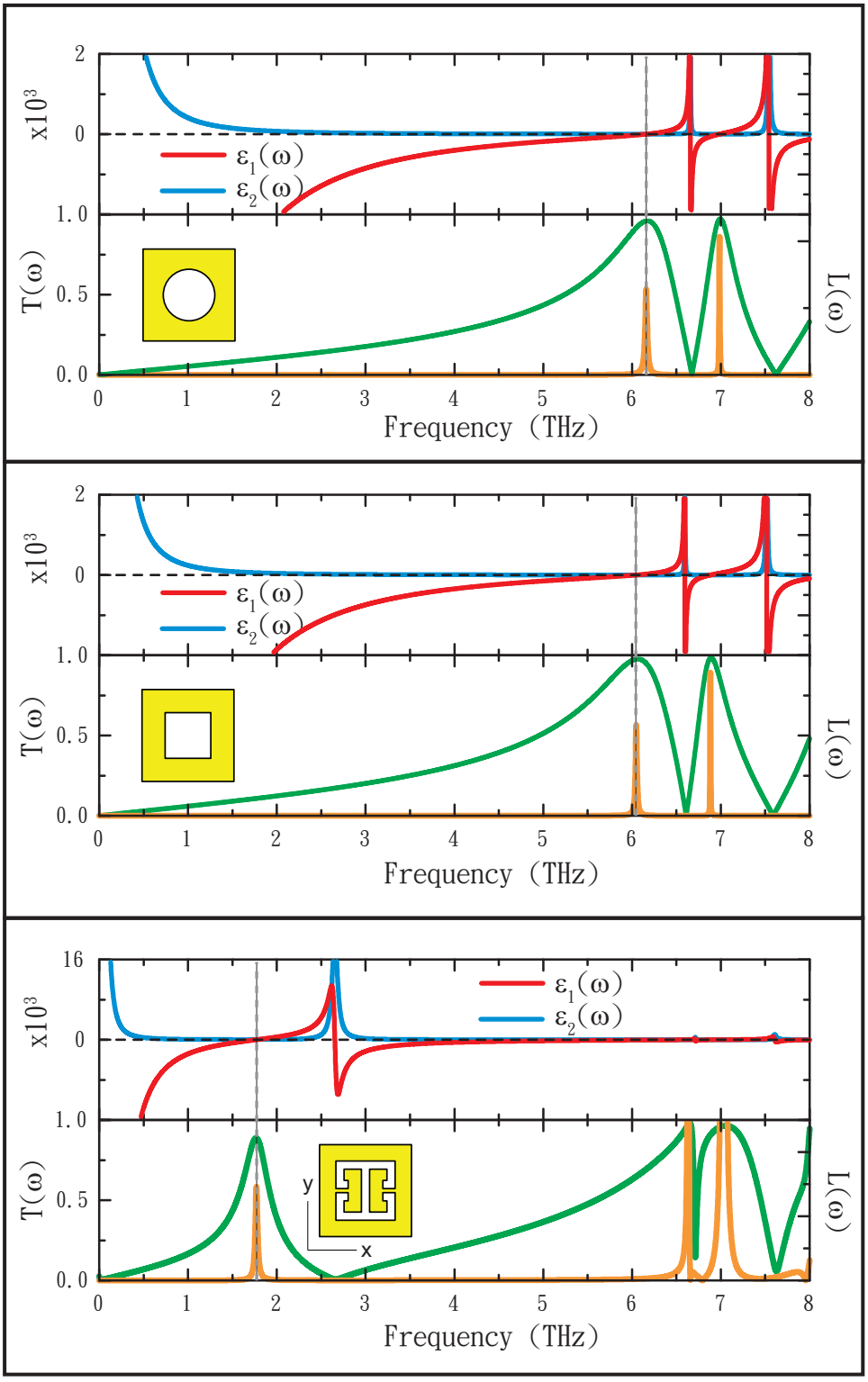

Figure 6.1: The retrieved real and imaginary permittivity, $\epsilon_1(\omega)$ (red curves) and $\epsilon_2(\omega)$ (blue curves), simulated transmission spectra $T(\omega)$(green curves - scale on the left axis), and Loss function $L(\omega)$ (gold curves - scale on the right axis) of the periodic aperture media. Each aperture has an area $A = 500\ \mu m^2$.

approximation, but not an exact solution. The analysis is generally valid when the feature size of the metamaterial is small compared to the wavelength, but produces considerable errors when spatial dispersion is non-negligible. Fortunately in all cases considered here, the transmission modes are outside of polarization resonances, (see the retrieved permittivity in Fig. 1). Our approach is accurate since, at frequencies of interest, $\epsilon(\omega)$ vanishes and we are in the deeply subwavelength regime.[38] In the top, middle, and bottom panels of Fig. 6.1 we present simulated results for circular, square, and Babinet metamaterial apertures, respectively. (Schematics of each aperture are also shown in the insets.) For the purposes of this study we have made both the area of the aperture (A=500μm^2) and the lattice parameter (a=45μm) equal for each unit cell. In Fig. 6.1 the extracted dielectric function ($\epsilon_1(\omega)$ and $\epsilon_2(\omega)$), the transmission ($T(\omega)$), and so-called loss function $L(\omega) \equiv -Im[1/\epsilon(\omega)]$ are shown as the red, blue, green (left axis), and gold curves (right axis), respectively. The circular aperture exhibits a transmission maximum (T_m) at ω_c=2$\pi\times$6.17 THz, the square aperture at ω_s=2$\pi\times$6.06 THz, and the Babinet metamaterial at ω_b=2$\pi\times$1.77 THz. As can be observed for all apertures, ϵ_1 (red curve) is negative at low frequencies and increases as a function of frequency with a Drude-like dependence. As ϵ_1 approaches zero (dashed black horizontal lines) the transmission increases and T=T_m near ϵ=0 for each. This dependency of T on the dielectric function is a simple consequence of our effective medium approach and a thin-film calculation. [132]

By comparing the transmission to the dielectric function we may associate the transmission minimum to a Lorentz-type resonant absorption evident in ϵ for all apertures. We note that the peak of $L(\omega)$, which represents the frequency of longitudinal optical modes for natural materials, can be seen to occur precisely at the

same frequencies where the transmission is maximum, see dashed grey vertical lines of each case in Fig. 6.1. Across the frequency range investigated each structure exhibits another transmission minimum and maximum, however here we only analyze the first transmission maximum.

The nature of the transmission bands described above can be computationally explored via the dispersion relations. We utilize a commercially available electromagnetic wave eigensolver to numerically calculate the k-vector perpendicular ($k_\perp$) and parallel ($k_\parallel$) to the aperture surface for each geometry as shown in the left and right panels of Fig. 6.2 (a). For propagation along the $k_\perp$ direction, all branches are optical-like modes and two occur near 6.7 and 7.3THz for all cases investigated. Distinct from circular and square apertures, the Babinet metamaterial realizes an additional mode occurring at a frequency near 1.8 THz. The right panels of Fig. 6.2 (a) show the $k_\parallel$ dispersion and we find an acoustic-like branch for all apertures beginning from zero frequency. The group velocity of this mode is approximately equal to that of the free space light line - as determined by the slope (not shown). As the curve approaches the Brillioun zone boundary, set by the periodicity, the group velocity reduces drastically; a characteristic of slow-wave modes. As we continue to higher frequencies, there is a band gap before which another linearly dispersing mode is observed - again with a velocity close to that of the light line (reminiscent of the band folding in periodic zone scheme). In addition to the above described common features of all apertures studied for $k_\parallel$ dispersion, there exists an unique propagating mode for the metamaterial geometry - a dispersion-less feature found at 1.8 THz (red dash curve of Fig. 6.2 (a)). This curve has a group velocity about 10-20 times slower than the speed of light - see Fig. 6.2 (b). Notably, all optical-like modes occur near

individual transmission maxima. For example, in the case of the Babinet metamaterial, the red and blue curves of the Fig. 6.2 are modes associated to the three transmission bands centered at 1.8, 6.5 and 7 THz, respectively.

Remarkably, the simulated dispersion relations presented above demonstrates that every transmission band not only corresponds to a specific optical branch along the $k_\perp$ direction, but also to a slow wave mode along $k_\parallel$; see the dash curves to the right panels of Fig. 6.2 (a). These are longitudinal bulk plasma modes in the perforated metallic film. Our model, based on the correlation between normal and complementary structures, yields a Drude-like effective dielectric function for the aperture films of,

$$\epsilon_c(\omega) \approx \frac{4c^2}{d^2\omega_i^2}(1 - \frac{\omega_0^2}{\omega^2}) \tag{6.1}$$

where d is the film thickness, ω_i and ω_0 are the effective plasma frequencies of the scatterer and hole arrays, respectively. A longitudinal mode exists in the film for $\epsilon_c(\omega) = 0$, which from Eq. 6.1 yields $\omega = \omega_0$, i.e. a dispersionless mode in all k-space directions. Our model permits an estimation of the transmission maxima and effective plasma frequency of the aperture film by analytically solving for the central resonant frequency ω_0 of the original metamaterial (the scatterer) – easily calculable based on the metamaterial geometry. [100, 97] As proof of principle, we can approximate the spectral location of the transmission maximum of the Babinet metamaterials by using the geometry (circumference) of the complementary features of the perforations. This qualitatively explains all of the main features observed, including $\omega_0 \ll \omega_p$, and the much lower ω_0 for the Babinet metamaterial structure as compared with that for simple shapes (e.g. circle and square). For more details see Supporting information.

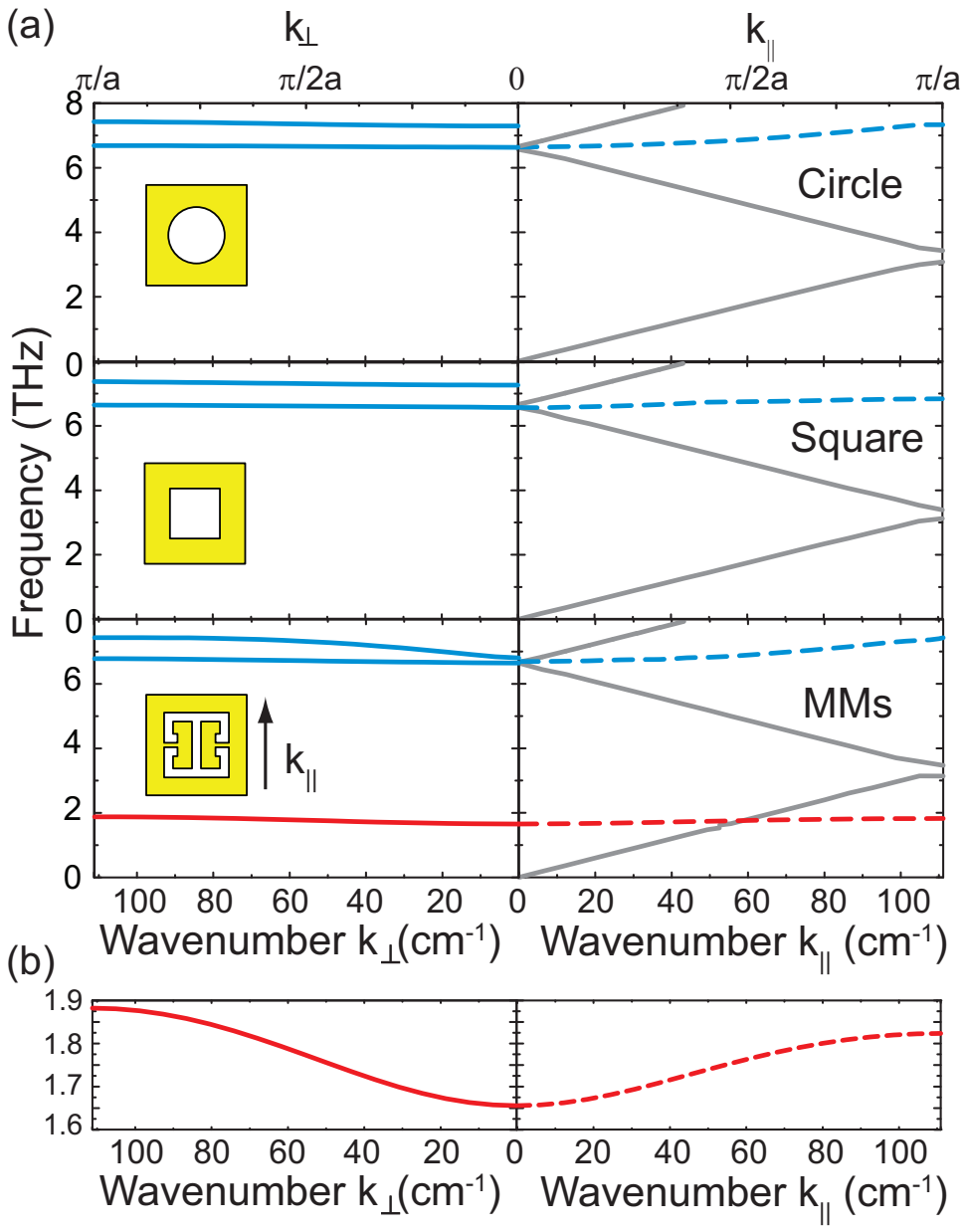

Figure 6.2: (a) Simulated dispersion curves for two different k directions of the periodic apertures studied here. Each optical branch in $k_\perp$ (solid curves in the left panels) can be linked with the transmission maxima observed in the spectra of the individual apertures (blue curves of Fig. 1). Solid grey curves (right panels) are acoustic modes that disperse similarly to the free space light line for low frequencies. Dash curves (right panels) are SPP-like modes. Metamaterial apertures realize an additional transmission channel (red curves) at much lower frequencies. (b) A zoomed-in view of the lowest mode for the metamaterial aperture.

Our results on conventional apertures are consistent with prior work [133], and indicate that the transmission mode of the circle and square geometries occurs close to the diffractive order of the structure, known as Wood's anomaly [133]. As mentioned previously, the low frequency metamaterial aperture mode occurs at frequencies far below the first diffractive order which, to the best of our knowledge, has not been observed elsewhere. This low frequency plasmon occurs in the first Brillouin zone and is not related to band-folding (Umklapp). Other work on conventional EOT has demonstrated that geometric tuning, i.e. changing the aspect ratio of rectangular [134] or circular holes [135, 136, 137, 138], can effectively red-shift the transmission peak which leads to various degrees of hybridization between the in-plane vertical and horizontal SPP modes. However, the shift in frequency is small and the spectral location of $T(\omega)$ is not distinct from the Bloch mode. In the case of the Babinet metamaterial aperture the low frequency transmission band cannot be explained by the same coupling mechanism. Our results indicate that a new class of modes (bulk plasmons associated with vanishing of the effective dielectric function of the perforated metallic film), controlled by the geometry of the Babinet metamaterial, remains unexplored. In Table I we summarize the different types of EOT structures and specify the frequency and wavevector regimes they operate in. Type I is the conventional EOT observed in small metallic holes occurring at frequencies close to ω_p. Type II are hole arrays where the hole diameter and lattice parameter are all of order of the resonant wavelength (λ_0). Type III are more complex shaped "hole" arrays, where $a \ll \lambda_0$. Case I is restricted to the near infrared and optical range of the electromagnetic spectrum, since plasma frequencies for metals typically occur in the optical and ultraviolet. However both Case II and III are engineered EOT structures and thus do

not suffer the limitations of Case I. However, Case III yields the highest transmission efficiencies and is more sub-wavelength than Case II structures.

Type	periodicity	ω_0	λ_0	k-vector	SPP-like
I	no	$\sim \omega_p$	–	–	Normal
II	a	$\sim \omega_a$	$\sim a$	$\sim \frac{2\pi}{a}$	Spoof
III	a	$\ll \omega_a$	$\gg a$	$< \frac{2\pi}{a}$	Geom.

Table 6.1: Comparison of various types of EOT responses, where ω_0 and $\lambda_0 = 2\pi c/\omega_0$ are the central frequency and wavelength of EOT, c is the speed of light, a is the lattice constant of the hole array, $\omega_a = 2\pi c/a$ is the frequency related to the periodicity, and Geom. is short for geometric.

6.4 Experimental Characterization

Experiments were performed to verify this unique predicted property of Babinet metamaterials. The circle, square, and metamaterial samples were fabricated with the same dimensions as simulated, see the insets of Fig. 6.3. Although it is not feasible to fabricate substrate free large area thin metallic films, it is straight forward to produce free standing optically-thin polymer substrates [50] which can support apertures studied here, (see Supporting Information for fabrication and experimental procedure details). Experimental results for the circle, square, and metamaterial apertures are shown in Fig. 6.3 (a), (b), and (c), respectively. The maximum of each transmission band is lower than that predicted by simulation and all resonances are redshifted by approximately 25%, (see Fig. 6.1 and 6.3). Regardless of these deviations, (both due to the polyamide substrate), all general spectral features are preserved. Specifically a transmission band at 1.3THz is found for the Babinet metamaterial aperture which is not observed for the other two apertures, which have their first transmission peaks

near 5THz.

All apertures were simulated with an additional 4μm-thick polyimide supporting substrate ($\epsilon_r = 2.88 + i0.23$). In Fig. 6.3 (a) we plot the simulated $T(\omega)$ as the solid black (circle), blue (square), and red (metamaterial) curves. We find good agreement between simulation and experiment and perform extraction to obtain the effective permittivity $\epsilon_1(\omega)$ and loss function of all apertures $L(\omega)$ – see Fig. 6.3 (d) and (e).

6.5 Discussion

We now turn toward discussion of the apertures as effective dielectric media. One approach for calculating $\epsilon(\omega)$ is to correlate the electromagnetic response with its complementary element through Babinet's principle [139, 34, 140], which describes scattering of the pair (aperture and scatterer) based on electromagnetic duality. [75, 131] Although these symmetry requirements provide no obstacle for describing the aperture in terms of effective electric dipole radiation, they lose validity when interpreted as effective magnetic media [131] – see Supporting Information for details. This can be easily shown as any in-plane magnetic field $\overline{B}$ cannot affect the electron's motion in a strictly 2D confinement. Thus, at normal incidence this allows for a complete effective medium description of the scattering, as shown by retrieval of the effective permittivity Fig. 6.1.

6.6 Conclusion

In conclusion, we have analyzed the transmissive properties of Babinet metamaterials through an effective medium description and demonstrated unambiguously that the EOT effect is a result of light coupling with SPP-like and bulk plasmon modes. A

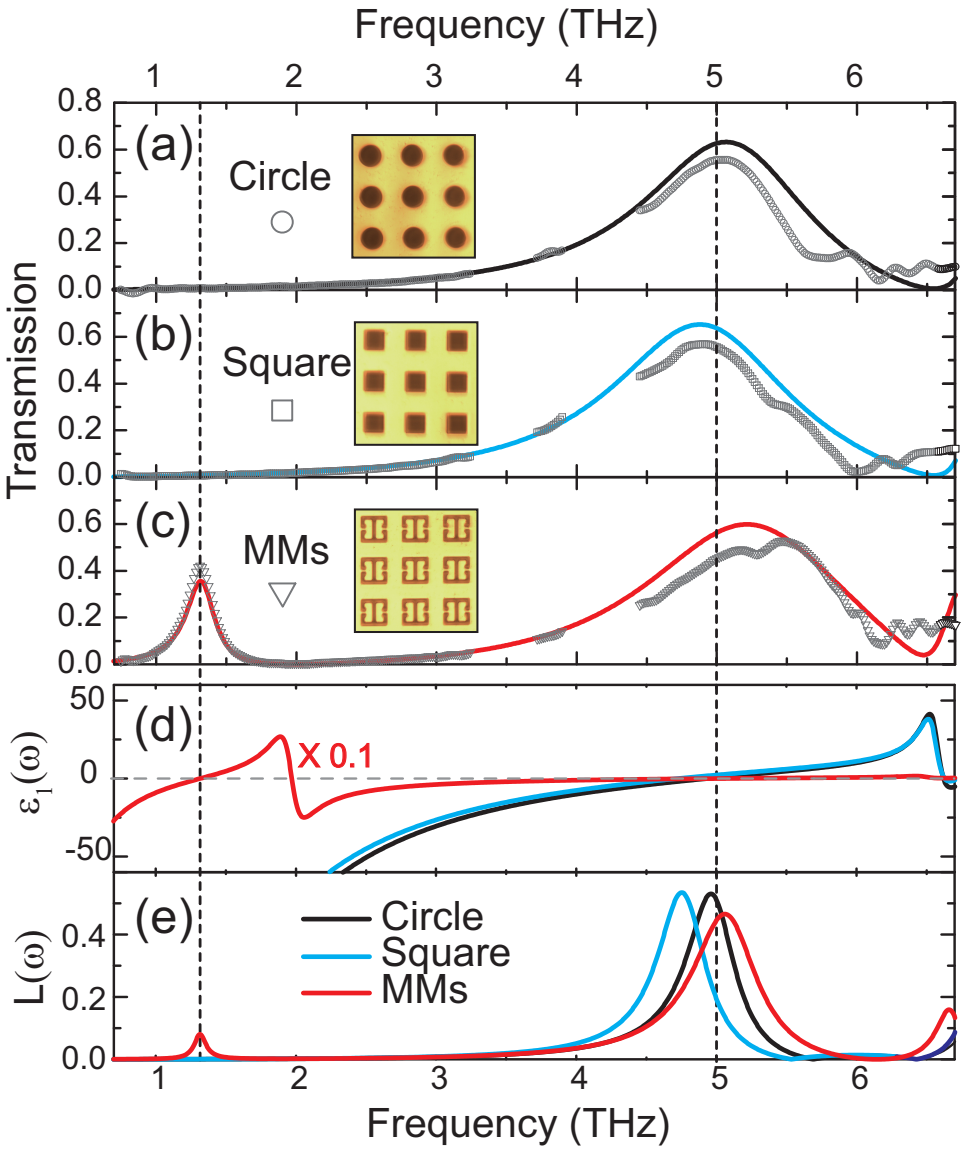

Figure 6.3: Transmission of (a) circle, (b) square, and (c) metamaterial apertures; symbols are the experimental data, and solid curves are simulated data. The insets are microscope images of the fabricated samples with a lattice constant $a = 45\mu$m. (d) Real part of dielectric function $\epsilon_1(\omega)$ and (e) loss function $L(\omega)$ of the MM structures.

non-dispersive feature along both $k_{\perp}$ and $k_{||}$ directions verifies that bulk and surface plasma frequencies are identical at the zone center, i.e. $\omega_{spp} = \omega_p$ – in stark contrast to a normal metallic film where $\omega_{spp} = \omega_p/\sqrt{2}$. We further computationally and experimentally investigated a novel transmission band which exists only for Babinet metamaterials that is not related to Wood's anomaly. This sub-wavelength transmission mode is a geometrical effect and allows Babinet metamaterials to achieve higher transmission efficiency than conventional EOT apertures. It was demonstrated that Babinet metamaterials must be interpreted as effective electric media at normal incidence. Analytical methods applied to metamaterials used to calculate the effective scattering properties may now be applied to EOT apertures - specifically to calculate transmission bands. Analytical methods applied to metamaterials used to calculate the effective scattering properties may now be applied to EOT apertures [100, 97]-specifically to calculate transmission bands. Metamaterials demonstrated here provide an additional parameter for designing more efficient aperture structures based on the EOT effect which may be useful for filters, polarizers and surfaces for sensing applications.

Chapter 7

Summary and Conclusions

Metamaterial's ability of tailoring electromagnetic waves making them great candidates for novel device applications. In this dissertation, we further demonstrate such advantages of MMs can also apply to the plasmonic devices. On the other hand, MMs system might support surface electromagnetic energy in an undesired way that interferes with the original process. This is because most of MMs utilize resonant responses leading that the value of the effective optical constants can change suddenly from positive to negative by the operation frequency - conditions of generation of surface waves might be satisfied. It is, thus, important to understand their contribution even at the frequency lower than the plasma frequency of the metal. Two followup works are briefly introduced, where we take advantages of the surface wave channel to further optimize the metamaterial performance.

7.1 Ring Metamaterial Perfect Absorbers

In chapter 5, we revisited a scenario where the canonical MM design absorbs more transverse-magnetic (TM) polarized light in a wide angle than the transverse-electric (TE). The origin is due to generation of SPP waves only occur for the TM case based

on our theoretically and experimentally investigation. Based on the same concept, if one can generate surface plasmons for the other polarization, angular absorbance for TM cases is expected to increase. It is well known that TE-polarized light can interact with two-dimensional split ring resonator arrays and generate so-called "magnetic" plasmons [141]. To test the idea, we use a standard tri-layer metal-dielectric-metal design. First layer is a ring shape resonator, next is a dielectric spacer, and the last is followed by a continue metallic ground plane. The thickness of the dielectric spacing is optimized such that the absorption for the normal Incident light is almost 100%. A preliminary simulated results indicate that the absorption of TE polarized light are increased noticeably (black curves in the bottom panel of Fig. 7.2)when compared to that of the cross MMA (grey curves). However, the absorption for TM polarization seems to be suppressed, as can be seen in the top panel of Fig. 7.2. Further investigation is required to understand this interesting phenomenon.

7.2 Angular Insensitive Transmission Mode in Complementary Metamaterial Apertures

In Chapter 6, we investigated complementary metamaterial structures using effective medium approach and obtain several new insights [142]. Firstly, the spectral responses of the CMMs are in full analogy to the extraordinary optical transmission (EOT) as the abnormally huge transmission of these 'tiny' holes always occurs at the effective plasma frequency [142]. Secondly, numerical dispersion investigation suggests that the hole media hold an identical effective bulk and surface plasmon frequency. To understand these distinct properties, we propose a full effective medium description of the hole media by treating the resonant charge carriers as electron holes rather than

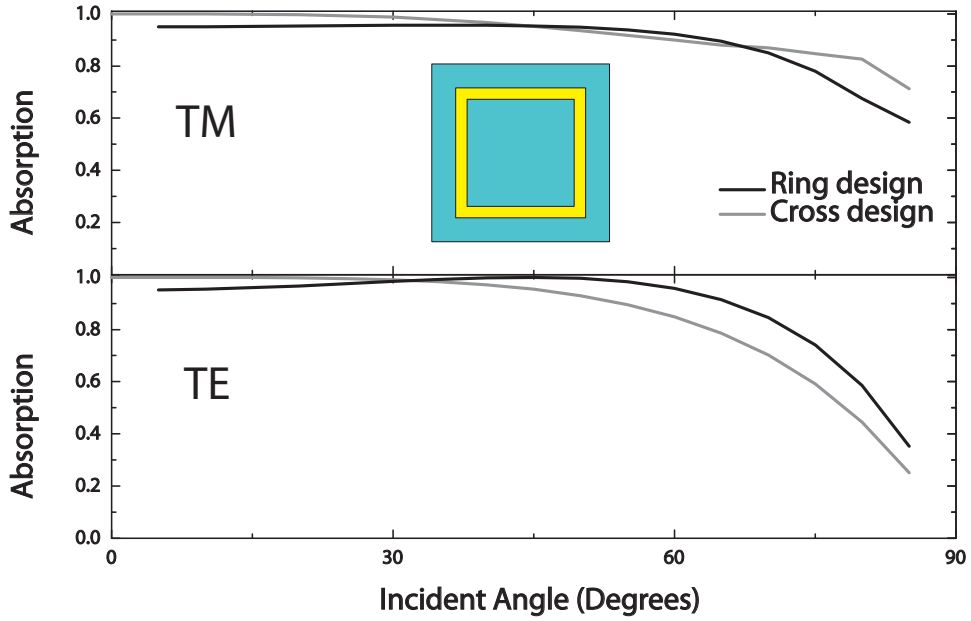

Figure 7.1: Absorption as a function of incident angle for both transverse magnetic (TM) and transverse electric (TE) polarization of the ring and cross metamaterial absorbers. The inset shows the schematic drawing of a ring shape resonator.

electrons of the regular MMs. This ad hoc approach will be confirmed analytically, and compared with the numerical homogenization process.

Let us briefly summarize properties of the Babinet metamaterial apertures in Chapter 6. Complementary electric split ring resonators (CERRs) were studied using three dimensional electromagnetic wave simulators. A schematic drawing of the CERR is shown in Fig. 7.3 (a). The thickness of the metal is 200nm, and all other geometric parameters are: $b = 6\mu$m, $c = 30\mu$m, $g = 2\mu$m, and $w = 4\mu$m. The lattice constant (a) of the structure is 45 μm. Simulated spectrum of the CERR is shown in Fig. 7.3 (b). Similar to the conventional EOT responses, we observe a transmission maximum occurring by Wood's anomaly, $\lambda \sim a$, at 6.7 THz, whereas the fundamental mode appears at a much lower frequency of 1.8 THz [133]. The simulated dispersion

relations along $k_\perp$ and $k_{||}$ indicate that each transmission band corresponds to a dispersless mode in either direction (solid curves along $k_\perp$ and dashed curves along $k_{||}$) - dispersing like bulk and surface plasmons, respectively. For the cases when both $k_\perp$ and $k_{||}$ go to zero, these two branches coincide with each other at the same frequency, an implication of the degeneracy in their bulk and surface plasmon modes, see Chapter 6 for details.

Given that the resonant mechanism is similar for both metamaterials (MMs) and their Babinet compliments - the same charge carriers, i.e. electrons, and the same driving force, i.e. Lorentz force, we argue that the dielectric function of Babinet structures should have an identical generic form as those of regular MMs. Based on the theoretical framework of Pendry et al. [10], MMs can be described as a Lorentzian model as

$$\epsilon(\omega) = \epsilon_\infty + \frac{\omega_{pF}^2}{\omega_0^2 - \omega^2 - i\gamma\omega} \tag{7.1}$$

where ϵ_∞ is a constant associated with dielectric properties at high frequencies, ω_0 is the center frequency of the resonance, γ is the loss factor, and ω_{pF} is the effective plasma frequency. ω_{pF} can be expressed explicitly as $\sqrt{Fn^*e^2/\epsilon_0 m^*} = \sqrt{F}\omega_p$ - a similar analytical form as the plasma frequency of the metals, ω_p, but with additional dependence on the filling fraction of metals, F, (where n^* is the effective electron density, e is electron charge, and m^* is the effective electron mass). Because a Babinet metamaterial is the 'negative' of the conventional design, the filling fraction of metal is $1 - F$ instead. $\epsilon_c(\omega)$ of Babinet metamaterials can then be rewritten as

$$\epsilon_c(\omega) = \epsilon_\infty + \frac{\omega_p^2}{\omega_0^2 - \omega^2 - i\gamma\omega} - \frac{\omega_{pF}^2}{\omega_0^2 - \omega^2 - i\gamma\omega} \tag{7.2}$$

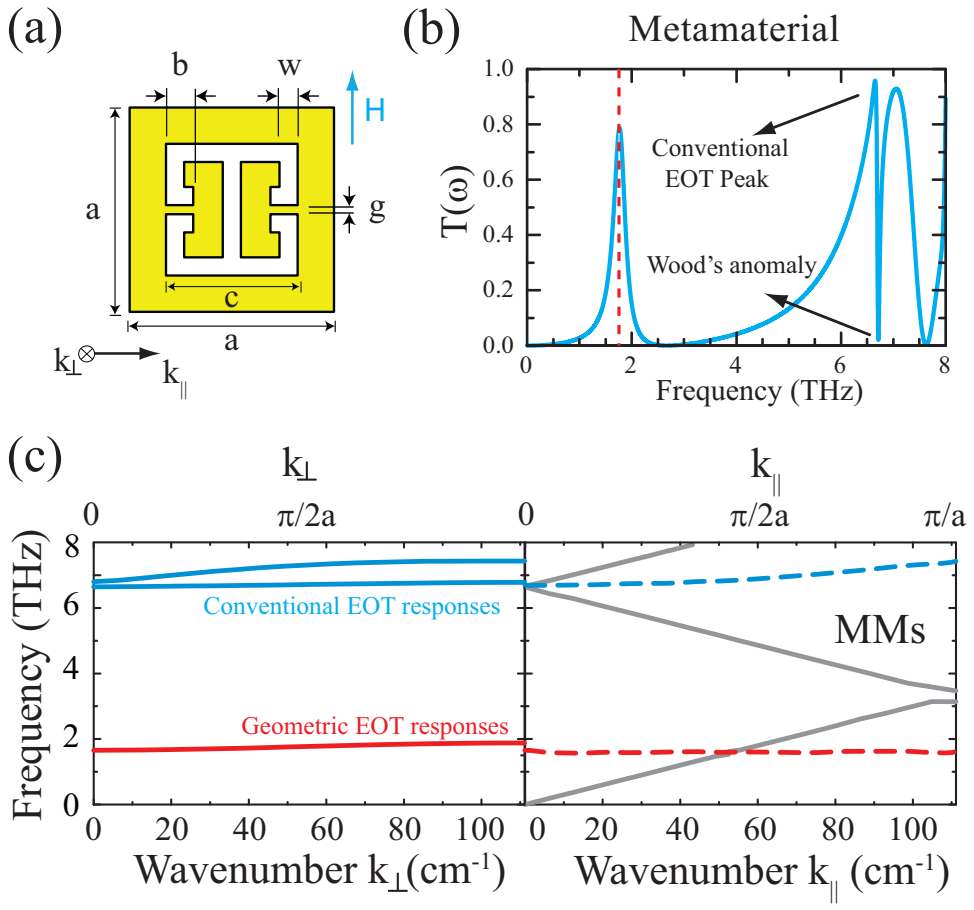

Figure 7.2: (a) A schematic drawing of a complementary electric split ring resonator (CERR) with its geometric parameters: $b = 6\mu$m, $c = 30\mu$m, $g = 2\mu$m, and $w = 4\mu$m. (b) Simulated transmission of the metamaterial apertures. (c) Dispersion relations perpendicular($k_\perp$) and parallel ($k_\perp$) to the CERR's surface.

where we introduce the subscript c to denote the properties of the complementary structures. As can be seen, the second term in Eq. 7.2 contains no filling fraction of F in the numerator and seems to account for the response of the continuous metal. If this is indeed the case, the remaining term has to compensate the change in the charge polarity to keep the open area neutral. Analogous to electron-hole pairs in Solid State Physics, we can consider the open areas are 'hole' carriers possessing positive charges, termed as "meta-holes". By this postulate, the middle and rightmost terms describe dielectric responses for two types of charge carriers, and hence the central resonance/the loss factor is different from each other. The restoring force of an unstructured metal is zero, and thus ω_0 of the middle term is taken to be zero. A diagrammatic expression to illustrate this transformation is shown in Fig. 7.4 (a). We then model the effective mass of the meta-holes as a negative quantity and substitute m^* with $-m^*$ into the rightmost term of Eq. 7.2. Remarkably, after applying all aforementioned conditions, the dielectric function of CMMs resembles a combination of Drude and Lorentzian terms as it can always be expressed as

$$\epsilon_c(\omega) = \epsilon_L(\omega) + \epsilon_D(\omega) \tag{7.3}$$

This ad hoc formula is supported by the following direct derivation. Based on Babinet's principle, a scatterer and its Babinet compliment hold a complementary spectral response, i.e. $T + T_c = 1$ [34]. When the thickness of a dielectric thin film, d, is known [132], its transmittance is only a function of the permittivity, $\epsilon(\omega)$. The complementary transmission relation directly bridges the dielectric functions of the Babinet pair [121, 122].

$$[\epsilon(\omega)-1][\epsilon_c(\omega)-1] = -\left[\frac{2c}{\omega d}\right]^2. \tag{7.4}$$

Note, the negative sign is chosen to satisfy causality since all composites are passive. Given that normal MMs are Lorentzian oscillators, $\epsilon_c(\omega)$ can be obtained analytically by substituting Eq. 7.1 into Eq. 7.4. We get

$$\epsilon_c(\omega) = 1 - \frac{\omega_{pc1}^2}{\omega^2} + \frac{\omega_{pc2}^2}{\omega_{0c}^2 - \omega^2} \tag{7.5}$$

where

$$\begin{aligned}
\omega_{pc1}^2 &= \frac{\omega_0^2\omega_d^2}{\omega_0^2(\epsilon_\infty - 1) - \omega_p^2} \\
\omega_{pc2}^2 &= \frac{\omega_d^2}{\epsilon_\infty - 1}\{1 - \frac{(\epsilon_\infty - 1)\omega_0^2}{(\epsilon_\infty - 1)\omega_0^2 + \omega_p^2}\} \\
\omega_{0c}^2 &= \omega_0^2 + \frac{\omega_p^2}{\epsilon_\infty - 1}
\end{aligned}$$

Identical to our ad hoc model, Eq. 7.5 shows that the Babinet complementary structures contain, in addition to the Lorentzian term (3rd term), also the Drude component (2nd term). The presence of the Drude term reflects simply the metallic nature of the complementary structure and all analysis concurs with our previous assumption.

We compare the result with the effective optical parameters retrieved from the scattering properties of the Babinet MMs [23]. Although the retrieval method fails quickly when $\lambda \sim a$ [38], it is applicable for the CMM case when operated in the deeply subwavelength limit. The resultant curves are shown in Fig. 7.3 (b). We found a Lorentzian-like lineshape at the frequency of 2.64 THz, albeit the extracted

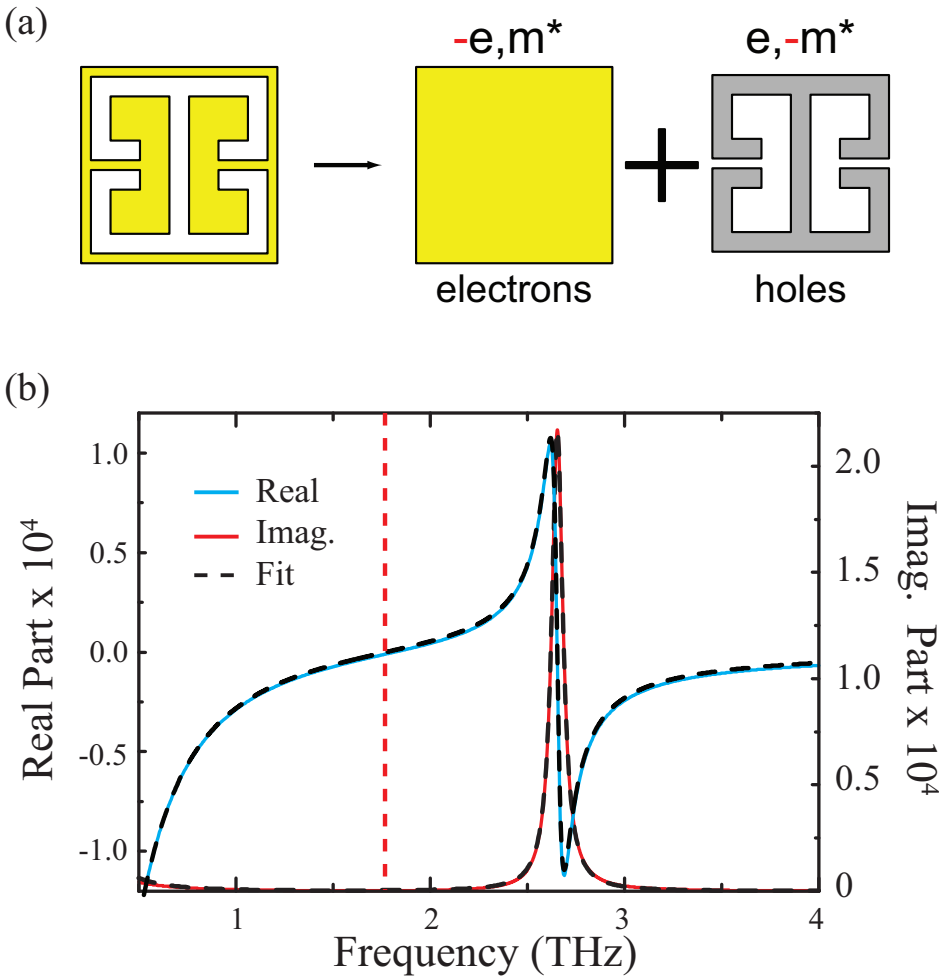

Figure 7.3: (a) A complementary structure can be treated as meta-holes resonating on a continues metal. (b) The real (blue curves) and imaginary parts (red curves) of the extracted permittivity of CERRs shown in Fig. 6.1. The vertical dashed line indicates that the transmission maximum occurs at the zero of the dielectric function.

dielectric function does not have a constant background as those of regular Lorentzian oscillators. We fit the data with the Drude-Lorentzian model using the following parameters: $\omega_{pc1} = 2\pi \times 59.61$ (THz), $\omega_{pc2} = 2\pi \times 63.56$ (THz), $\gamma_1 = 2\pi \times 0.022$ (THz), and $\gamma_2 = 2\pi \times 0.070$ (THz), and found excellent agreement, see dashed curves of Fig. 7.3 (b).

Having verified the effectiveness of the Drude-Lorentzian fit, we employ our model to analyze how CMMs disperse along the $k_{||}$ and $k_{\perp}$ direction. By summing up the last two terms in Eq. 7.5, $\epsilon_c(\omega)$ can be simplified as

$$\epsilon_c(\omega) = \epsilon_\infty + \frac{4c^2}{d^2\omega_p^2}\left(1 - \frac{\omega_0^2}{\omega^2}\right) \approx \frac{4c^2}{d^2\omega_p^2}\left(1 - \frac{\omega_0^2}{\omega^2}\right) \tag{7.6}$$

Since the structure film is operated in the subwavelength region $d^2\omega_p^2 \ll 1$. Eq. 7.6 represents a net Drude response at lower frequencies, and the transparency is mediated by *longitudinal bulk plasmons* at $\omega_b = \omega_0$. This is evident as the transmission maximum (denoted by red dashed curves) peaks at the zero of dielectric function, see Fig. 7.3 (b). On the other hand, the effective dielectric function given by Eq. 7.6 can support a surface plasmon. By assuming there is negligible interaction between either side of MM surface, a SPP dispersion can be described by [2],

$$k_{||} = \frac{\omega}{c}\sqrt{\frac{\epsilon_c}{\epsilon_c + 1}}. \tag{7.7}$$

In the limit of $k_{||} \to \infty$, we find,

$$\omega_{sp} \to \omega_0 = \omega_b. \tag{7.8}$$

Remarkably, our effective medium approach supports the requirement that these

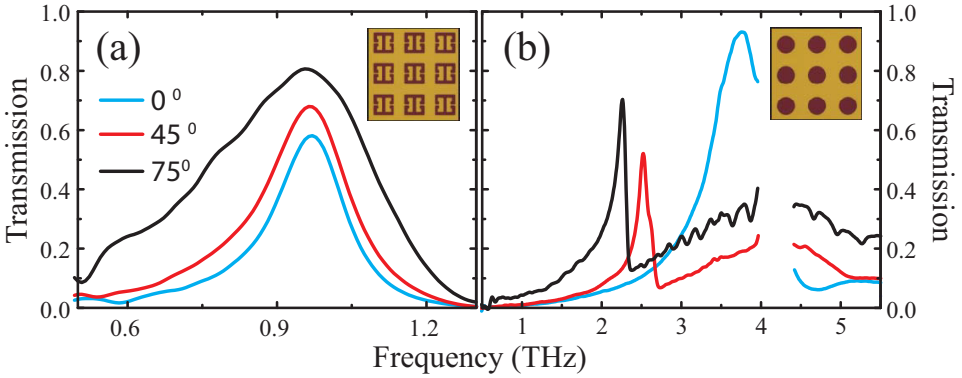

Figure 7.4: Measured transmittance at 0^o, 45^o, and 75 ^{o} for (a) the metamaterial and (b) the circle apertures. The insets are the fabricated metamaterial and circle aperture samples.

Babinet films would have degenerate effective bulk and surface plasmons in the long wavelength limit. This feature is not available to the majority of FSSs.

We proceed to measure the angular behavior of these perforated films to examine the interplay between surface and bulk plasmonic waves [115]. Two presumptions for these aperture media have to be satisfied as our approach essentially rests on Babinet's principle - they must be thin and highly conductive [34, 140]. Because at terahertz metals are essentially perfect conductors, it leaves one challenge to overcome. A 500nm-thick Si_3N_4 free-standing membrane, ($\sim \lambda_0/1000$), was then used to support the patterned structure to reduce the substrate effect. Additionally, periodic circle apertures with the same a are fabricated for reference. The frequency dependent transmittance for transverse magnetic polarized light was characterized at a sequence of incident angles from 0 up to 75 degrees using a commercially available Fourier transform infrared spectrometer (FTIR). Three representative transmission spectra measured at 0, 45 and 75 degrees for the CMM and circle geometries are shown in Fig. 7.4 (a) and (c), respectively. We first discuss the spectral responses of the CMMs.

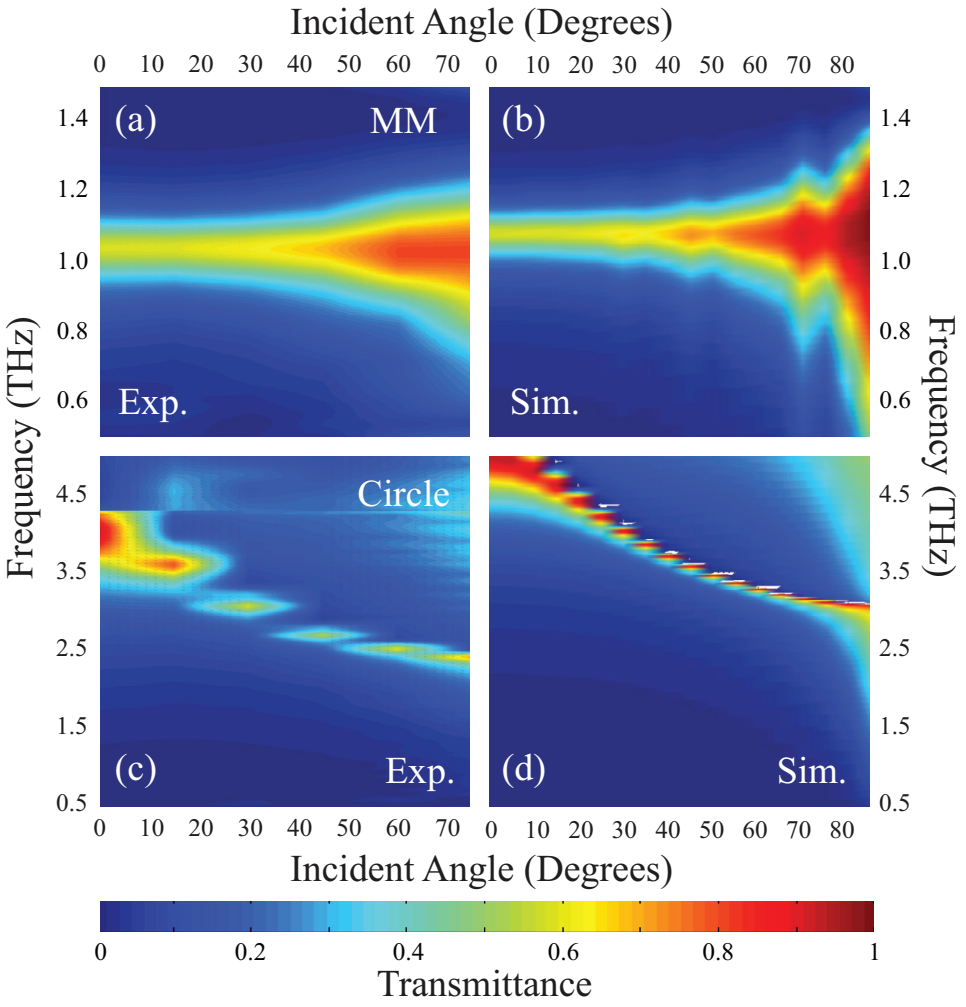

Figure 7.5: Measured transmittance as a function of frequency and angle for (a) the metamaterial and (c) the circle apertures. (b) and (d) are simulated results for the metamaterial and the circle structures, respectively.

Since we are interested in the fundamental resonance, the data is only presented from 0.5 to 1.3 THz. For normal incidence, a transmission maximum at 0.97 THz is observed with a value of 60%. At 45 degrees, $T(\omega)$ peaks at the same position as the previous case, but both the amplitude and the transmission bandwidth increase noticeably. At the widest angle of 75 degrees, the peak position shifts slightly to 0.955 THz, while the amplitude and the bandwidth continue to grow. In contrast, the transmission spectra of the circle apertures reveal a strong angular dependence. At the normal angle, $T(\omega)$ peaks at 3.8 THz with a transmittance of 95%. At 45 and 75 degrees, the primary resonance redshifts to 2.5 and 2.2 THz, respectively, but the amplitude varies non-monotonically. The tendency of the angular spectral behaviors is more evident as we plot the transmittance as a function of both frequency and incident angle for both configurations, as shown Fig. 7.5 (a) and (c). Figure 7.5 (b) and (d) display a computational investigation for validating these experimental observations. We see good agreement between both cases besides a few inconsistencies. The errors are attributed to the fabrication tolerance and uncertainty in modeling the dielectric properties of Si_3N_4 film that leads to the mismatch in the peak position and the amplitude.

Our investigation confirms that the transmittance of the metamaterial apertures are angle-insensitive evidencing that the metamaterial aperture media have identical ω_b and ω_{sp}. Their peak position redshifts about 1% in comparison with 30% for the circle apertures between two extreme angle incidence - 0^o and 75^o. It is worth mentioning that the bulk and surface plasmon polaritons not necessitate to have the same propagation loss leading that the bandwidth and the amplitude become susceptible to the change of the incident angle. Considering these optically thin aperture media are

two-dimensional, only the SPPs are allowed to travel, and thus to dissipate energy. As the radiative loss dominates in EOT responses, the more light coupled onto the SPP mode, the higher the transmission and the wider the bandwidth are. Our interpretation qualitatively describes all experimental observations, although it requires further investigation regarding the loss mechanism of these designs. Nonetheless, we present the first angle-insensitive THz filtering device made by single layer metamaterials. As optical functional elements are largely lacking in this range, our results pave a new way for designing compact bandpass filters that possess an angular insensitivity. Of course, as the spectral responses of metamaterials are scalable, our configuration can be easily extended to other regimes of the electromagnetic spectrum.

To conclude, we propose resonant charge carriers of complementary metamaterial structures are meta-holes. Their dielectric properties can be described by a combination of Drude and Lorentzian models without applying electromagnetic duality that often leads to nonphysical interpretation. Further, our model affirms that these subwavelength structured holes have identical effective bulk and surface plasmon frequencies and feature an angular insensitive transmission. The results are consistent with our experimental and computational investigation.

Bibliography

[1] A.F. Harvey. Periodic and Guiding Structures at Microwave Frequencies. *IEEE Transactions on Microwave Theory and Techniques*, 8(1):30–61, January 1960.

[2] Heinz Raether. *Surface plasmons on smooth and rough surfaces and on gratings, Volume 111*. Springer, 1988.

[3] J. B. Pendry. Negative Refraction Makes a Perfect Lens. *Physical Review Letters*, 85(18):3966–3969, October 2000.

[4] David R Smith. Applied physics. How to build a superlens. *Science (New York, N.Y.)*, 308(5721):502–3, April 2005.

[5] Nicholas Fang, Hyesog Lee, Cheng Sun, and Xiang Zhang. Sub-diffraction-limited optical imaging with a silver superlens. *Science (New York, N.Y.)*, 308(5721):534–7, April 2005.

[6] D Schurig, J J Mock, B J Justice, S A Cummer, J B Pendry, A F Starr, and D R Smith. Metamaterial electromagnetic cloak at microwave frequencies. *Science (New York, N.Y.)*, 314(5801):977–80, November 2006.

[7] Matteo Burresi, Daniela Diessel, Dries van Oosten, Stefan Linden, Martin Wegener, and L Kuipers. Negative-index metamaterials: looking into the unit cell. *Nano letters*, 10(7):2480–3, July 2010.

[8] J B Pendry, D Schurig, and D R Smith. Controlling electromagnetic fields. *Science (New York, N.Y.)*, 312(5781):1780–2, June 2006.

[9] Nathan I. Landy and Willie J. Padilla. Guiding light with conformal transformations. *Optics Express*, 17(17):14872, August 2009.

[10] J.B. Pendry, A.J. Holden, D.J. Robbins, and W.J. Stewart. Magnetism from conductors and enhanced nonlinear phenomena. *IEEE Transactions on Microwave Theory and Techniques*, 47(11):2075–2084, 1999.

[11] Wenshan Cai and Vladimir M. Shalaev. *Optical Metamaterials: Fundamentals and Applications(Google eBook)*, volume 0. Springer, 2009.

[12] Saïd Zouhdi, Ari Sihvola, and Mohamed Arsalane, editors. *Advances in Electromagnetics of Complex Media and Metamaterials*, volume 89. Springer Netherlands, Dordrecht, 2002.

[13] A. Serdyukov, I. Semchenki, S. Tretyakov, and A. Sihvola. *Electromagnetics of Bi-anisotropic Materials: Theory and Applications*, volume 1. Gordon and Breach Science, 2001.

[14] T J Yen, W J Padilla, N Fang, D C Vier, D R Smith, J B Pendry, D N Basov, and X Zhang. Terahertz magnetic response from artificial materials. *Science (New York, N.Y.)*, 303(5663):1494–6, March 2004.

[15] Christophe Caloz and Tatsuo Itoh. *Electromagnetic Metamaterials: Transmission Line Theory and Microwave Applications*. Wiley, 2006.

[16] Stefan Linden, Christian Enkrich, Martin Wegener, Jiangfeng Zhou, Thomas Koschny, and Costas M Soukoulis. Magnetic response of metamaterials at 100 terahertz. *Science (New York, N.Y.)*, 306(5700):1351–3, November 2004.

[17] D. Schurig, J. J. Mock, and D. R. Smith. Electric-field-coupled resonators for negative permittivity metamaterials. *Applied Physics Letters*, 88(4):041109, January 2006.

[18] W. Padilla, M. Aronsson, C. Highstrete, Mark Lee, A. Taylor, and R. Averitt. Electrically resonant terahertz metamaterials: Theoretical and experimental investigations. *Physical Review B*, 75(4):041102, January 2007.

[19] Alastair P Hibbins, Benjamin R Evans, and J Roy Sambles. Experimental verification of designer surface plasmons. *Science (New York, N.Y.)*, 308(5722):670–672, April 2005.

[20] Allen Taflove. *Computational Electrodynamics: The Finite - Difference Time - Domain Method*, volume 1. Artech House, Incorporated, 1995.

[21] Jian-Ming Jin. *The Finite Element Method in Electromagnetics*. Wiley, 2002.

[22] D. R. Smith, S. Schultz, P. Markos, and C.M. Soukoulis. Determination of effective permittivity and permeability of metamaterials from reflection and transmission coefficients. *Physical Review B*, 65(19):195104, April 2002.

[23] D. R. Smith, D. C. Vier, Th. Koschny, and C. M. Soukoulis. Electromagnetic parameter retrieval from inhomogeneous metamaterials. *Physical Review E*, 71(3):036617, March 2005.

[24] M. van Exter and D.R. Grischkowsky. Characterization of an optoelectronic terahertz beam system. *IEEE Transactions on Microwave Theory and Techniques*, 38(11):1684–1691, 1990.

[25] Susan L. Dexheimer, editor. *Terahertz Spectroscopy: Principles And Applications*. Taylor & Francis, 2008.

[26] John F. OHara, J. M. O. Zide, A. C. Gossard, A. J. Taylor, and R. D. Averitt. Enhanced terahertz detection via ErAs:GaAs nanoisland superlattices. *Applied Physics Letters*, 88(25):251119, June 2006.

[27] Albert Abraham Michelson. *On the Application of Interference Methods to Spectroscopic Measurements*. Smithsonian Inst., 1903.

[28] Peter Griffiths and James A. De Haseth. *Fourier Transform Infrared Spectrometry(Google eBook)*. John Wiley & Sons, 2007.

[29] Viktor G Veselago. THE ELECTRODYNAMICS OF SUBSTANCES WITH SIMULTANEOUSLY NEGATIVE VALUES OF AND μ. *Soviet Physics Uspekhi*, 10(4):509–514, April 1968.

[30] D. Smith, Willie Padilla, D. Vier, S. Nemat-Nasser, and S. Schultz. Composite Medium with Simultaneously Negative Permeability and Permittivity. *Physical Review Letters*, 84(18):4184–4187, May 2000.

[31] R A Shelby, D R Smith, and S Schultz. Experimental verification of a negative index of refraction. *Science (New York, N.Y.)*, 292(5514):77–9, April 2001.

[32] D R Smith, J B Pendry, and M C K Wiltshire. Metamaterials and negative refractive index. *Science (New York, N.Y.)*, 305(5685):788–92, August 2004.

[33] E. Cubukcu, K. Aydin, E. Ozbay, S. Foteinopoulou, and C. Soukoulis. Subwavelength Resolution in a Two-Dimensional Photonic-Crystal-Based Superlens. *Physical Review Letters*, 91(20):207401, November 2003.

[34] John David Jackson. *Classical Electrodynamics*. John Wiley, New York, 3rd edition, 1999.

[35] Tuck C. Choy. *Effective Medium Theory: Principles and Applications*. Oxford University Press, 1999.

[36] David R. Smith and John B. Pendry. Homogenization of metamaterials by field averaging (invited paper). *Journal of the Optical Society of America B*, 23(3):391, March 2006.

[37] Constantin R. Simovski and Sergei A. Tretyakov. Local constitutive parameters of metamaterials from an effective-medium perspective. *Physical Review B*, 75(19):195111, May 2007.

[38] C. R. Simovski. Material parameters of metamaterials (a Review). *Optics and Spectroscopy*, 107(5):726–753, December 2009.

[39] D. R. Smith. Analytic expressions for the constitutive parameters of magnetoelectric metamaterials. *Physical Review E*, 81(3):036605, March 2010.

[40] Yosuke Minowa, Masaya Nagai, Hu Tao, Kebin Fan, A. C. Strikwerda, Xin Zhang, Richard D. Averitt, and Koichiro Tanaka. Extremely Thin Metamaterial as Slab Waveguide at Terahertz Frequencies. *IEEE Transactions on Terahertz Science and Technology*, 1(2):441–449, November 2011.

[41] H. Mosallaei and K. Sarabandi. A one-layer ultra-thin meta-surface absorber. In *2005 IEEE Antennas and Propagation Society International Symposium*, volume 1B, pages 615–618. IEEE, 2005.

[42] J. OHara, A. K. Azad, and A. J. Taylor. A method to determine effective metamaterial properties based on stratified metafilms. *The European Physical Journal D*, 58(2):243–247, May 2010.

[43] A. Alexopoulos. Effective-medium theory of surfaces and metasurfaces containing two-dimensional binary inclusions. *Physical Review E*, 81(4):046607, April 2010.

[44] T. Koschny, P. Markoš, D. Smith, and C. Soukoulis. Resonant and antiresonant frequency dependence of the effective parameters of metamaterials. *Physical Review E*, 68(6):065602, December 2003.

[45] Constantin R. Simovski. Bloch material parameters of magneto-dielectric metamaterials and the concept of Bloch lattices. *Metamaterials*, 1(2):62–80, December 2007.

[46] N. Landy, S. Sajuyigbe, J. Mock, D. Smith, and W. Padilla. Perfect Metamaterial Absorber. *Physical Review Letters*, 100(20):207402, May 2008.

[47] Hu Tao, Nathan I. Landy, Christopher M. Bingham, Xin Zhang, Richard D. Averitt, and Willie J. Padilla. A metamaterial absorber for the terahertz regime: design, fabrication and characterization. *Optics Express*, 16(10):7181, May 2008.

[48] Hou-Tong Chen, John F. O'Hara, Antoinette J. Taylor, Richard D. Averitt, Clark Highstrete, Mark Lee, and Willie J. Padilla. Complementary planar terahertz metamaterials. *Optics Express*, 15(3):1084, February 2007.

[49] John F. O'Hara, Evgenya Smirnova, Hou-Tong Chen, Antoinette J. Taylor, Richard D. Averitt, Clark Highstrete, Mark Lee, and Andwillie J. Padilla. Properties of Planar Electric Metamaterials for Novel TeraHertz Applications. *Journal of Nanoelectronics and Optoelectronics*, 2(1):90–95, April 2007.

[50] Hu Tao, A C Strikwerda, K Fan, C M Bingham, W J Padilla, Xin Zhang, and R D Averitt. Terahertz metamaterials on free-standing highly-flexible polyimide substrates. *Journal of Physics D: Applied Physics*, 41(23):232004, December 2008.

[51] Ioachim Pupeza, Rafal Wilk, and Martin Koch. Highly accurate optical material parameter determination with THz time-domain spectroscopy. *Optics Express*, 15(7):4335, April 2007.

[52] Maik Scheller, Christian Jansen, and Martin Koch. Analyzing sub-100-μm samples with transmission terahertz time domain spectroscopy. *Optics Communications*, 282(7):1304–1306, April 2009.

[53] Willie J. Padilla. Group theoretical description of artificial electromagnetic metamaterials. *Optics Express*, 15(4):1639, February 2007.

[54] Muhan Choi, Seung Hoon Lee, Yushin Kim, Seung Beom Kang, Jonghwa Shin, Min Hwan Kwak, Kwang-Young Kang, Yong-Hee Lee, Namkyoo Park, and Bumki Min. A terahertz metamaterial with unnaturally high refractive index. *Nature*, 470(7334):369–73, February 2011.

[55] E. Tatartschuk, A. Radkovskaya, E. Shamonina, and L. Solymar. Generalized Brillouin diagrams for evanescent waves in metamaterials with interelement coupling. *Physical Review B*, 81(11):115110, March 2010.

[56] Mikhail Lapine, David Powell, Maxim Gorkunov, Ilya Shadrivov, Ricardo Marques, and Yuri Kivshar. Structural tunability in metamaterials. *Applied Physics Letters*, 95(8):084105, August 2009.

[57] David A. Powell, Mikhail Lapine, Maxim V. Gorkunov, Ilya V. Shadrivov, and Yuri S. Kivshar. Metamaterial tuning by manipulation of near-field interaction. *Physical Review B*, 82(15):155128, October 2010.

[58] H. Liu, Y. M. Liu, T. Li, S. M. Wang, S. N. Zhu, and X. Zhang. Coupled magnetic plasmons in metamaterials. *physica status solidi (b)*, 246(7):1397–1406, July 2009.

[59] Jiangfeng Zhou, Thomas Koschny, Maria Kafesaki, and Costas Soukoulis. Negative refractive index response of weakly and strongly coupled optical metamaterials. *Physical Review B*, 80(3):035109, July 2009.

[60] Na Liu and Harald Giessen. Coupling effects in optical metamaterials. *Angewandte Chemie (International ed. in English)*, 49(51):9838–52, December 2010.

[61] John F. O'Hara, Richard D. Averitt, and Antoinette J. Taylor. Prism coupling to terahertz surface plasmon polaritons. *Optics Express*, 13(16):6117, August 2005.

[62] Georg Goubau. Surface Waves and Their Application to Transmission Lines. *Journal of Applied Physics*, 21(11):1119, November 1950.

[63] Georg Goubau. On the Excitation of Surface Waves. *Proceedings of the IRE*, 40(7):865–868, July 1952.

[64] G. Goubau. Open Wire Lines. *IEEE Transactions on Microwave Theory and Techniques*, 4(4):197–200, October 1956.

[65] Georg Goubau. Surface-wave Transmission Line. *Acta Tech. Acad. Sci. Hung.*, 17:269, 1957.

[66] V N Datsko and A A Kopylov. On surface electromagnetic waves. *Physics-Uspekhi*, 51(1):101–102, January 2008.

[67] Aleksandr V Kukushkin. On the existence and physical meaning of the Zenneck wave. *Physics-Uspekhi*, 52(7):755–756, July 2009.

[68] R. S. Elliott. On the Theory of Corrugated Plan Surfaces. *IRE Trans. Antennas Propag.*, 2:71, 1954.

[69] J B Pendry, L Martín-Moreno, and F J Garcia-Vidal. Mimicking surface plasmons with structured surfaces. *Science*, 305(5685):847–848, August 2004.

[70] Simon Ramo, John R. Whinnery, and Theodore Van Duzer. *Fields and Waves in Communication Electronics*. Wiley, 3rd edition, 1994.

[71] R. P. Feynman. There's Plenty of Room at the Bottom. *Eng. Sci.*, 23:22–36, 1960.

[72] Yu Yuan, Christopher Bingham, Talmage Tyler, Sabarni Palit, Thomas H. Hand, Willie J. Padilla, David R. Smith, Nan Marie Jokerst, and Steven A. Cummer. Dual-band planar electric metamaterial in the terahertz regime. *Optics Express*, 16(13):9746, June 2008.

[73] Christopher M. Bingham, Hu Tao, Xianliang Liu, Richard D. Averitt, Xin Zhang, and Willie J. Padilla. Planar wallpaper group metamaterials for novel terahertz applications. *Optics Express*, 16(23):18565, October 2008.

[74] F. Martin, F. Falcone, J. Bonache, R. Marques, and M. Sorolla. Miniaturized coplanar waveguide stop band filters based on multiple tuned split ring resonators. *IEEE Microwave and Wireless Components Letters*, 13(12):511–513, December 2003.

[75] F. Falcone, T. Lopetegi, M. Laso, J. Baena, J. Bonache, M. Beruete, R. Marqués, F. Martín, and M. Sorolla. Babinet Principle Applied to the Design of Metasurfaces and Metamaterials. *Physical Review Letters*, 93(19):197401, November 2004.

[76] Ibraheem A. Ibraheem and Martin Koch. Coplanar waveguide metamaterials: The role of bandwidth modifying slots. *Applied Physics Letters*, 91(11):113517, September 2007.

[77] I A I Al-Naib, C Jansen, and M Koch. Miniaturized bandpass filter based on metamaterial resonators: a conceptual study. *Journal of Physics D: Applied Physics*, 41(20):205002, October 2008.

[78] Mahmoud A. Abdalla and Zhirun Hu. Nonreciprocal left handed coplanar waveguide over ferrite substrate with only shunt inductive load. *Microwave and Optical Technology Letters*, 49(11):2810–2814, November 2007.

[79] Ibraheem A. I. Al-Naib, Christian Jansen, and Martin Koch. SINGLE METAL LAYER CPW METAMATERIAL BANDPASS FILTER. *Progress In Electromagnetics Research Letters*, 17:153–161, 2010.

[80] I. Gil, J. Bonache, J. Garcia-Garcia, and F. Martin. Tunable metamaterial transmission lines based on varactor-loaded split-ring resonators. *IEEE Transactions on Microwave Theory and Techniques*, 54(6):2665–2674, June 2006.

[81] Adolfo Vélez, Jordi Bonache, and Ferran Martín. Effects of varying the series capacitance in CSRR-loaded metamaterial transmission lines. *Microwave and Optical Technology Letters*, 49(9):2245–2248, September 2007.

[82] Evren Ekmekci, Kagan Topalli, Tayfun Akin, and Gonul Turhan-Sayan. A tunable multi-band metamaterial design using micro-split SRR structures. *Optics express*, 17(18):16046–58, August 2009.

[83] J. Brown. The Types of Wave Which May Exist Near a Guiding Surface. *Proceedings of the IEEE*, 100:363, 1953.

[84] A. Treizebre, T. Akalin, and B. Bocquet. Planar excitation of Goubau Transmission Lines for THz BioMEMS. *IEEE Microwave and Wireless Components Letters*, 15(12):886–888, December 2005.

[85] T. Akalin, A. Treizebre, and B. Bocquet. Single-wire transmission lines at terahertz frequencies. *IEEE Transactions on Microwave Theory and Techniques*, 54(6):2762–2767, June 2006.

[86] E. Economou, Th. Koschny, and C. Soukoulis. Strong diamagnetic response in split-ring-resonator metamaterials: Numerical study and two-loop model. *Physical Review B*, 77(9):092401, March 2008.

[87] Xianliang Liu, Talmage Tyler, Tatiana Starr, Anthony F. Starr, Nan Marie Jokerst, and Willie J. Padilla. Taming the Blackbody with Infrared Metamaterials as Selective Thermal Emitters. *Physical Review Letters*, 107(4):045901, July 2011.

[88] C. Enkrich, M. Wegener, S. Linden, S. Burger, L. Zschiedrich, F. Schmidt, J. Zhou, Th. Koschny, and C. Soukoulis. Magnetic Metamaterials at Telecommunication and Visible Frequencies. *Physical Review Letters*, 95(20):203901, November 2005.

[89] E. Shamonina, V. A. Kalinin, K. H. Ringhofer, and L. Solymar. Magnetoinductive waves in one, two, and three dimensions. *Journal of Applied Physics*, 92(10):6252, November 2002.

[90] M. C. K. Wiltshire. Radio frequency (RF) metamaterials. *physica status solidi (b)*, 244(4):1227–1236, April 2007.

[91] S. Tricarico, F. Bilotti, and L. Vegni. Multi-functional dipole antennas based on artificial magnetic metamaterials. *IET Microwaves, Antennas & Propagation*, 4(8):1026, 2010.

[92] Ferran Paredes, Gerard Zamora Gonzalez, Jordi Bonache, and Ferran Martin. Dual-Band Impedance-Matching Networks Based on Split-Ring Resonators for Applications in RF Identification (RFID). *IEEE Transactions on Microwave Theory and Techniques*, 58(5):1159–1166, May 2010.

[93] Michael Wiltshire, J. Hajnal, J. Pendry, D. Edwards, and C. Stevens. Metamaterial endoscope for magnetic field transfer: near field imaging with magnetic wires. *Optics Express*, 11(7):709, April 2003.

[94] M. J. Freire and R. Marques. Planar magnetoinductive lens for three-dimensional subwavelength imaging. *Applied Physics Letters*, 86(18):182505, April 2005.

[95] Yaroslav Urzhumov and David R. Smith. Metamaterial-enhanced coupling between magnetic dipoles for efficient wireless power transfer. *Physical Review B*, 83(20):205114, May 2011.

[96] Bingnan Wang, Koon Hoo Teo, Tamotsu Nishino, William Yerazunis, John Barnwell, and Jinyun Zhang. Experiments on wireless power transfer with metamaterials. *Applied Physics Letters*, 98(25):254101, June 2011.

[97] Juan Baena, Ricardo Marqués, Francisco Medina, and Jesús Martel. Artificial magnetic metamaterial design by using spiral resonators. *Physical Review B*, 69(1):014402, January 2004.

[98] Filiberto Bilotti, Alessandro Toscano, and Lucio Vegni. Design of Spiral and Multiple Split-Ring Resonators for the Realization of Miniaturized Metamaterial Samples. *IEEE Transactions on Antennas and Propagation*, 55(8):2258–2267, August 2007.

[99] Cihan Kurter, John Abrahams, and Steven M. Anlage. Miniaturized superconducting metamaterials for radio frequencies. *Applied Physics Letters*, 96(25):253504, June 2010.

[100] R. Marques, F. Mesa, J. Martel, and F. Medina. Comparative analysis of edge- and broadside-coupled split ring resonators for metamaterial design - Theory and experiments. *IEEE Transactions on Antennas and Propagation*, 51(10):2572–2581, October 2003.

[101] Ricardo Marqués, Francisco Medina, and Rachid Rafii-El-Idrissi. Role of bianisotropy in negative permeability and left-handed metamaterials. *Physical Review B*, 65(14):144440, April 2002.

[102] Claire M Watts, Xianliang Liu, and Willie J Padilla. Metamaterial electromagnetic wave absorbers. *Advanced materials (Deerfield Beach, Fla.)*, 24(23):OP98–OP120, June 2012.

[103] Xianliang Liu, Tatiana Starr, Anthony F. Starr, and Willie J. Padilla. Infrared Spatial and Frequency Selective Metamaterial with Near-Unity Absorbance. *Physical Review Letters*, 104(20):207403, May 2010.

[104] Koray Aydin, Vivian E Ferry, Ryan M Briggs, and Harry A Atwater. Broadband polarization-independent resonant light absorption using ultrathin plasmonic super absorbers. *Nature communications*, 2:517, January 2011.

[105] David Shrekenhamer, Wangren Xu, Suresh Venkatesh, David Schurig, Sameer Sonkusale, and Willie Padilla. Experimental Realization of a Metamaterial Detector Focal Plane Array. *Physical Review Letters*, 109(17):177401–, October 2012.

[106] D.L Begley, R.W Alexander, C.A Ward, and R.J Bell. Propagation of surface electromagnetic waves on n-type GaAs in the far infrared. *Surface Science*, 81(1):238–244, February 1979.

[107] Fumiaki Miyamaru, Mototsugu Kamijyo, Keisuke Takano, Masanori Hangyo, Hiroshi Miyazaki, and Mitsuo Wada Takeda. Characteristics and generation process of surface waves excited on a perfect conductor surface. *Optics express*, 18(16):17576–83, August 2010.

[108] Liang-Yin Chen, Wan-Shao Tsai, Wen-Hao Hsu, Kuan-Yu Chen, and Way-Seen Wang. Fabrication and Characterization of Benzocyclobutene Optical Waveguides by UV Pulsed-Laser Illumination. *IEEE Journal of Quantum Electronics*, 43(4):303–310, March 2007.

[109] Leonard Hanssen. Integrating-Sphere System and Method for Absolute Measurement of Transmittance, Reflectance, and Absorptance of Specular Samples. *Applied Optics*, 40(19):3196, July 2001.

[110] K. Gindele, M. Köhl, and M. Mast. Spectral reflectance measurements using an integrating sphere in the infrared. *Applied Optics*, 24(12):1757, June 1985.

[111] Vladimir Kaganer and Karl Sabelfeld. X-ray diffraction peaks from partially ordered misfit dislocations. *Physical Review B*, 80(18):184105, November 2009.

[112] J. A. Barnes, T. E. Gough, and M. Stoer. The infrared spectrum of clustered carbon dioxide: An interpretation via bulk optical constants. *The Journal of Chemical Physics*, 95(7):4840, 1991.

[113] M. A. Ordal, Robert J. Bell, R. W. Alexander, Jr, L. L. Long, and M. R. Querry. Optical properties of fourteen metals in the infrared and far infrared: Al, Co, Cu, Au, Fe, Pb, Mo, Ni, Pd, Pt, Ag, Ti, V, and W. *Applied Optics*, 24(24):4493, December 1985.

[114] H. Bethe. Theory of Diffraction by Small Holes. *Physical Review*, 66(7-8):163–182, October 1944.

[115] T. W. Ebbesen, H. J. Lezec, H. F. Ghaemi, T. Thio, and P. A. Wolff. Extraordinary optical transmission through sub-wavelength hole arrays. *Nature*, 391(6668):667–669, February 1998.

[116] L. Martín-Moreno, F. García-Vidal, H. Lezec, K. Pellerin, T. Thio, J. Pendry, and T. Ebbesen. Theory of Extraordinary Optical Transmission through Subwavelength Hole Arrays. *Physical Review Letters*, 86(6):1114–1117, February 2001.

[117] H J Lezec, A Degiron, E Devaux, R A Linke, L Martin-Moreno, F J Garcia-Vidal, and T W Ebbesen. Beaming light from a subwavelength aperture. *Science*, 297(5582):820–2, August 2002.

[118] K. Koerkamp, S. Enoch, F. Segerink, N. van Hulst, and L. Kuipers. Strong Influence of Hole Shape on Extraordinary Transmission through Periodic Arrays of Subwavelength Holes. *Physical Review Letters*, 92(18):183901, May 2004.

[119] T. Zentgraf, T. Meyrath, A. Seidel, S. Kaiser, H. Giessen, C. Rockstuhl, and F. Lederer. Babinets principle for optical frequency metamaterials and nanoantennas. *Physical Review B*, 76(3):033407, July 2007.

[120] Thomas Paul, Christoph Menzel, Carsten Rockstuhl, and Falk Lederer. Advanced optical metamaterials. *Advanced materials (Deerfield Beach, Fla.)*, 22(21):2354–7, June 2010.

[121] K. Kempa. Percolation effects in the checkerboard Babinet series of metamaterial structures. *physica status solidi (RRL) - Rapid Research Letters*, 4(8-9):218–220, September 2010.

[122] Y. Peng, T. Paudel, W.-C. Chen, W. J. Padilla, Z. F. Ren, and K. Kempa. Percolation and polaritonic effects in periodic planar nanostructures evolving from holes to islands. *Applied Physics Letters*, 97(4):041901, July 2010.

[123] Haitao Liu and Philippe Lalanne. Microscopic theory of the extraordinary optical transmission. *Nature*, 452(7188):728–31, April 2008.

[124] R. Marquès, F. Mesa, L. Jelinek, and F. Medina. Analytical theory of extraordinary transmission through metallic diffraction screens perforated by small holes. *Optics Express*, 17(7):5571–5579, March 2009.

[125] Chandra S. R. Kaipa, Alexander B. Yakovlev, Francisco Medina, Francisco Mesa, Celia A. M. Butler, and Alastair P. Hibbins. Circuit modeling of the transmissivity of stacked two-dimensional metallic meshes. *Optics Express*, 18(13):13309–13320, June 2010.

[126] Chandra S. R. Kaipa, Alexander B. Yakovlev, Francisco Medina, and Francisco Mesa. Transmission through stacked 2D periodic distributions of square conducting patches. *Journal of Applied Physics*, 112(3):033101, 2012.

[127] D. M. Byrne. Infrared mesh filters fabricated by electron-beam lithography. *Journal of Vacuum Science & Technology B: Microelectronics and Nanometer Structures*, 3(1):268, January 1985.

[128] Charles M. Rhoads, Edward K. Damon, and Benedikt A. Munk. Mid-infrared filters using conducting elements. *Applied Optics*, 21(15):2814, August 1982.

[129] Ben A. Munk. *Frequency Selective Surfaces: Theory and Design*. John Wiley & Sons, 2005.

[130] F J Garcia-Vidal, L Martín-Moreno, and J B Pendry. Surfaces with holes in them: new plasmonic metamaterials. *Journal of Optics A: Pure and Applied Optics*, 7(2):S97–S101, February 2005.

[131] Thomas H. Hand, Jonah Gollub, Soji Sajuyigbe, David R. Smith, and Steven A. Cummer. Characterization of complementary electric field coupled resonant surfaces. *Applied Physics Letters*, 93(21):212504, November 2008.

[132] O. S. Heavens. *Optical Properties of Thin Solid Films*. Dover Publications, 1991.

[133] F. J. Garcia-Vidal, T. W. Ebbesen, and L. Kuipers. Light passing through subwavelength apertures. *Reviews of Modern Physics*, 82(1):729–787, March 2010.

[134] Jiang-Yan Li, Yi-Lei Hua, Jin-Xin Fu, and Zhi-Yuan Li. Influence of hole geometry and lattice constant on extraordinary optical transmission through subwavelength hole arrays in metal films. *Journal of Applied Physics*, 107(7):073101, April 2010.

[135] Jill Elliott, Igor I. Smolyaninov, Nikolay I. Zheludev, and Anatoly V. Zayats. Polarization control of optical transmission of a periodic array of elliptical nanoholes in a metal film. *Optics Letters*, 29(12):1414, June 2004.

[136] R. Gordon, A. Brolo, A. McKinnon, A. Rajora, B. Leathem, and K. Kavanagh. Strong Polarization in the Optical Transmission through Elliptical Nanohole Arrays. *Physical Review Letters*, 92(3):037401, January 2004.

[137] R. Gordon, M. Hughes, B. Leathem, K. L. Kavanagh, and A. G. Brolo. Basis and Lattice Polarization Mechanisms for Light Transmission through Nanohole Arrays in a Metal Film. *Nano Letters*, 5(7):1243–1246, July 2005.

[138] Yakov Strelniker. Theory of optical transmission through elliptical nanohole arrays. *Physical Review B*, 76(8):085409, August 2007.

[139] Max Born and Emil Wolf. *Principles of Optics: Electromagnetic Theory of Propagation, Interference and Diffraction of Light*. Cambridge University Press, 1999.

[140] Constantine A. Balanis. *Antenna Theory: Analysis and Design*. Wiley, 2005.

[141] Jonah Gollub, David Smith, David Vier, Tim Perram, and Jack Mock. Experimental characterization of magnetic surface plasmons on metamaterials with negative permeability. *Physical Review B*, 71(19):195402, May 2005.

[142] W.-C. Chen, N. I. Landy, K. Kempa, and W. J. Padilla. A Subwavelength Extraordinary-Optical-Transmission Channel in Babinet Metamaterials. *Advanced Optical Materials*, 1(3):221–226, February 2013.